POLYTECHNIQUE MONTRÉAL

affiliée à l'Université de Montréal

Flow Control and MRI-Compatible Particle Injector: Application to Magnetic Resonance Navigation

NING LI

Institut de génie biomédical

Thèse présentée en vue de l'obtention du diplôme de *Philosophiæ Doctor*

Génie biomédical

Avril 2019

POLYTECHNIQUE MONTRÉAL

affiliée à l'Université de Montréal

Cette thèse intitulée :

Flow Control and MRI-Compatible Particle Injector: Application to Magnetic Resonance Navigation

présentée par **Ning LI**

en vue de l'obtention du diplôme de *Philosophiæ Doctor*

a été dûment acceptée par le jury d'examen constitué de :

Frédéric SIROIS, président

Sylvain MARTEL, membre et directeur de recherche

Gilles SOULEZ, membre et codirecteur de recherche

Julien COHEN-ADAD, membre

Antoine FERREIRA, membre externe

DEDICATION

To my beloved wife Cui, and my parents...

ACKNOWLEDGEMENT

I would like to express my special thanks and appreciations to my research supervisors, Professor Sylvain Martel and Professor Gilles Soulez. They are both tremendously honourable mentors for me. I am so grateful to Sylvain for giving me the means to do this doctorate. His energy, ideas and ambition in dealing with compelling research problems are excellent models for me to learn from. My co-director, Dr. Gilles Soulez, is someone who can not be replaced on this journey. He provided excellent guidance for this project and always gave me constructive comments concerning my work. Without their help, this project would not have seen the light of the day.

Thanks to Mr. Charles Tremblay, an energetic and joyful friend. He made the working environment interesting and efficient. He was always willing to listen and help me.

Thanks to other members of the Nanorobotics laboratory: Mahmood Mohammadi, Dumitru Loghin, Maxime Latulippe, Arash Azizi, Kévin Gagné, Yasamin Majedi, et al. Everyone is nice and patient regarding my communication problems in English.

I would also like to thank other members of our research group: Samuel Kadoury and Gerald Moran. They provided excellent guidance for this particular research topic.

Thanks to Francois Michaud. We spent a lot of time together making the setup and doing the experiments. He is also a wonderful friend and I admire his positive outlook and his dream of becoming a doctor.

Thanks to Rosalie Plantefève, she was always willing to help me and share her findings and experiences. Her rigorous academic attitudes and statistical methods gave me great inspiration.

Thanks to members in the cooperative laboratory at the University of British Columbia: Prof. Urs, Dr. Samuel and Mrs. Zeynab. We had a very pleasant cooperation experience. Thanks to their works, I was able to acquire the perfect particles used for liver embolization.

Special thanks to Yuting Jiang, a happy girl with dreams, who has helped me find spelling mistakes in each of my paper and this thesis.

I would like to thank all my friends. There are too many to list here, but I hope you know who you are!

I would like to thank my parents, father-in-law and mother-in-law for their unconditional love

and support from overseas. I love them so much, and I would not have made it this far without them.

In the end, I would like to express my special thanks to my beloved wife Cui Wang who was always my indispensable support for all these years. Words cannot express how grateful I am to her.

RÉSUMÉ

Notre groupe de recherche travaille sur une technique de navigation par résonance magnétique (NRM) qui vise à améliorer l'efficacité du ciblage des médicaments vers les zones tumorales. Cette technique a été subdivisée en cinq parties :

1. Conception des microparticules. La taille et les matériaux constituants les particules doivent répondre aux exigences médicales et physiologiques de l'embolisation humaine, ainsi qu'à la faisabilité du pilotage des microparticules en utilisant les gradients magnétiques (≤ 40 mT/m) d'un système clinique d'imagerie par résonance magnétique (IRM).

2. Contrôle du flot sanguin. Un contrôle du flot sanguin a été mis au point pour permettre une navigation suffisamment rapide afin de réduire le temps d'injection tout en étant suffisamment lente pour assurer un taux de réussite élevé pour la NRM.

3. Conception d'un injecteur pour la formation d'agrégats de microparticules de tailles contrôlables. Un injecteur IRM compatible a été conçu pour permettre l'injection d'agrégats de particules pour à la fois réduire le temps d'injection et augmenter l'efficacité de la NRM en raison du volume magnétique plus important injecté à chaque fois.

4. Logiciel NRM. Une séquence NRM est utilisée pour suivre et orienter les agrégats injectés.

5. Intégration de l'injecteur de particules, du contrôle du flot sanguin et du logiciel NRM.

Dans cette thèse, nous cherchons à trouver des solutions aux étapes 2, 3, 4 et 5.

L'auteur a constaté que la combinaison d'un micro-flot vibratoire et d'un flot constant à faible vitesse pouvait rendre la vitesse de dérive des particules basse et constante. Un système de contrôle de l'écoulement composé d'une machine vibratoire générant le flot en question et d'une pompe péristaltique a été conçu et fabriqué pour générer ces deux types d'écoulement. Ensuite, le système a été intégré au NRM pour tester les manipulations *in vitro* visées. Dans une IRM de 1.5 Tesla (T), les microparticules encapsulant des nanoparticules superparamagnétiques ont été navigués dans un canal à bifurcation unique en forme de Y. En comparant les résultats avec le NRM à débit constant, nous avons démontré que le modèle de flot vibrantoire proposé peut améliorer de manière significative le taux de réussite du NRM avec un gradient magnétique inférieur à 40 mT/m qui correspond au seuil maximum de gradient qui peut être utilisé sur une IRM clinique traditionnelle.

Par la suite, un injecteur de particules compatible avec l'IRM, composé de deux pompes péristaltiques, d'un compteur optique et d'un piège magnétique, a été proposé pour former des agrégats de particules de taille spécifique. Afin de déterminer la conception et la configuration optimales de l'injecteur, les propriétés magnétiques des microparticules, la compatibilité magnétique des différentes pièces de l'injecteur et la distribution spatiale du champ magnétique du système IRM ont été étudiées de manière exhaustive. Les particules utilisées dans l'essai avaient un diamètre de 230 ± 35 µm, ce qui respecte les spécifications requises pour une chimioembolisation trans-artérielle (TACE) chez l'adulte. Nous avons démontré que l'injecteur pouvait former des agrégats contenant 20 à 60 microparticules avec une précision de 6 particules. Les agrégats ayant des longueurs globales correspondantes de 1.6 à 3.2 mm, ce qui se situe juste dans l'échelle des diamètres internes des artères hépatiques propres et des branches de division droite et gauche. Par la suite, des agrégats constitués de 25 particules ont été injectés dans un fantôme imitant des conditions physiologiques et rhéologiques humaine. Dans ce cas, 82% des agrégats (n = 50) ont réussi à atteindre les sous-branches ciblées.

Enfin, nous avons démontré qu'il était possible d'intégrer le flot vibrant combiné avec flot constant, l'injecteur et la séquence NRM à notre injecteur afin d'établir une synchronisation entre la formation, la propulsion, la navigation et le suivi de bolus de particules dans un fantôme avec deux niveaux de bifurcation. Un modèle théorique de la taille et l'orientation des vaisseaux a été étudié et pris en compte lors du calcul de la longueur appropriée de l'agrégat de particules pour différentes tailles de vaisseaux. Une séquence d'IRM rapide (True FISP) et un gradient magnétique de 20 mT/m ont été choisis pour suivre et orienter les agrégats. Les particules magnétiques de 200 µm de diamètre moyen ont été utilisées pour évaluer l'efficacité de la NRM avec la méthode proposée. Dans les expériences, sur la base du modèle théorique, la longueur totale des agrégats a été fixée à environ 1.6 mm. Lorsqu'un agrégat était prêt, il était injecté dans le fantôme situé au centre du tunnel de l'IRM, imitant des situations réelles. Pendant ce temps, un signal de déclenchement généré automatiquement par le générateur déclenche la séquence NRM. Les agrégats de particules ont été entraînés par le flot combiné et dirigés puis suivis par la séquence NRM. En fonction de la position des agrégats dans le fantôme, la direction du gradient de navigation a été ajustée pour diriger les agrégats de microparticules dans la branche ciblée. Lorsque le tube principal du fantôme était parallèle à B_0, la distribution de base des agrégats sans NRM de gauche à gauche (GG), de gauche à droite (GD), de droite à gauche (DG) et de droite à droite (DD)

était de 4%, 96%, 0% et 0% respectivement. La précision a atteint 84% (GG), 100% (GD), 84% (DG) et 96% (DD) ($P < 0.001$, $P = 1.0$, $P < 0.001$, 1, $P < 0.001$) en utilisant la séquence de NRM correspondantes pour diriger chaque agrégat dans une branche ciblée. Ensuite, le fantôme a subi une rotation de 90 degrés horizontalement. Dans cette configuration, la branche D-G qui avait le plus faible ratio de distribution de base de 0%, passait à 80% ($P < 0.001$) après NRM. De plus, le taux de réussite du MRN était toujours supérieur à 92% à la première bifurcation dans les expériences mentionnées ci-dessus.

En conclusion, ce projet a proposé un nouveau modèle d'écoulement pour augmenter le taux de réussite de la NRM avec un gradient magnétique de 40 mT/m. Il s'agit d'une étape importante pour les expériences *in vivo* utilisant le système d'IRM clinique. Ensuite, un injecteur compatible avec l'IRM, capable de contrôler la taille des agrégats de particules, a été conçu et testé. Enfin, la première intégration du système d'injection de particules, qui alterne un gradient de guidage et une séquence True FISP dans un logiciel NRM dédié, confirme que le NRM peut être utilisée pour naviguer *in vitro* des agrégats de particules à travers deux niveaux de bifurcations à l'aide d'une IRM clinique 3 T sans modification matérielle.

ABSTRACT

The author's research group has been working on a technique of magnetic resonance navigation (MRN) which aims to improve the targeting efficiency of drugs towards tumour areas. This technique was subdivided mainly into the following steps:

1. Particle design. Sizes and materials of particles need to meet the medical and physiological requirements of human embolization, as well as the feasibility of steering the particles by using magnetic gradients (≤ 40 mT/m) of a clinical magnetic resonance imaging (MRI) system.

2. Flow control. The particles drifted by blood flow must be fast enough to decrease the particle injection time while being appropriately slow to ensure a high success rate for MRN.

3. The conception of a dedicated MR compatible injector to create microparticle aggregates with controllable sizes. The formation of aggregates can both decrease the injection time and increase the MRN efficiency because of the larger magnetic volume injected each time.

4. MRN software. An MRN sequence is used to track and steer the injected aggregates.

5. Integration of the particle injector, flow control and the MRN software.

In this thesis, I aim to find solutions for steps 2, 3, 4 and 5.

The author found that the combination of micro-vibrating flow and low-velocity constant flow could make the velocity of the drifted particles low and steady. A flow control system consisting of a vibrator and a peristaltic pump was designed and fabricated to generate these two flow patterns. Then, the system was integrated with MRN to test for the targeted *in vitro* manipulations. In a 1.5 Tesla (T) MRI system, microparticles encapsulating superparamagnetic nanoparticles were navigated in a Y-shaped single bifurcation channel. By comparing the results with MRN with constant flow, I demonstrated that the proposed flow pattern can significantly improve the success rate of MRN under a magnetic gradient of 40 mT/m, a force that can be obtained but is difficult to increase further when using a traditional clinical MRI system.

Subsequently, an MRI-compatible particle injector, composed of two peristaltic pumps, an optical counter and a magnetic trap was proposed to form specific-sized particle aggregates. In order to determine the optimal design and setup of the injector, the magnetic property of microparticles, the magnetic compatibility of different parts within the injector and the field

distribution of the MRI system were studied comprehensively. The particles used in the test had diameters of 230 ± 35 μm which respect the specifications needed for trans-arterial chemoembolization (TACE) in human adults. I demonstrated that the system could form aggregates containing 20 to 60 microparticles with a precision of 6 particles. The corresponding aggregate lengths ranged from 1.6 to 3.2 mm, which is just within the scale of internal diameters of the common, right and left hepatic arteries. Subsequently, aggregates consisting of 25 particles were injected into a phantom which mimics realistic physiological and rheological conditions. Under such circumstances, 82% of the aggregates (n = 50) were able to successfully reach subbranches.

At last, I demonstrated the feasibility of integrating the combined flow pattern, the injector and the MRN sequence to establish synchronization between the formation, propulsion, steering and tracking of particle boluses in a two-level bifurcation phantom. To start with the establishment of a theoretical model, the size and orientation of the vessels were comprehensively studied and took into consideration when the calculation for the appropriate length of the particle aggregate for different vessel sizes. Next, a steady-state coherent sequence (True FISP) and a 20 mT/m magnetic gradient were chosen as the MRN sequence and force used to track and steer moving aggregates. Finally, magnetic particles of 200 μm mean diameter were used to evaluate the MRN efficiency of the proposed method. In the experiments, based on the theoretical model, the aggregate length was set, through the injector, to roughly 1.2 mm. When an aggregate was ready, it was injected into the phantom located in the MRI bore, imitating real-life situations. Meanwhile, a trigger signal automatically generated by the trigger generator would start the MRN sequence. Particle aggregates were drifted by the combined flow and were steered and tracked by the MRN sequence. According to the position of the aggregates in the phantom, the direction of the steering gradient would be tuned to ensure that the particles were steered into the targeted branch. When the main tube of the phantom was parallel to B_0, the left–left (L-L), left–right (L-R), right–left (R-L) and right–right (R-R) baseline distribution of aggregates with no MRN were 4%, 96%, 0% and 0% respectively. The accuracy reached 84% (L-L), 100%(L-R), 84% (R-L) and 96% (R-R) ($P < 0.001$, $P = 1.0$, $P < 0.001$, $P < 0.001$) after applying corresponding MRN operations to steer each aggregate into a targeted branch. Then, the phantom was rotated 90 degrees horizontally. In that setup, the R-L branch had the smallest baseline distribution ratio of 0%, which increased to 80% ($P < 0.001$)

through MRN. Moreover, the success rate of MRN was always more than 92% at the 1st bifurcation in the experiments above.

In conclusion, this project proposes a new flow pattern for increasing the MRN success rate under the magnetic gradient of 40 mT/m. This is an important step for *in vivo* experiments using the clinical MRI system. Then, an MRI-compatible injector, capable of controlling the size of particle aggregates, was designed and tested. At last, the first integration of the particle injection system which interleaves a steering gradient and a True FISP sequence in a dedicated MRN software confirmed that MRN can be used to navigate particle aggregates *in vitro* across two branch divisions in a 3 T clinical MRI system without hardware modification.

TABLE OF CONTENTS

LIST OF TABLES

LIST OF FIGURES

LIST OF ABBREVIATIONS AND SYMBOLS

CT	Computed tomography
DEB	Drug-eluting bead
DFN	Dipole field navigation
EPI	Echo planar imaging
FFE	Fast Field Echo
FIESTA	Fast Imaging Employing Steady-state Acquisition
GRE	Gradient echo
HCC	Hepatocellular carcinoma
L-L	Left-Left
L-R	Left-Right
MRI	Magnetic resonance imaging
MRN	Magnetic resonance navigation
Poly (lactic-coglycolic acid)	PLGA
Poly (vinyl alcohol)	PVA
RF	Radio-frequency
R-L	Right-Left
R-R	Right-Right
SP	Spin echo
3D	Three dimensional
2D	Two dimensional
TACE	Transcatheter arterial chemoembolization
TE	Echo time
TMMC	Therapeutic magnetic micro carrier

TR	Repetition time
US	Ultrasound

LIST OF SYMBOLS

cm	Centimeter
emu	Electromagnetic unit
G	Gauss
g	Gram
h	Hour
k	Kilo
L	Liter
m	Meter
M	Magnetization (magnetic moment per unit volume)
min	Minute
mm	Millimeter
s	Second
T	Tesla
T1	Longitudinal relaxation time
T2	Transverse relaxation time
μm	Micrometer

LIST OF APPENDICES

CHAPTER 1 INTRODUCTION

1.1 Problem statement

In the last few years, hepatocellular carcinoma (HCC) led to continuously growing mortality rates and has become the third cause of cancer-related death worldwide [1]. Many therapeutic methods, such as surgical resection, liver transplantation, radiotherapy, percutaneous ablation, and transcatheter arterial chemoembolization (TACE), have been proposed and clinically applied to treat HCC [2, 3]. Among them, surgical resection and liver transplantation are two commonly performed surgery methods. However, in most cases, less than 30-40% of individuals are eligible to these two procedures because the cancer is often found in its late stages, thus patients do not have a sufficient hepatic functional reserve for surgical resection or enough time to wait for liver transplants. Radiotherapy is not often used as an HCC treatment option because the liver has a low tolerant for radiation. Although percutaneous ablation can be used as a non-surgical treatment, this technique is only applicable when the tumors are far away from other organs and vessels because of the heat generation and the heat sink effect in therapy [4, 5]. TACE, a minimally invasive cancer therapy method, includes selective catheterization and the intra-arterial infusion of embolization agents. The embolizing agents can block the blood flow to the arteries feeding the tumors while slowly releasing anti-tumor drugs. However, the extremity of catheters is often difficult to guide into a position close to the tumor, while being highly dependent on the physician's ability to do so, and therefore a considerable fraction of the injected dose may be released too early or too far away from the targeted site, which results in low therapeutic effects while inducing negative impacts onto healthy cells.

To overcome the limitation of TACE, a method involving particles being remotely controlled after being released from the catheter is proposed. In previous applications, therapeutic vectors are usually drifted by flow and steered with an external force. The force is usually perpendicular to the flow direction. Physical forces (e.g., electric or magnetic fields, ultrasound (US), hyperthermia or light) have been proposed and researched to supply the steering force [6-11]. In 2007, Prof. Martel proposed a technique now known as magnetic resonance navigation (MRN), which was validated by him and his team by performing *in vivo* MRN of an untethered object in blood vessels using a clinical magnetic resonance imaging (MRI) scanner. With this technique, anti-tumor drugs and

superparamagnetic nanoparticles are encapsulated into biodegradable microbeads which are referred to as magnetic drug-eluting bead (MDEB). The MDEB can be tracked and navigated into the targeted vessels. Compared with other magnetic actuation methods, the main merits of MRN are summarized as follows: 1) The MRI scanner provides a high magnetic field throughout the human body, which ensures a saturation magnetization for the superparamagnetic nanoparticles inside of the MDEBs, even within deep organs inside human bodies; 2) The imaging functions of MRI systems can be used to track the MDEBs, and the magnetic gradients induced by the gradient coils can be used to steer them; 3) Besides the tracking and steering functions, this technique is able to evaluate distributions of MDEBs in the tumors by the T2-weighted MR images [12, 13]; 4) MRN is based on clinical MRI systems, thus avoiding extra costs for purchasing additional equipment.

However, in previous MRN researches, most of the experiments were performed *in vitro,* owing to the limitations of current technical conditions. As we know, the blood flow velocity in hepatic arteries reaches tens of centimeters per second, which is much higher than the steering velocity induced by the magnetic gradient of the clinical MRI systems. It means the particles may potentially have not enough steering displacement to enter selected branches because of the high velocity generated by blood flow, ultimately leading to lower targeted efficiencies [9, 14-18]. Besides the steering function, when achieving the imaging of MDEBs, several seconds or a few minutes are generally required to detect them [7, 19, 20]. It is far from being adequate for real-time tracking of small doses of carriers when they are being pushed around by the arterial circulation because of large position errors, especially in deep tissues. Many methods and technologies focusing on the increase of the steering force and imaging speed have been proposed [19, 21, 22]. However, few reports have been found in the drifting method of particles to generate a low and stable aggregate velocity, and thus ensuring high MRN success rates. Thus, one of the scientific contributions of this thesis is to reveal navigation characteristics of particles in low-velocity flow and to propose the appropriate flow pattern to increase MRN success rates.

Due to the nature of the system, magnetic forces induced by gradient coils are always uniform in the MRI bore, which means MRN is not capable of simultaneously navigating several particles to different directions. Moreover, considering the fact that MDEBs are generally within tens to hundreds of micrometers while the internal diameter of the first two-level of the hepatic arteries is about several millimeters, injecting particle aggregates is a better choice when compared to single-

particle injections, which decreases the injection time as well as the therapy time. In multi-bifurcation MRN, each individual aggregate needs to reach the targeted branch before the injection of the next one. In addition, in order to adapt to different sizes of blood vessels and to estimate the amount of drugs injected, the aggregate size and particles number per aggregate both need to be controllable. Thus, the second scientific contribution of this thesis is to design an MRI-compatible injector which has the ability to inject uniform particle aggregates with the controllable sizes and particle numbers.

Flow control, particle injections and MRN sequences have interlinked with a very high complexity since the synchronization between aggregate injections and MRN is complicated. Indeed, several questions are still existing: 1) How to determine the aggregate sizes for them to adapt to the different sizes of blood vessels; 2) Which MRI sequences can perform high spatial resolution and within a short acquisition time; 3) How to appropriately determine an appropriate duty cycle of imaging and navigation functions in the MRN sequence; 4) How to ensure that the entire system works together during MRN. Thus, the third scientific contribution of this thesis is to solve the questions mentioned above, in order to achieve the synchronization between the aggregate injections and MRN in a two-bifurcation phantom.

To address the problems above, I have therefore made the following assumptions:

1.2 Objectives, hypothesis and general methodology

The general objective of this study is to propose a flow pattern, an MRI-compatible injection system and a simple MRN sequence to achieve successful MRN in a two-level bifurcation phantom. More particularly, the envisaged steps are as follows:

Objective 1 is to evaluate the research hypothesis 1:

Oscillating flow consisting of vibrating flow and constant flow is capable of increasing MRN success rates even if the magnetic gradient is no more than 40 mT/m.

Objective 1:

• Propose a flow pattern to increase the manipulation capability of aggregates in a liquid.

• Experimentally demonstrate that the combination of vibrating flow and constant flow can increase MRN success rates of aggregates in a liquid.

Objective 2 is to evaluate the research hypothesis 2:

It is possible to design an MRI-compatible injection system to precisely and repeatedly generate and inject particle boluses with a desired particle number and, correspondingly, aggregate size.

Objective 2:

• Demonstrate that infrared photoresist devices can be used to determine the amount of microparticles in the high magnetic field induced by a clinical MRI system.

• Propose the MRI-compatible injection system based on the desired aggregate size for liver embolization.

• Experimentally test the proposed system.

Objective 3 is to evaluate the following research hypothesis 3:

Integration of the previously proposed flow pattern in objective 1, the MRI-compatible injection system in objective 2, and a proposed MRN sequence here can be used to form size-controllable microparticle aggregates, track their movements and steer them into selected end-branches of a two-level bifurcation phantom that mimics realistic physiological conditions.

Objective 3:

• Propose a theoretical model to determine the most appropriate size for each particle aggregate for MRN;

• Propose a simple MRN sequence to navigate and track particle aggregates;

• Integrate the flow control method, particle injector and MRN sequence to achieve successfully MRN in a two-level bifurcation phantom.

This thesis is presented and organized in the format of a manuscript-based (article-based) thesis. The following content has eight chapters. Chapter 2 gives the background of MRN and lists the relevant literature reviews on liver embolization. Chapter 3 shows the process of this research project and the methods used for achieving the objectives above. Chapters 4, 5 and 6 show the main original contributions of this thesis, which includes two published and one submitted articles. Chapter 7 includes a general discussion of the methodological aspects and results linked with the critical literature review. At last, the conclusion section summarizes the contributions of this thesis and proposes recommendations for possible future works.

CHAPTER 2 LITERATURE REVIEW

This chapter makes a comprehensive literature review to explain the current problems and possible methods for this project.

The first part focuses on the incidence, diagnosis and treatment of HCC. Among different types of treatment techniques, TACE was introduced for more details.

Subsequently, two MRI-based targeted navigation methods, MR-guided catheter navigation and dipole field navigation (DFN), were investigated to improve the targeting efficiency of the traditional TACE technique.

At last, I introduced the MRN technique which is my research topic. The technique is divided into several sub-steps: design of magnetic microparticles, sizing of particle aggregates, and navigation and tracking of the magnetic particles. In the magnetic particles' design section, the used materials and appropriate particle sizes were introduced. Then, the reason behind why appropriate-sized aggregates need to be made was explained, followed by the current situation of lacking necessary injectors that can meet the demand for MRN. After being released from the catheter, particle aggregates will move through the circulatory system, via blood flow, and the magnetic gradient will steer them into the desired vessel branch. Thus, in the next part, the magnitude of magnetic gradients achievable by a clinical MRI system is introduced. This is to better understand why blood flow needs to be reduced. Then, several medical methods are introduced to block or reduce blood flow, and it was found that the balloon catheter is the most appropriate choice for controlling blood flow because it is easily placed and removed. At last, different MR imaging sequences and their effects are compared with each other in order to select the appropriate sequences for measuring the blood flow velocity, tracking particles during MRN, and assessing particle distributions after MRN.

2.1 HCC

2.1.1 Incidence of HCC

There were 14 million cancer cases in 2012 and the data were predicted to increase to 22 million over the next 20 years [23]. Among them, more than 700,000 new cases are diagnosed as HCC every year. HCC has become the 5th most common cancer in men and the 7th most common cancer

in women [24]. Moreover, it is the third most common cause of cancer-related death that is exceeded only by lung and stomach cancers, more than 600,000 people died of this disease each year [25].

The incidence rates of HCC have a clear geographical distribution. Generally, the incidence rate is low in developed regions. The highest incidence rate occurs in developing countries, such as East Asia, Sub-Saharan Africa, and Melanesia, where around 85% of the population is affected by HCC and where hepatitis B virus infections are endemic [23, 26]. Figure 2-1 shows the incidence rates of HCC in different regions of the world.

Moreover, the incidence rates of HCC are closely linked to age and gender. Individuals below 40 years of age are rarely touched by HCC, and HCC rates reach a peak in the population of approximately 70-79 years of age. The prevalence rate of men is 2 to 4 times higher than that of females.

Figure 2-1: Reproduced from [24]. Incidence rates of HCC in different regions of the world.

2.1.2 Diagnosis of HCC

Diagnosis techniques generally include two main components: invasive and non-invasive. The invasive method relies on measuring liver functions or analyzing liver samples. In the last few decades, noninvasive imaging, including ultrasound (US), computed tomography (CT) and magnetic resonance imaging (MRI), has become an effective method for the diagnosis of HCC [27, 28]. Every method has its merits and weaknesses. However, until now, there is not a single imaging technique that can reach 100% correct identification of all HCC.

2.1.2.1 Measuring the liver function through blood tests

Liver function tests, also called a liver panel, belong in the group of blood chemistry tests. Although alpha-fetoprotein has been considered as the only specific blood test which can be used towards a diagnosis of HCC, its sensitivity for HCC less than 3 cm is only 25% and it goes only up to 50% for lesions more than 3 cm in diameter [29]. Until now, other serum biomarkers have not demonstrated their diagnostic accuracy. However, blood tests can be used as a reference for whether there is possibly a liver pathology. The tested substances include albumin, bilirubin, prothrombin time, etc. For example, after liver cells are damaged, the generated amounts of albumin will decrease.

2.1.2.2 Getting the sample of liver tissues for laboratory testing (biopsy)

Before 2000, an accurate diagnosis of small liver nodules mainly relied on biopsies. Now, in many cases, based on the suggestion from many medical societies, this technique is not necessary [30]. There are still some practitioners who advocate the need for a biopsy since they can then accumulate tissue samples that can be used for research purposes.

When using a biopsy for HCC diagnosis, the overall sensitivity is about 90%. However, the value is variable. For example, the sensitivity reduces to 83% when the size of HCC lesions is less than 1 cm and the value can go up to 70% when the targeted biopsies of lesions are just in the posterior and superior segments of the liver [31].

2.1.2.3 US

US is a low-cost method when compared with other types of scans, such as CT and MRI. Another merit of using the US is that this technique does not involve ionizing radiation or injected

intravenous contrast material-a chemical liquid in order to improve the imaging contrast. However, the diagnostic accuracy of this technique relies highly on the skills of the technician or radiologist performing the scan. To further improve the sensitivity of standard US by means of technology, utilizing microbubble contrast agents allows vascularity of the lesions possible [23]. After using contrast-enhanced ultrasound for HCC diagnosis, based on the survey from 317 patients, a study has demonstrated that the technique had a sensitivity of 90%, a specificity of 99%, and a diagnostic accuracy of 89% [32]. However, this technique still difficultly differentiates adequately cholangiocarcinoma from HCC.

2.1.2.4 CT scans

CT scans can be as sensitive as the US with the help of enhancing contrast agents. Unlike the US, CT scans are much less operator-dependent. Generally, a CT scan is often chosen to investigate further when a liver nodule is detected by the US [33]. CT has a fairly high specificity for detecting HCC. It has demonstrated that, by the 4-slice CT scan, the specificity of HCC diagnosis is above 90% with a 65%–79% sensitivity [34]. Now, the 128-slice CT is more generic in clinical diagnosis, which results in higher specificity and sensitivity [35].

Hepatic angiography may be carried out if other noninvasive imaging methods cannot find any signs of HCCs while the patient is at high risk. After the insertion of a catheter into hepatic arteries, iodine contrast material is injected. If the tumor is found during angiography, TACE may be used for HCC therapy.

2.1.2.5 MRI

MRI is an attractive option for HCC diagnosis because no ionizing radiation is involved. If necessary, the imaging can be repeated many times with little or no risk. When HCC tumors are more than 2 cm, standard gadolinium-enhanced MRI has a sensitivity of more than 90% and a specificity of at least 95% to detect them [36]. However, the sensitivity of standard MRI can drop to less than 30% when HCC tumors are less than 2 cm [37].

Besides the problems in the diagnosis techniques, many countries still lack consistent guidelines in terms of the non-invasive diagnosis [22, 28, 29]. Figure 2-2 gives EASL–EORTC Clinical Practice Guidelines proposed by the European Association for the Study of the Liver and European Organization for Research and Treatment of Cancer.

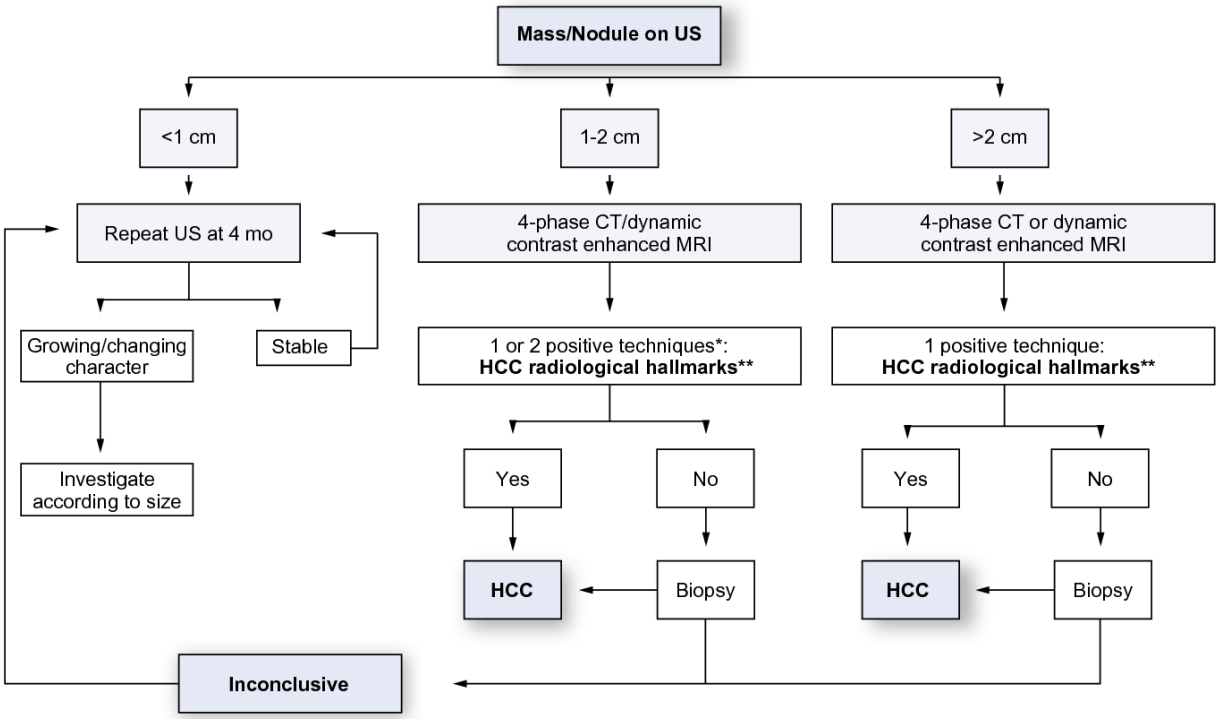

Figure 2-2: Reproduced from [23]. Diagnostic algorithm and recall policy of HCC.

2.1.3 Therapeutic approaches for HCC

2.1.3.1 General treatment recommendations

According to the data from [38], the 1- and 3-year survival rates are 20% and 5%, respectively, with a median survival of 8 months, after HCC treatment.

Treatment approaches depend on the severity of the liver disease, and on access to complex treatment regimens. Among different treatment algorithms, the Barcelona Clinic Liver Cancer staging classification system (see figure 2-3) is most commonly used to determine the optimal therapeutic method after conjunction with the Child's Pugh score [39]. When patients have stage 0 disease (the tumor nodule is smaller than 2 cm and the portal pressure/bilirubin is normal), resection is generally chosen for the patient. Transplantation is the treatment choice for patients with cirrhosis when a single nodule < 5 cm, or a maximum of three nodules, each < 3 cm [40]. If the patients are in stage 0 and A but not suitable for transplant, locoregional therapies, such as radiofrequency ablation and percutaneous ethanol ablation, are recommended. For patients with the multinodular disease (Stage B), TACE is first considered. The patients with portal vein invasion

or disease outside the liver mean that they are in Stage C. For those patients, sorafenib is recommended. If patients in stage D (decompensated cirrhosis), palliative treatment is preferred.

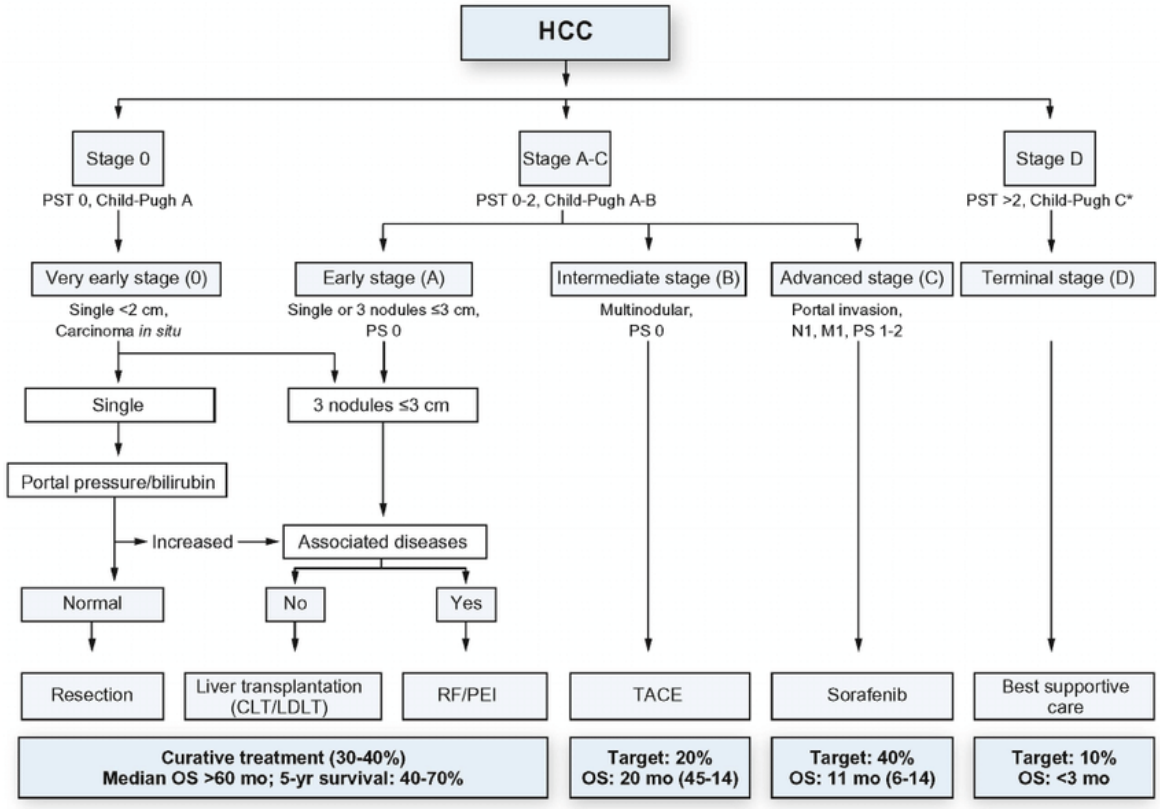

Figure 2-3: Reproduced from [41] and [42]. Barcelona Liver Cancer Staging system with treatment recommendations. Abbreviations: RF, radiofrequency ablation; PEI, percutaneous ethanol injection.

2.1.3.2 TACE

In this section, the TACE technology is described in detail, which includes: the principle, the operating procedure, the catheter selection and the induced limitations, the used drugs and their dosage, the materials of embolization agents, and a simple introduction of the DEB-TACE method.

TACE derives its beneficial effects through the special operating mechanism of the liver: blood vessels feeding the tumor are mainly supplied from hepatic arteries while other liver tissues are fed by blood from the portal vein. Therefore, TACE can interrupt the tumor's blood supply without affecting the rest of the liver or body. Despite blocking the vessels feeding the tumor, targeted release of the drugs allows delivery of a higher dose to the tumor tissue while reducing systemic

exposure, because the chemotherapeutic drug will not be washed out by blood flow since it is embolized near the tumor.

TACE procedure is performed in the angiography suite. Prior to TACE, a thorough angiography will be performed after selective catheterization of the hepatic artery with a 4 or 5 French catheter to locate all the feeding arteries of the tumor, as well as any possible extrahepatic arteries that may feed the tumor [43]. After that, a 2 to 3 French microcatheter is advanced coaxially, selectively into the feeding arteries of the tumor. Alternating injections of anti-tumor drugs and embolic particles will be performed through the catheter to infuse chemotherapy and block tumor circulation. Superselectivity and complete coverage of the HCC nodules with the chemoembolization are necessary to maximize therapeutic response [44]. However, the high selectivity of this method mainly relies on the physician's skills [45, 46]. On some occasions, catheterization needs to be performed repeatedly, increasing the time of exposition to ionizing X-ray radiation for the patient, staff and interventional radiologist. Another limitation of TACE is the visualization of the tumor which is better seen on MRI and sometimes poorly seen using X-ray angiography. In the angio suite, the use of cone-beam CT with selective contrast injection is often recommended to improve the identification of feeding arteries [44].

Based on the statistics, the most common anti-tumor drug is doxorubicin (36%), cisplatin (31%), epirubicin (12%), mitoxantrone (8%), mitomycin C (8%) and SMANCS (5%) [47]. Until now, there are no consistent criteria defining the most suitable dosage of chemotherapeutic agents for HCC therapy. The factors required to be considered include the tumor size, the catheter's position in vessels, the patient's body surface area, patient weight, etc. In early studies, many clinicians prefer to use a fixed dose of drugs. For example, two of the most common drugs, doxorubicin and cisplatin, generally need respectively 40–100 mg and 10–70 mg per patient [48, 49]. Recently, some clinicians determined the drug dose based on the patient's body surface area. In [50], the recommended maximum dose of doxorubicin administered per treatment is 75 mg/m^2. There is also no evidence (randomized controlled trials) of significant differences in survival rates after using the different drugs mentioned above. Sometimes, several chemotherapeutic agents are mixed together instead of using one alone. In the United States, for example, the mixture of 100 mg cisplatin, 50 mg doxorubicin and 10 mg mitomycin C is one of the most common drug combinations [49].

In TACE, the selection of embolization agents is also different. Lipiodol, a poppy-seed oil, is commonly used as an embolization and radio-opaque agent [51, 52]. It is mixed with doxorubicin as a water in oil emulsion. After being injected into the feeding arteries, this material can remain in tumor nodules for several weeks to over a year, allowing it to distribute itself throughout the tumor artery branches and the peritumor portal venules [53]. Moreover, its iodine component is can be evaluated by CT or cone-beam CT [53, 54], which can be used to monitor tumor coverage during TACE procedure. Embolization is performed after chemotherapy infusion using a biodegradable embolizing agent (Gelfoam) or PVA microspheres which are permanent) [44].

More recently, a different approach from conventional TACE which requires the need to inject drugs and embolic agents separately has been developed. Indeed, embolic agents carrying drugs have been tested and proven effective, officially being called drug-eluting beads (DEBs) [55-58]. The DEB-TACE makes the injection of drugs and embolic agents in a single operation, facilitating the targeted and sustained delivery of the drugs. Here, two types of DEBs, DC/LC-Beads® (Biocompatibles, UK) and HepaSphere® (BioSphere Medical, Inc., USA), are commercially available. In both cases, the doxorubicin is encapsulated into polymeric microspheres for HCC treatment. They have been evaluated in clinical studies [59-61]. In [62], the HCC therapy outcomes between DEB-TACE (DC/LC Beads®) and conventional TACE (intra-arterial injection of doxorubicin emulsified in Lipiodol followed by particle embolization with Gelfoam or Poly(vinyl alcohol) (PVA) particles) were compared with each other. The drug-eluting bead (DEB) loaded with doxorubicin showed to be capable of achieving a similar or same therapeutic efficacy while reducing side effects [63]. In the sub-analysis, the authors further showed that DEB-TACE can induce a significantly lower liver and cardiac toxicities. In [64] and [65], similar clinical responses and tolerances were found between these two kinds of TACE methods. However, a lower number of patients with DEB-TACE suffer from post-procedural pain [66]. DEB-TACE with irinotecan has also been used for the treatment of non-resectable colorectal liver metastases [67-72]. The response rate reached 70%. Moreover, the patients had superior survival rates and were found to have a better quality of life, when compared with those administered with intravenous chemotherapy [73, 74]. One important limitation of the DEB-TACE technique is the poor visualization of tumor coverage because the injection of lipiodol becomes impossible after therapy. Cone-beam CT and new radiopaque DEBs are two recently proposed methods to solve the visualization problem [75-77].

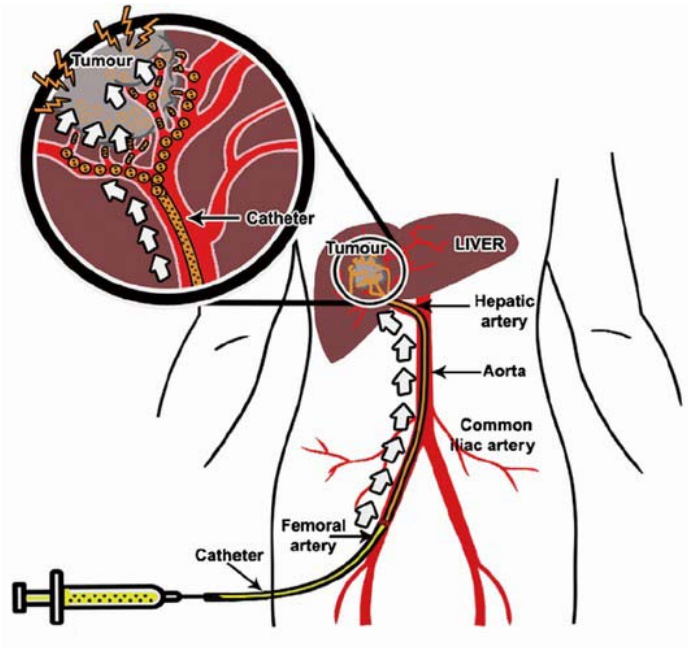

Figure 2-4: Reproduced from [78]. The basic principle of TACE.

In summary, the DEB-TACE technique facilitates the targeted and sustained delivery of the drugs. However, the need for repeated superselective catheterizations and the poor visualization of the tumors under fluoroscopy are the main limitations of this technique. Thus, if the particles can be delivered selectively from an implanted catheter in the main hepatic artery with MR guidance allowing good visualization of tumor extension and coverage, better therapeutic outcomes could be expected. In the next section, the methods aiming to move particles into smaller arteries are introduced.

2.2 MRI-based targeted intervention

Compared with the TACE technique performed under fluoroscopy/cone-beam CT guidance, MRI-based targeted techniques have at least two advantages. First, X-ray fluoroscopy, generate damaging ionizing radiations for patients, physician and other attending persons. The MRI system is non-ionizing. Second, MRI is the best modality to identify HCC extension whereas these lesions can be difficult to detect using digital subtraction angiography under fluoroscopic guidance.

Thus, in this section, I focus on two kinds of MRI-based targeted techniques: MR-guided catheter navigation and DFN.

2.2.1 MR-guided catheter navigation

For a normal catheter, the catheter is operated manually. The physician will rotate the catheter to push it into the desired vessel along a guidewire. The insertion of the catheter and the control of the guidewire tip will become more difficult after the catheter has passed through several vascular turns. Generally, for liver chemo-embolization procedures, a 4 or 5 French diagnostic catheter is used to catheterize the celiac trunk or the proximal hepatic artery. Then, superaselective catheterization of hepatic segmental arteries is performed using a 2 to 3 French microcatheter advanced coaxially inside the diagnostic catheter. This microcatheter is manipulated over floppy micro-guidewires with different angulations depending on the angio-architecture. Since it is important to be selective at the segmental level to maximize therapeutic efficacy, catheterization of all feeders can be fastidious and may require long procedure time and several microcatheters and guidewires.

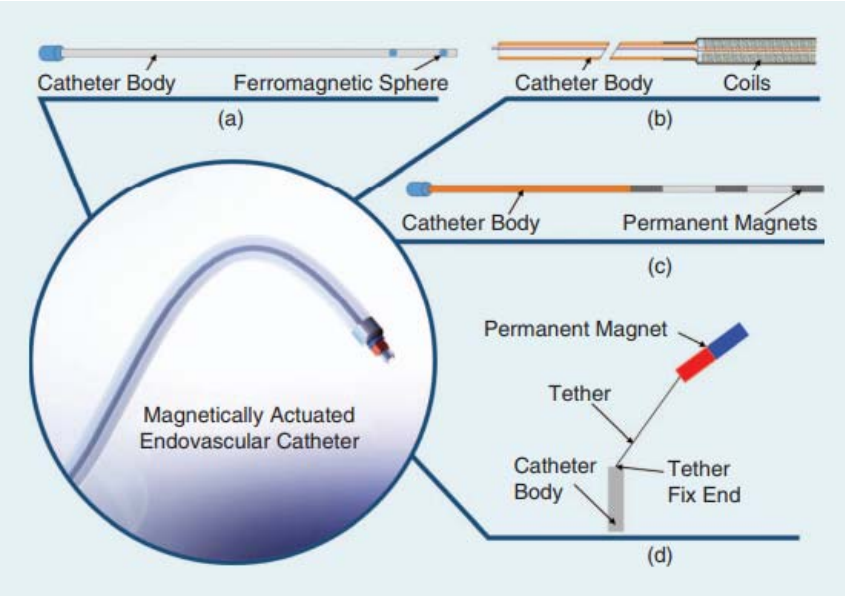

Figure 2-5: Reproduced from [79]. Four different concepts of catheters that can be magnetically actuated.

MR-guided catheter navigation is a promising field of study with significant clinical prospects. Many techniques have been proposed to guide a catheter using the magnetic field of an MRI scanner [80, 81]. The principle is based on magnetic forces. A micro ferromagnetic bead [79, 82, 83] or micro coils [79, 84, 85] are installed on the catheter tip. Using magnetic gradients generated by the imaging coils of an MRI system, it is feasible to push or drag the ferromagnetic bead using magnetic forces, thus inducing a deflection on the catheter tip in any desired direction (see (a) in Figure 2-5). Generally, only low saturation magnetization materials can be used in case they induce

serious interference with MRI imaging. The principle of using micro coils is that when the solenoidal coil is powered on, the catheter tip will undergo the influence of a bending force if the induced magnetic moment and B_0 do not point at the same direction (see (b) in figure 2-5). Hence, the use of coils results in minimal image distortion when the current is off. However, the over-heating problem of coils is an important weakness for this type of methods. In table 2-1, advantages and disadvantages of these two types of MR-guided catheters are listed.

Table 2-1: Reproduced from [79]. Advantages and disadvantages of MR-guided catheters when different components are used on the catheter tip

Catheter Components	Advantages	Disadvantages
Ferromagnetic spheres	● Larger magnetic forces. ● Artifacts caused by spheres can be used for tracking. ● Small spheres can be easily removed to reduce artifacts.	●Multiple ferromagnetic spheres introduce undesired dipole–dipole artifacts. ● Heavy spheres cause the catheter tip to drop and induce large slide friction against vessel walls. ● Only low saturation magnetization materials can be used.
Microcoils	● Can be guided under MR imaging navigation; hence, no radiation exposure. ● Has the potential, as a radio-frequency transmitter-receiver, to enhance imaging of soft tissues near the catheter tip. ● Reduced levels of artifacts can be helpful for tracking of the catheter tip.	● Resonant heating of coils requires additional heat reduction techniques. ● DC current causes imaging-related artifacts. ● Fabrication of microcoils using the laser lathe technique limits the size. ● Microcoils require high magnetic fields and are restricted to active actuation using MR scanners

Although permanent magnets have also been used with magnetically actuated catheters, the external actuators are often electromagnets or permanent magnets (see (c) and (d) in figure 2-5) [86-88].

Once a catheter has reached the targeted blood vessel, the insertion will be stopped, followed by the injection of drugs and/or particles. Currently, there are two injection environments: Fluoroscopy and MRI. As explained above, the MRI system does not provide ionizing radiation to patients while it is not achievable for the fluoroscopy. If therapeutic magnetic micro carriers (MDEBs) need to be injected, an MRI-compatible injector that can precisely control the injection amount becomes indispensable.

2.2.2 DFN

Once subjected to the homogeneous external magnetic field of an MRI system, spherical ferromagnetic spheres become magnetized. The induced magnetic gradient field around the magnetized ferromagnetic cores can navigate MDEBs into desired vessels. This technique is called DFN [89]. DFN can generate strong directional gradients exceeding 300 mT/m in deep tissues, making whole body interventions possible. However, the distorted magnetic field induced by the ferromagnetic cores also affects MR imaging. In order to cope with this problem, the authors proposed a method that solves the above problem by using the gradient force to move the cores away when imaging the injected particles [90]. Two possible problems need to be comprehensively and carefully considered before moving the cores: 1) The presence of the patient in a space-limited MRI bore may make the movement of the cores complex and difficult; 2) To avoid possible dangers, the cores must always be in the uniform field of the MRI scanner.

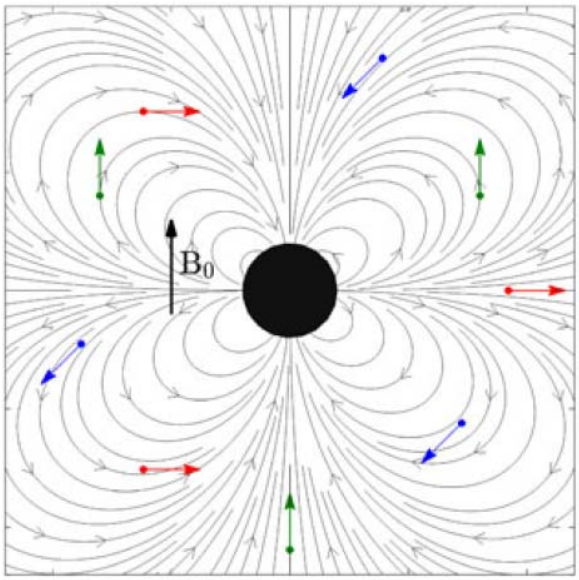

Figure 2-6: Reproduced from [89]. Distribution of the magnetic gradient field around a magnetized ferromagnetic core.

Imaging and injecting particles are done alternately in the DFN technique, which means the injection of MDEBs need to be stopped during imaging. Moreover, when the treatment operation approaches completion, a small amount of MDEBs need to be injected, followed by the MRI check of the embolization effect, until embolization achieves satisfactory results. This requires a controlled injection system to precisely control the amount of particles per injection.

2.3 The MRN based targeted therapeutic intervention and related researches

This section will give a quick overview of the basic principles and related researches of the MRN technique.

2.3.1 Basic concept of MRN

The author's research group has been working on the technique of MRN [9, 22]. The technique uses a clinical MRI system to track and navigate MDEBs to targeted positions within the body through the patients' vascular networks. The MDEBs mainly consist of degradable materials, anti-tumor drugs and magnetic nanoparticles [91-93]. The nanoparticles can be magnetized to saturation by B_0, the main MRI magnetic field. Then, the MRI's gradient coils can, in any direction, generate a magnetic force on a MDEB. In order to navigate a MDEB in vessels where it can drift downstream with blood flow, the gradient force induced by the gradient coils is often used as the steering force,

which ensures that MDEBs are navigated towards the appropriately releasing sites. Moreover, MDEBs are MR-visible because of magnetic susceptibility artifacts [94], which makes the real-time assessment of MDEB distributions in the tumor quite easy.

The process of MRN can be simply divided into the following steps: At the beginning of the MRN-based intervention, an infusion catheter is inserted into the artery and advanced to an appropriate site; Then, the patient is centered into the MRI, followed by MRN of MDEBs.

The magnetic steering force induced by the MRI gradients on a particle can be expressed by

$$\boldsymbol{F_m} = V_p(\boldsymbol{M} \cdot \nabla)\boldsymbol{B} \qquad \text{(Eq. 2-1)}$$

where $\boldsymbol{F_m}$ is the magnetic force and V_p is the particle volume (m^3) (In the MDEB, V_p is defined as the volume magnetization), $\boldsymbol{M}$ is the magnetization of the particle material (A/m), B is the magnetic flux density (Newton-meters per ampere (Nm/A) or Tesla (T)), $\boldsymbol{\nabla B}$ is the spatial variation or gradient of the magnetic field (T/m).

When a particle is moving in a liquid, the magnetic force needs to overcome the fluid resistance induced by the magnetically induced velocity [95].

$$\boldsymbol{U_m} = \boldsymbol{F_m}(6\pi r\mu)^{-\mathbf{1}} \qquad \text{(Eq. 2-2)}$$

where r is particle radius, and μ is the dynamic viscosity of the flow.

Despite the motion perpendicular to vessels, the particle also has a velocity vector along with the blood flow. These two types of motions combine into a deflection motion ($\boldsymbol{U_{defl}}$) in vessels in order to navigate the particle into the targeted areas.

$$\boldsymbol{U_{defl}} = \boldsymbol{U_m} + \boldsymbol{U_f} \qquad \text{(Eq. 2-3)}$$

where $\boldsymbol{U_f}$ is the particle velocity induced by the flow.

When single-direction MRN is considered, a single unidirectional gradient is enough to steer the beads toward the desired side of the targeted bifurcation. The magnetic particles can be continuously injected with an infusion pump, as shown in figure 2-7(a).

For multiple-branches MRN as shown in figure 2-7(b), at least two consecutive gradients are required. Unfortunately, inside an MRI system, only global magnetic forces can be formed. Thus, independent control of multiple boluses becomes impossible. The continuous injection can not be

used anymore because only a single bolus of MDEBs can be navigated at a time. As such, the particle control system needs to have two basic functions: first, the injection must be controllable to release only a single bolus of MDEBs into the bloodstream each time; and second, the particle number in each bolus must be controlled.

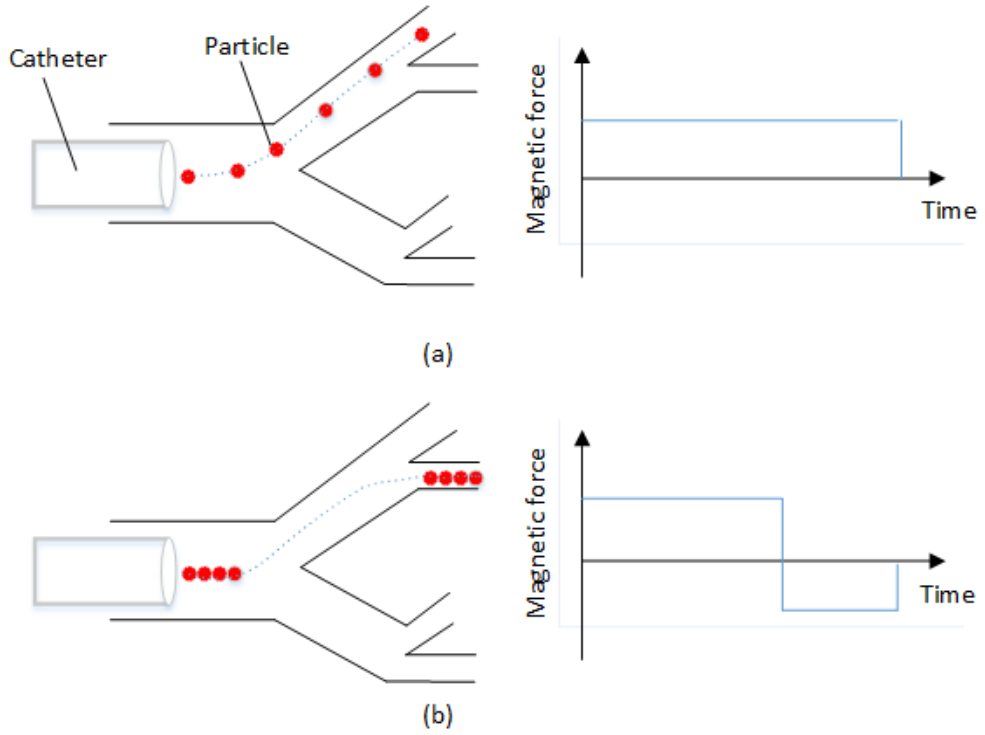

Figure 2-7: Schematic diagram to show the continuous injection (a) and sequential injection (b).

2.3.2 Magnetic microparticles used in MRN

2.3.2.1 Materials and sizes of MDEB

MRN-based embolization requires appropriate MDEBs in terms of materials and sizes [96]. Generally, MDEB mainly consists of degradable materials, anti-tumor drugs and magnetic nanoparticles [91-93]. The detailed reasons are as follows:

1) Degradable materials based MDEBs can temporarily block the arteries supplying blood to the tumor. After tumor cells are killed and cleared, the normal blood circulation can be restored. Among different types of materials, Poly (lactic-coglycolic acid) (PLGA), a material that has been approved by the Food and Drug Administration (FDA) [97], attracted a lot of attention because of

its biodegradability, biocompatibility and controllable degradation rate [98, 99]. Alginate is another widely used encapsulation material that is biodegradable and biocompatible [100, 101]. These two materials have different encapsulating principles: interfacial precipitation is often used for PLGA encapsulation while alginate crosslinked matrix can be formed when contacting divalent cations [102].

2) Anti-tumor drugs are slowly released to the tumor as a mean to kill the cancerous cells during the slow decomposition of the MDEBs while also reducing its toxicity and increasing its therapeutic effect.

3) Those magnetic nanoparticles are superparamagnetic, and thus they can be magnetized by the uniform magnetic field of the MRI scanner while not keeping any net magnetization once the patients are removed from the MRI system. Moreover, the particles can be phagocytosed because they are nanosized (5-20 nm) [103, 104]. Despite size requirements, the biocompatibility of the nanoparticles is also an important consideration before using MDEBs. In [105], iron-cobalt nanoparticles (FeCo) possessing a high saturation magnetization of 209 emu/g were synthesized. The particles exhibited good performances in both imaging and navigation operations during MRN. However, this material, FeCo, is in general not regarded as biocompatible. In [106], magnetic iron oxide nanoparticles were synthesized and then encapsulated into PLGA-based microspheres. The microspheres were considered to be biocompatible.

After choosing the appropriate materials for MDEBs, the sizes of embolic agents must be determined with regards to the dimensions of target arteries. The particle size that has been used for MRN ranges from tens of micrometers to a millimeter [107]. In [108], an *in vivo* rat model was used and the results revealed that the particle size should be at least 40 μm. The smaller ones may distribute to non-targeted organs, such as the lungs. In [109], the particle size that is larger than 50 μm was recommended to avoid passage through the liver. Considering the fact that 4 or 5 Fr catheters with 0.035- or 0.038-inch inner lumen are often used in liver embolization, the particle sizes larger than 1,000 μm can potentially obstruct catheters. In [110], [111] and [112], it has been demonstrated that 100–300 μm is the appropriate size of microparticles for liver chemoembolization because the particles of this size range can reach the proximity of the tumor margin while offering a high quality of MR imaging.

2.3.2.3 Magnetic particle aggregates in MRI

Magnetic particles have a strong tendency to agglomerate in magnetic fields due to dipolar interactions. The importance of using particle aggregations has been introduced in several previous works [113, 114].

The justification for using particle aggregates in MRN involves the main considerations below:

1) The recommended particle size is generally much smaller than the vessel diameter. As explained above, it has been demonstrated that 100–300 μm is the appropriate size for microparticles for liver chemoembolization. Considering the fact that the internal diameter of the first two branches division of hepatic arteries is in the range of 3 to 5 mm. Thus, injecting aggregates can significantly decrease the therapeutic time when the total amount of particle injections is fixed.

2) A larger magnetic volume induces a higher magnetic propulsion force to counter the viscous friction force, hence facilitating magnetic steering during MRN.

In the research of magnetic particle aggregates in the MRI system, Jean-Baptiste Mathieu et al. [115] have studied the phenomenon of magnetic aggregations in an MRI system. The data demonstrated that, along the B_0 direction, the formed particle aggregates have the longest axis also referred to as the easy axis.

To form particle aggregates and use them in MRN, an injector prototype composed of a bead capture and a bead detection system was proposed by Alexandre Bigot et al. [116]. The capture subsystem used copper wire coils to generate local magnetic forces, trapping the magnetic beads in laminar flow, as shown in figure 2-8. The detection subsystem was composed of two identical coils, one emitter and one receiver. The emitter was excited by the resonance frequency, inducing a magnetic coupling structure. When a bead entered the space between the two coils, the natural resonance frequency changed and thus the output of the receiver shifted, which was also used to solve the issue concerning the synchronization between the injector and MRN software. However, the injector prototype is not capable of controlling the number of particles per aggregate. Another concern is that the controlled beads were made of chrome steel and had a size of 0.8 or 1.0 mm in the experiment. Such high-magnetization materials combined with large dimensions only require low-power coils to trap the flowing beads, hence generating less heat. The increase in temperature

is actually an important issue that should be comprehensively considered when using MDEBs, all of which will be introduced below.

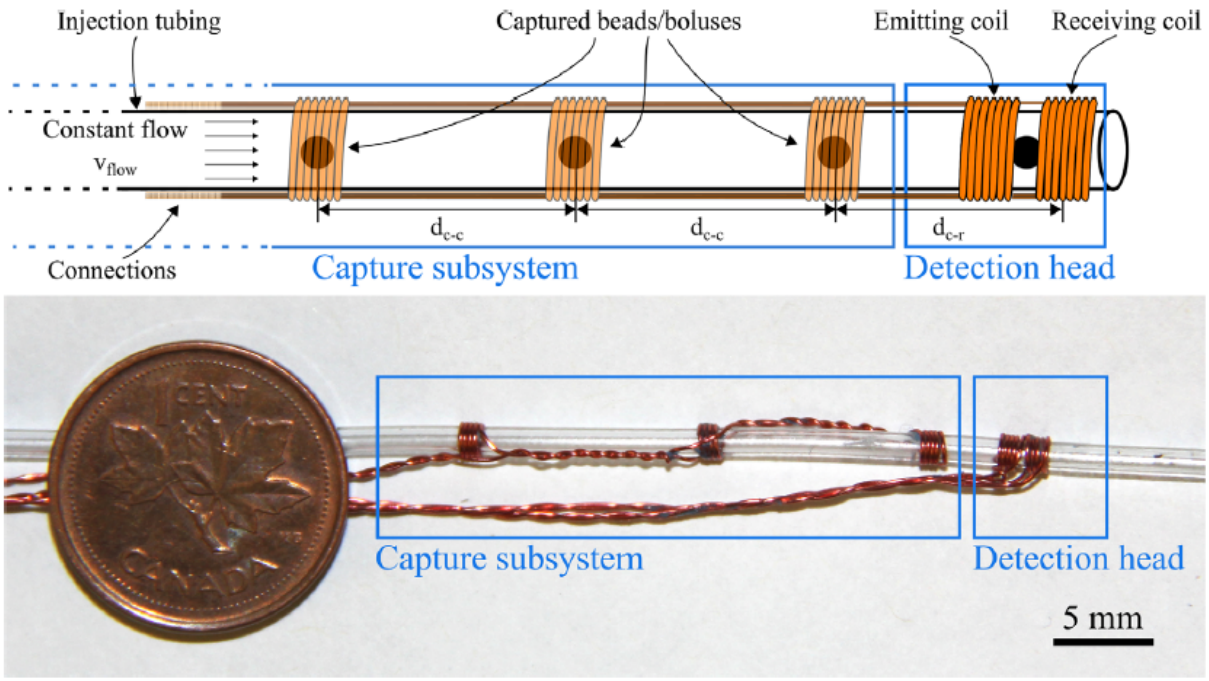

Figure 2-8: Reproduced from [116]. A prototype of the injector to control and to detect the release of magnetic beads.

2.3.3 Magnetic gradient for MRN

The gradient supplied by imaging coils of clinical MRI systems is typically limited to about 40 mT/m in any direction. Under such values, navigated objects are generally ferromagnetic and sizes are in the millimeter ranges [93]. As explained above, the preferred magnetic material in MDEBs is superparamagnetic nanoparticles (5-20 nm). Compared with ferromagnetic materials, the superparamagnetic particles own a much smaller magnetization. Moreover, a smaller size of MDEBs makes MRN harder since the particles' velocity and the induced magnetic force acting on them decrease at, respectively, quadratic and cubic rates with particle sizes. Thus, higher gradients amplitudes are required.

In [17], [105] and [117], an upgraded imaging coil (see figure 2-9) was inserted into the MRI bore to supply a magnetic gradient as high as 400 mT/m. In [17] and [105], iron-cobalt nanoparticle-based MDEBs were successfully navigated *in vivo* through one bifurcation of a rabbit

liver with a gradient of 400 mT/m. Then, with the help of the upgraded imaging coil, Alexandre Bigot et al. [117] successfully achieved navigation of a 1-mm Chrome-Steel bead in a three-level bifurcation phantom. However, the limitation of using the upgraded coils is also quite apparent since such coils have a small inner diameter, which could not fit any human bodies. In [118], an ultrahigh gradient MRI scanners, capable of supplying up to 300 mT/m gradient, was proposed. However, the high cost for such equipment limits its wide application.

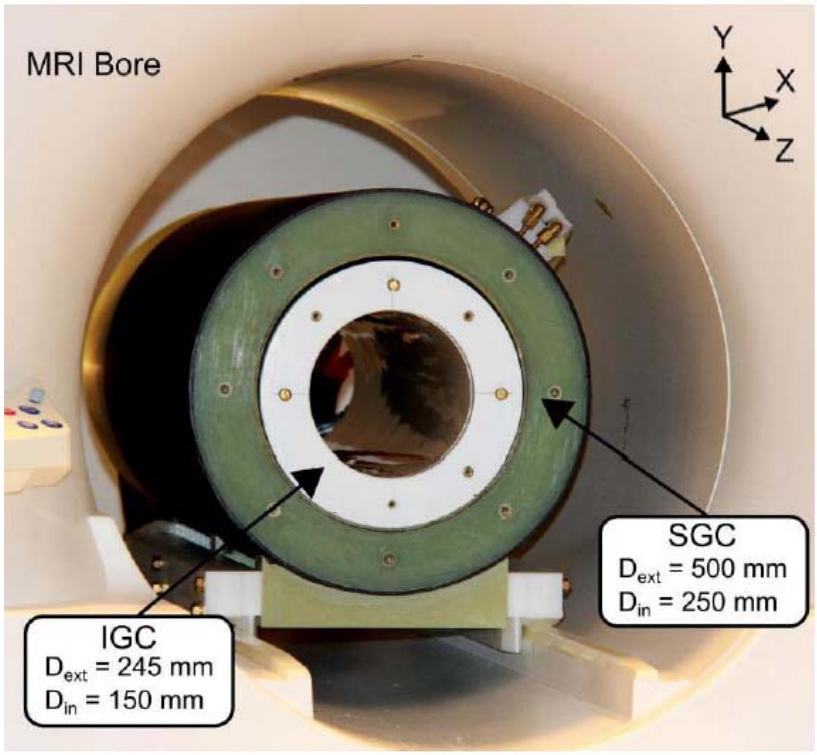

Figure 2-9: Reproduced from [117]. The upgraded imaging coils capable of supplying a magnetic gradient as high as 400 mT/m. Abbreviations: IGC, imaging gradient coil; SGC, steering gradient coil.

In summary, when doing MRN in a wide range of body size, using a high magnetic gradient is expected but is difficult to be obtained under current technical conditions.

2.3.4 Blood flow control during MRN

As explained above, inside the MRI scanner, increasing the magnetic gradient force is difficult. Moreover, blood flow in human vasculature usually has a very high velocity. Figure 2-10 shows the blood velocity and Reynolds number in different sizes of vessels. The common, right and left

hepatic arteries have respectively internal diameters (mean ± standard deviation) of 4.5 ± 0.3, 3.0 ± 0.3, and 3.6 ± 0.4 mm [119]. The blood velocity in the hepatic arteries can be tens of centimeters per second.

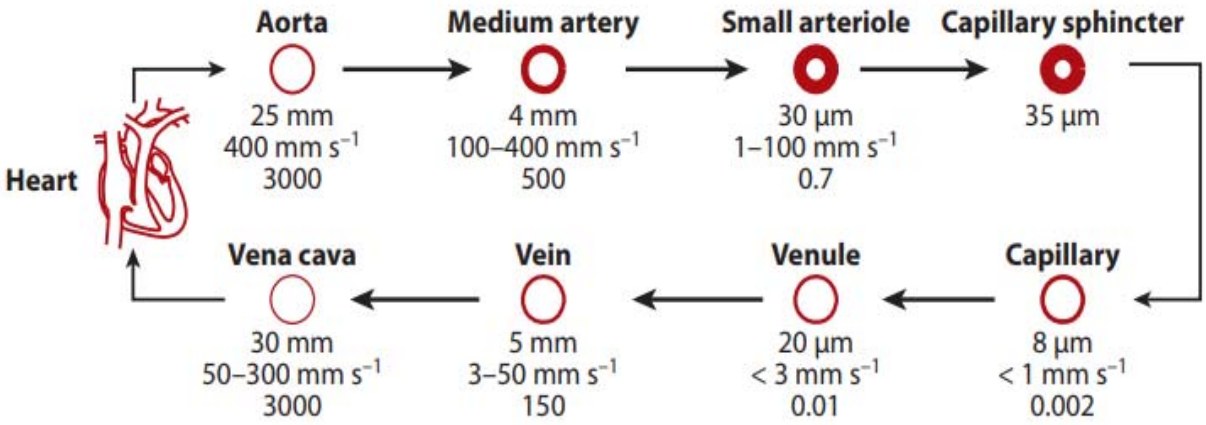

Figure 2-10: Reproduced from [120]. Schematic representation of the blood flow velocity and Reynolds number as a function of vessel size.

In [121], a microfluidic device was designed to evaluate the effect of MRN on the deflection pattern of magnetic aggregations as a function of fluid flow velocity. Even if the magnetic gradient amplitude was 400 mT/m, the deflection patterns were only discernable when the flow velocity was several millimeters per second. This means the particle velocity induced by blood flow has to be reduced in order to increase the MRN success rate. Thus, here, decreasing the blood's movement and thus its speed is considered as an optimal method.

In this section, I will give a quick review of different devices used to block or reduce blood flow. Table 2-2 lists the advantages and disadvantages of different devices for blood control.

Table 2-2: Advantages and disadvantages of different methods for blood control

	Advantages	**Disadvantages**	**Precise control of blood**	**Possibility of MRI-compatible**
Coils [122]	Wide range in the coil characteristics and good for fast-flowing vessels	Large coils can disrupt the radiographic image	N	Y
Detachable Balloons [122, 123]		Removed from the market		
Amplatzer Vascular Plug [123, 124]	Ease of deployment	Permanent large-vessel occlusion	N	Y
Balloon catheter [125, 126]	Easily placed and removed and allow simultaneous injection of MDEBs or fluids	Risk of leakage	N	Y

The coil, one of the most widely used embolic agents, has diameters from submillimeter to several centimeters [127]. This device relies on thrombogenic responses to block blood flow. In order to adapt to different vessel structures, the configuration is variable, such as helical, straight, spiral, etc. Many coils have small fibers attached to the metal component, increasing the thrombogenic response. Multiple coils can also be used to further increase the occlusion effect.

The detachable balloon [122, 123, 127] has many critical limitations, such as rupture risk and potential migration, which cause it to be prohibited by the market of the United States.

Amplatzer Vascular Plug [123, 124], consisting of a noncovered nitinol mesh, is usually used for permanent large-vessel occlusion. Generally, the device has a diameter of 4 to 16 mm. For a single-mesh device, the size should be oversized 30 to 50% relative to vessel diameter in order to prevent distal migration. For the multi-mesh devices, the value is 15–30%

The balloon catheter is composed of two coaxial tubes and one inflatable "balloon". The internal tube is used for injecting drugs or particles, and the external tube is to control the balloon. Generally, a catheter is inserted into vessels under fluoroscopic guidance. When the catheter tip reaches the desired position, the balloon is inflated by injecting liquids into a co-axial channel. This inflation makes the balloon compress against the vessel wall, stopping or decreasing the flow velocity in the vessel. This method has been widely used to prevent or minimize bleeding during surgery [125, 126]. The balloon catheter is also easily removed out after deflating the balloon. Besides the functions above, the balloon catheter, a multi-function device, can also be used to enlarge a narrow vessel, install stents in vessels [128], and block a reflow when performing embolization procedures etc.

From table 2-2, it is easy to find that the existing devices are hard to achieve precise control of blood flow. However, the balloon catheter is an appropriate choice for controlling blood flow because it is easily placed and removed.

The concept of controlling the blood flow by using the balloon catheter has been tested *in vivo*. A 5 French compliant occlusion balloon catheter (Fogarty, Edwards Lifesciences, Irvine, CA) was inserted into the proper hepatic artery while keeping the catheter tip about 3-4 cm away from the right-left bifurcation. The 2D phase-contrast cine sequence validated the capability of controlling flow in hepatic arteries when inflating the balloon catheter [129]. For the details, please see Appendix B.

2.3.5 MR imaging and tracking technique

In the MRN technique, the MRI system has four main functions: provide the steering force, measure the blood flow rate, track particle motions, and assess particle distributions. The first function has been introduced above. The remaining three functions will be introduced in the content of this section. Although the research study of identifying the vascular path plays a crucial role in enhancing the steering efficiency, such operations often occur before MRN. Here, the techniques about identifying the vascular path will not be introduced.

The organization of this section is as follows: 1) the basic principle of the MRI system; 2) two basic imaging sequences, followed by the selection of appropriated sequences for assessing particle distributions after MRN; 3) the appropriate MR sequences for tracking particle motions; and 4) the MR sequences for measuring the blood flow rate.

2.3.5.1 Basic principle of MRI

When a human body is in a magnetic field, hydrogen nuclei will be aligned with the B_0 direction (figure 2-11). The nuclei precess around B_0 with the frequency of the Larmor frequency, which is called Larmor precession. The frequency is:

$$w_0 = rB_0 \qquad \text{(Eq. 2-4)}$$

where w_0 is the Larmor frequency, r the gyromagnetic ratio and B_0 the strength of the magnetic field. The nuclei are charged particles, thus creating a net magnetic moment, M, parallel to B_0.

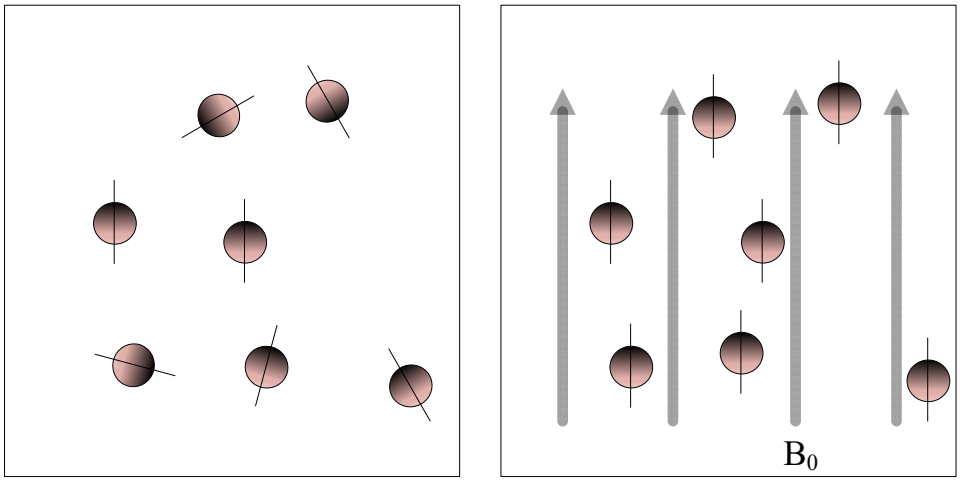

Figure 2-11: Hydrogen nuclei are randomly aligned (left). In a strong magnetic field, B_0, the hydrogen nuclei precess around the direction of B_0 (right).

Then, a radio-frequency (RF) pulse, which is perpendicular to B_0 and equal to the Larmor frequency, is applied to cause M to tilt away from B_0. Once the RF signal is removed, M repoints in the B_0 direction and the nuclei can release energy through RF signals. The signals are received by the imaging coils in the MRI system. Magnetic field gradients localize the signals in space to obtain 3D MR images. By changing the parameters of the RF pulse, different contrasts will be generated between tissues because of the different relaxation properties of the hydrogen atoms therein.

T1 and T2, two different relaxation times, are a time constant at which the excited protons repoints in the B_0 direction. T1 is the time constant of longitudinal relaxation while T2 (transverse relaxation time) is the time constant of transverse relaxation. However, the excited protons may not have a true "relaxation" process because of magnetic field inhomogeneity. The corresponding

transverse relaxation time constant is named T2*. Generally, T2* is much smaller than T2. Their relationship is as follows:

$$\frac{1}{T2^*} = \frac{1}{T2} + \frac{1}{T_{inhom}} = \frac{1}{T2} + \gamma \Delta B0 \quad \text{(Eq. 2-5)}$$

where T_{inhom} is inversely proportional to the magnetic field inhomogeneity, γ is the gyromagnetic ratio and $\Delta B0$ is the difference of the varying field [130].

2.3.5.2 Particle imaging through spin echo (SE) sequences and gradient echo (GRE) sequences

In this section, two types of MR imaging sequences are explained and discussed. The susceptibility effect induced by the presence of magnetic particles is introduced in detail. The purpose of doing such things is to select appropriate MR sequences used for tracking particle motions and assessing particle distributions during and after MRN.

The phenomenon of SE was first introduced and explained by Erwin Hahn in 1950 [131]. Then, in 1954, Carr and Purcell developed SE by using a 180° refocusing pulse as the second pulse [132].

In a common SE sequence (figure 2-12), a 90° pulse will induce an excitation able to flip the longitudinal magnetization into transversal magnetization. Then, due to magnetic field inhomogeneities, spins experience a dephasing process, resulting in delays of transversal magnetization with the time constant T2*. In this stage, some spins (lower local field strength) slow down and start trailing behind, while some others (higher field strength) speed up and begin to get ahead of the others. After half of the desired echo time (TE), a 180° pulse will be used to rephrase the dephased spins, which results in the following phenomenon: slower spins move ahead of the main moment and the fast ones begin to trail behind. In the next half of TE, the fast and slow moments move toward the main moment. Therefore, complete refocusing occurs right after TE.

The SE sequence's advantageous point is that it is insensitive to magnetic field inhomogeneities. However, the waiting interval between SE experiments is long since longitudinal magnetization must be recovered through the T1 relaxation process after each SE sequence, resulting in a long scanning time.

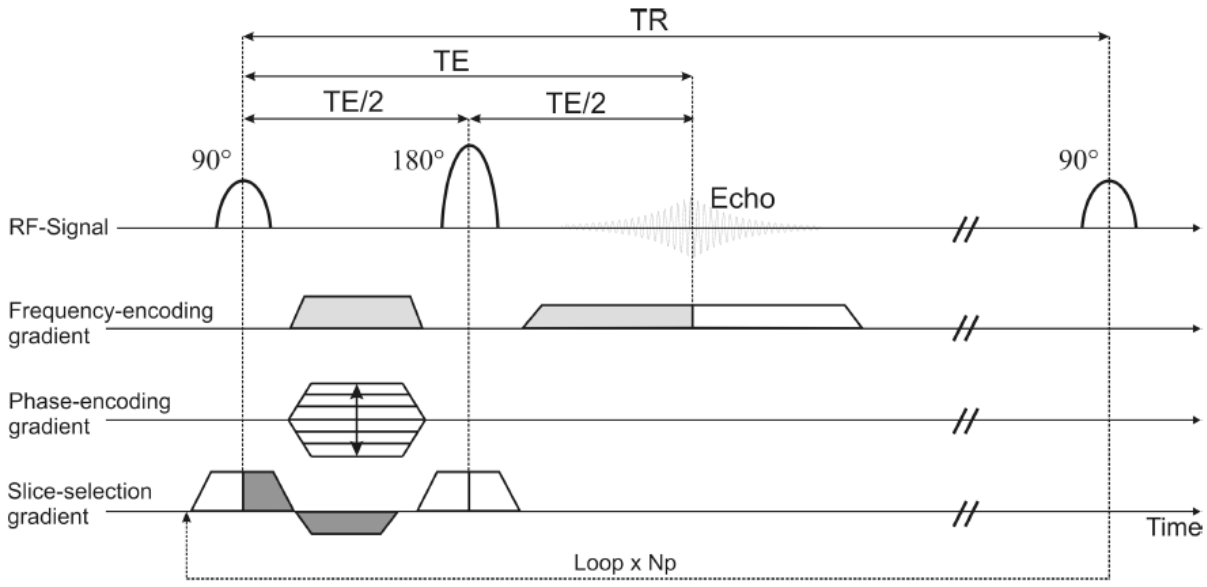

Figure 2-12: Reproduced from [133]. SE sequence.

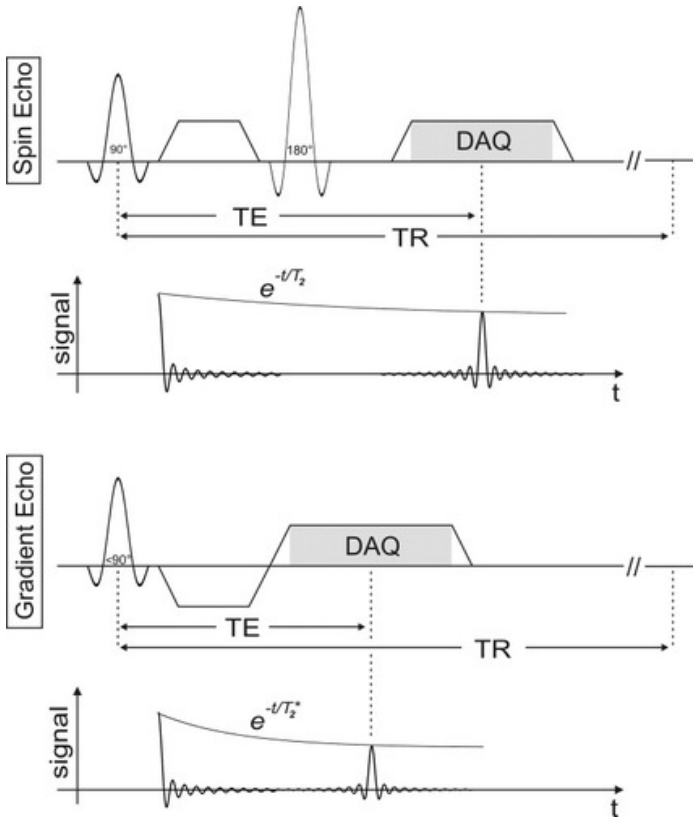

Figure 2-13: Reproduced from [37]. SE pulse (top) vs GRE pulse (bottom). Abbreviation: DAQ, data acquisition.

Compared with the SE which requires pairs of RF pulses, a signal RF pulse and a gradient reversal are enough to generate GRE images (Figure 2-13). The principle of GRE is as follows: 1) An RF pulse will induce processing spins; 2) The spins will experience a phase dispersion because of the first negative-ongoing lobe of gradient; 3) The spins will be refocused after the gradient is reversed, resulting in a gradient (recalled) echo.

Once put in the MRI scanner, superparamagnetic objects can be magnetized because of the presence of B_0. An MRI system works using the following principle: the nuclei precess around the B_0 with the frequency of Larmor frequency. Thus, the magnetized object induces an inhomogeneity in B_0, which creates a variation in the precession and causes susceptibility artifacts in the MR images. Magnetic susceptibility can be measured by the material's ability to induce a magnetic field inhomogeneity in a homogeneous magnetic field. Local susceptibility differences affect the MR imaging effect by two principles: spatial misregistration and intravoxel dephasing [134]. Spatial misregistration is caused by the spatial coding principle of MRI sequences. The non-uniform gradient fields induced by susceptibility differences disturb aligned image reconstruction [135]. Intravoxel dephasing is induced by the varying of gradient fields around the magnetic object. Spins inside a voxel are usually aligned at the TE in order to have a good echo signal (see figure 2-14). The changing of the magnetic field can dampen the echo signal. As explained above, the SE sequences can partly correct this loss because of the 180° refocusing pulse.

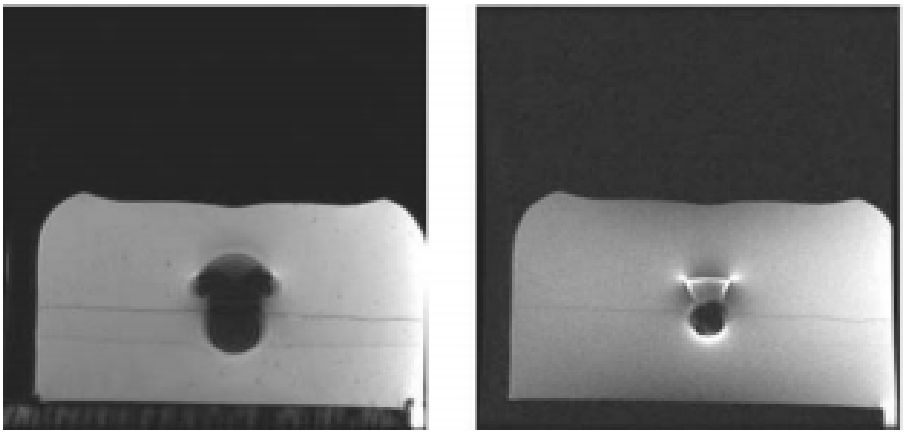

Figure 2-14: Reproduced from [134]. Typical artifacts of ferrofluid for GRE (left) and SE (right).

Superparamagnetic objects mainly affect the T2* relaxation time, and T2*/T2-weighted imaging sequences are often used to image them. In [136], the authors demonstrated that T1 can also be affected by superparamagnetic materials.

When selecting the appropriate MR sequences for assessing particle distributions in tissues, the effect of susceptibility should be small in order to have a clear identification of the blood vessels. Thus, SE sequences are better choices than GRE sequences.

2.3.5.3 Real-time MR imaging of magnetic particles through the steady-state coherent sequence

When selecting the appropriate sequence for tracking the moving particles, two basic functions are necessary and must be taken into great considerations: fast-imaging speed (rapid signal acquisition) and good imaging quality. The GRE sequences (figure 2-14) only rely on one RF pulse, resulting in a shorter TE than that of SE sequences. Moreover, if low-flip-angle excitations are applied in GRE sequences, the repetition time (TR) is also short. Another important feature of the GRE imaging is that phase shifts resulting from magnetic field inhomogeneities can induce the loss of signals. GRE sequences have been frequently used for imaging magnetic materials by using the relaxation of T2*. For the reasons above, GRE sequences are more suitable for very rapid signal acquisition and real-time tracking of superparamagnetic materials. However, it not means that the SP sequence is not suitable as the real-time MR sequence.

For example, echo planar imaging (EPI), a type of SE sequences, is a very fast imaging sequence, allowing acquisition of images in 20–100 msec [137]. As explained above, the waiting interval between SE experiments is long because longitudinal magnetization must be recovered through the T1 relaxation process after each SE sequence, resulting in the long scan time. In the EPI, after the RF excitation, multiple lines of imaging data are produced. In each TR, a train of gradient echoes is generated. One gradient echo can fill one k-space line which represents the MR image before the Fourier transform analysis. Thus, a train of gradient echoes can include many k-space lines during one TR. This technique can significantly reduce the imaging time, making real-time imaging possible. However, it is sensitive to susceptibility effects and the main magnetic field inhomogeneity [138], which limits its application in real-time tracking of superparamagnetic objects.

The True FISP (Siemens trade name, figure 2-15), a steady-state coherent sequence, is commonly accepted to be the class of GRE sequences [139]. The sequence is called FIESTA (Fast Imaging Employing Steady-state Acquisition) by GE and Balanced-FFE (Fast Field Echo) by Philips, respectively. In this sequence, balanced gradients-a coexistence of both longitudinal and

transversal magnetizations-are used, which means the dephasing induced by the net gradient over a TR interval is zero. The images are weighted by the T2/T1 ratio. This sequence has a high sensitivity to the presence of superparamagnetic nanoparticles [140, 141]. The True-FISP has been demonstrated to be capable of monitoring superparamagnetic particle positions in real time [22].

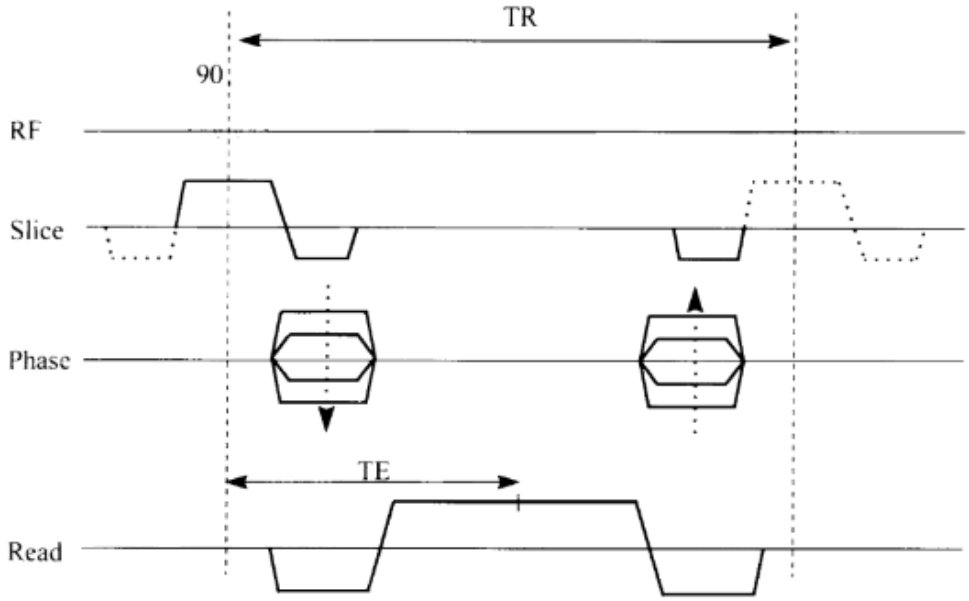

Figure 2-15: Reproduced from [142]. True FISP sequence diagrams.

2.3.5.4 Flow measurement by MRI

The necessity and possible methods of reducing blood flow during MRN have been explained. Decreased blood flow needs to be quantitatively measured through the MRI system.

In the EPI technique explained above, the gradient-echo can have a fast imaging speed. This technique is also capable of supplying a relatively high signal intensity when imaging the flowing fluid [143]. Cine MRI combines a short TR GRE sequence and cardiac synchronization with the ability to measure blood flow. The flow information is based on inflow enhancement, which makes that the obtained result is only qualitative because the signal intensity of the flowing blood varies [143].

Phase contrast MRI provides a possibility of quantitatively measuring blood flow [144]. With the presence of blood flow, a spin moving along the gradient direction will obtain a phase difference while the static spins do not have a phase difference, as shown in figure 2-16. If the magnetic

gradient is linear, the velocity of the moving spin can be calculated by measuring the amount of this phase difference [145]. However, some MRI sequences may also cause phase shifts, inducing measurement errors. Repeating the measurement with an inverted bipolar gradient solves this problem [146, 147].

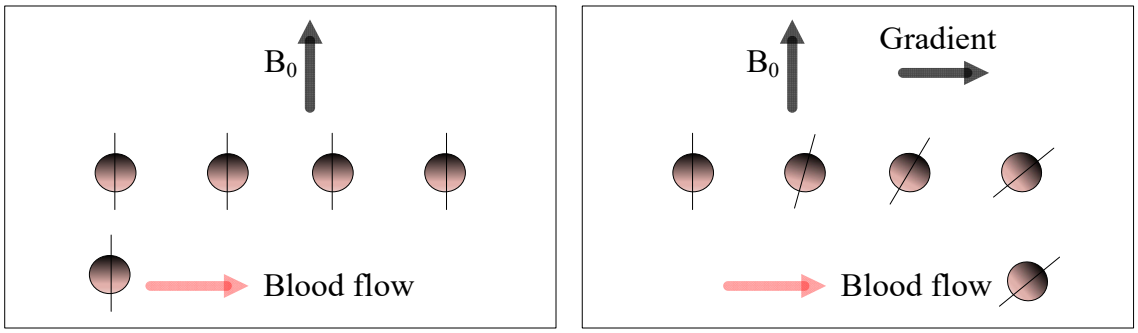

Figure 2-16: Diagrams show that a spin will acquire a phase difference when moving along the magnetic gradient.

In [148], a concept of combing the flow-dependent contrast of phase with cardiac cine imaging was proposed, resulting in a new technique: phase-contrast cine. Phase-contrast cine acquires a series of magnitude and phase images through cine and phase MRI. In the mages, the static tissue appears gray because of intermediate signal intensity, while the flowing blood appears white or black. Before the measurement, the magnitude of the velocity-encoding gradient needs to be set based on the maximal velocity of blood flow. Otherwise, aliasing artifacts may be generated if the gradient is not in an apocopate range [149].

CHAPTER 3 PROCESS FOR THE RESEARCH PROJECT AS A WHOLE AND GENERAL ORGANIZATION OF THE DOCUMENT INDICATING THE COHERENCE OF THE ARTICLES IN RELATION TO THE RESEARCH GOALS

This thesis is presented and organized in the format of a manuscript-based (article-based) thesis. Chapters 4, 5 and 6 show the main original contributions of this thesis, which includes two published and one submitted articles. In chapter 4, an article published in the 2017 International Conference on Manipulation, Automation and Robotics at Small Scales (MARSS) is shown. In this section, a method based on oscillating flow consisting of vibrating flow and constant flow used to increase the MRN capability of particles in the liquid was developed and demonstrated. In chapter 5, an article published by the journal « IEEE Transactions on Biomedical Engineering» in December 2018 is shown. In this section, an MRI-compatible particle injector was designed to precisely and repeatedly generate and inject particle boluses with the desired particle numbers and aggregate sizes, which aims to supply appropriate sized particle aggregates for MRN. In chapter 6, an article submitted to the Journal of « Annals of Biomedical Engineering» in January 2019 is shown. This section first demonstrates the feasibility of integrating the particle injection system, combination flow and MRN sequences to achieve two-level bifurcation MRN, which consists of forming size-controllable microparticle aggregates, tracking their movements and steering them into a selected end-branch of a two-level bifurcation phantom.

In section 1.1 of chapter 1, I explained a number of existed MRN problems, followed by a list of my research objectives in section 1.2. The objectives can be simply summarised as (1) finding and demonstrating a flow pattern to increase MRN success rates in a liquid, (2) design of an MRI-compatible injection system, and (3) integration of all MRN parts to achieve successful MRN in multi-bifurcation phantoms.

Chapter 3 of this thesis addresses objective 1 through the experimental study of MRN performances in two types of flow patterns: constant and oscillating flow. This chapter presents a new concept, the synergy of an oscillating flow consisting of a vibrating flow and a constant flow which is capable of increasing the MRN success rate even if the magnetic gradient is no more than 40 mT/m. Indeed, since the blood flow in hepatic arteries can reach tens of centimeters per second

while the magnetic gradient of clinical MRI is no more than 40 mT/m, how to increase the manipulation capability of particles in a liquid is an important research topic. Before this work, I had demonstrated the possibility of controlling blood flow in hepatic arteries through *in vivo* experiments (Appendix B). After fabricating 200 μm particles (Appendix A), the performance of particle MRN was evaluated in a low-velocity constant flow. The results revealed that a constant flow makes it difficult to ensure a high MRN success rate. At last, I experimentally demonstrated that the combination of a vibrating flow and a constant flow can increase the success rate of MR navigation for particles in a liquid through the targeted bifurcation.

Chapter 4 addresses objective 2 through the design of an MRI-compatible injection system capable of forming the size specific particle aggregates. Infrared photoresist devices were tested to count the microparticle number in the high magnetic field induced by the clinical MRI. In the design of the setup, the injector was divided into two parts: the controller, which controls the capture and release of magnetic particles, and the MRI-compatible actuator, which sends out a measured signal for monitoring the particle number while acting as a mechanical actuator for particle aggregation and release. The light reaching the receiver diminishes as the opaque magnetic particles accumulate in the counting chamber. By monitoring the resistance of an infrared receiver, the size of an aggregate could be obtained.

Chapter 5 addresses objective 3 through a computational model and experimental studies. The model, based on the force balance of MDEBs after a magnetic force has been applied to them, describes the appropriate size of particle aggregate for successful MRN. The used parameters include the vessel size, the density and magnetization of particles, the magnetic steering gradients, the buoyancy, the gravity, and the vessel direction relative to B_0. In this section, oscillating flow and the proposed injection system will work together to achieve MRN. Particle aggregates formed with an appropriate size would be injected into phantom inside the MRI bore. I used a trigger signal to start the MRN sequence when aggregates were released from the catheter. Then, a simple MRN sequence was proposed. The duty cycle of the steering gradient and True FISP sequences were arranged based on the kinetic characteristics of the particles and the measured imaging parameters. At last, the experimental results demonstrated the feasibility of integrating all MRN parts in order to achieve successful MRN in a multi-bifurcation phantom. This research is the first successful attempt of integrating a particle injection system with MRN sequences to achieve two-level bifurcation MRN.

CHAPTER 4 ARTICLE 1: COMBINING OSCILLATING FLOW AND CLINICAL MRI GRADIENTS FOR TARGETED THERAPY

Ning Li; Charles Tremblay; Sylvain Martel

Laboratory of NanoRobotics, Department of Computer Engineering, Institute of Biomedical Engineering, Polytechnique Montreal, Montreal, QC, Canada.

Published in *2017 International Conference on Manipulation, Automation and Robotics at Small Scales (MARSS)*, on 08 August 2017. (DOI: 10.1109/MARSS.2017.8001937)

4.1 Abstract

Abstract—In this paper, a method based on an oscillating flow consisting of an 8 Hz vibrating flow and a constant flow used to increase the manipulation capability of particles in a liquid is developed and demonstrated. The method was integrated with magnetic resonance navigation (MRN) for targeted manipulation. Micro particles encapsulating superparamagnetic nanoparticles were successfully navigated in a Y-shaped channel using the proposed drifting method and MRN using a magnetic gradient of 40 mT/m. The strategies and results presented in this paper envision a method for targeted drug delivery at the human scale.

Key words—Medical interventions, oscillating flow, magnetic resonance navigation, magnetic micro particles, targeted drug delivery.

4.2 Introduction

Hepatocellular carcinoma (HCC) is the most common type of liver cancer. It is recognized as the second cause of cancer deaths worldwide [150]. Today, Trans Arterial Chemo Embolisation (TACE) therapies are commonly preferred therapeutic approaches. In TACE, a catheter is inserted into the vessels leading to the tumor, followed by the injection of embolizing agents. These agents drifted with the blood flow prior to block the flow feeding the tumor. Due to the size of the catheter, the extremity of the catheter is usually advanced deep inside an artery while remaining relatively far from the target site. Therefore, without targeted navigation, many particles may enter the healthy area and block it. Although micro-catheter can reach smaller arteries, it depends much on the capability of the physician, and repeated catheterizations may be needed. A new approach

known as magnetic resonance navigation (MRN) is used to navigate ferromagnetic objects deep inside the blood vessels [9, 115]. The technique uses a clinical magnetic resonance imaging (MRI) system to track and steer therapeutic magnetic micro carriers (TMMCs). Generally, a TMMC is made of biodegradable material, antitumor drugs and magnetic nanoparticles [17, 19, 22, 105]. The nanoparticles are magnetized to saturation by the main magnetic field of the MRI scanner, but do not retain net magnetization once removed from the field. Therefore, the imaging gradient coils provide a means of directional propulsion force to the particles when they are magnetized, which helps them reach appropriate releasing sites. At last, the nanoparticles are released from the biodegradable materials, and are cleaned by the phagocytic function of the body. Our group has previously proven the feasibility of this technique in a rabbit model [17, 105]. However, some technical challenges arise when we propose to apply the technique to human size.

For magnetic gradients, the magnetic force on a particle is computed as

$$\boldsymbol{F_m} = V_p(\boldsymbol{M} \cdot \nabla)\boldsymbol{B} \qquad \text{(Eq. 4-1)}$$

where $\boldsymbol{F_m}$ is the magnetic force, V_p is the total effective volume of particles (m3), $\boldsymbol{M}$ is the magnetization level (A/m), and $\nabla \boldsymbol{B}$ is the spatial variation or gradient of the magnetic field (T/m). When the particle is moving in a liquid, the gradient force with the drag force result in a magnetically induced velocity [95]

$$\boldsymbol{U_m} = \boldsymbol{F_m}(6\pi r\mu)^{-1} \qquad \text{(Eq. 4-2)}$$

where r is the particle radius, μ represents the dynamic viscosity of the fluid, and $\boldsymbol{U_m}$ is the particle velocity induced by magnetic forces.

If the particles in a vessel can travel a distance equal to the diameter of the vessel before entering the next intersection, they can be navigated into a selected branch.

$$\frac{D_{vessel}}{\boldsymbol{U_m}} = \frac{L_{vessel}}{\boldsymbol{U_f}} \qquad \text{(Eq. 4-3)}$$

where L_{vessel} is the vessel length before the next intersection, D_{vessel} is the internal diameter of the vessel, and U_f is the particle velocity induced by the flow. To improve the targeting efficiency, the radio U_m/U_f needs to be increased. The parameters that can increase the ratio are:

1) Magnetic gradient strength. In previous research, an upgraded gradient system has been used to provide an ultrahigh magnetic gradient strength (400 mT/m)—about ten times higher than that of

the clinical MRI [151]. Such a system has a reduced diameter, which prevents it from being used for the whole body. Generally, the magnetic gradients of the regular MRI can only generate 40 mT/m gradients. Moreover, the gradient strength is limited not only by technology related issues but also by physiological constraints. For instance, in the case of the slew rate dB/dt, the FDA guidelines suggest 0-20 T/s [152]. As such, if we use a maximum adequate rise time of 200 μs for MR-image sequencing, the maximum gradients will be 40 mT/m. Therefore, in this paper, the gradients are always set to 40 mT/m.

2) Particle properties. Increasing the size and magnetization of particles are two possible methods to increase the ratio. For the diameter of particles, 100-300 μm is recommended [110, 153]. Larger particles cannot be steered into the small arteries while particles with a diameter below 30 μm can entail the risk of extravasation and lung embolization [105]. This requires that the size of particles needs to be in the recommended range. For the particle magnetization, increasing the concentration of magnetic nanoparticles yields a higher volume magnetization. However, this increases the injected dose of nanoparticles into the body, and may also affect the loading amount of the antitumor drugs.

3) Particle velocity induced by the flow, which is the main interest of this paper. We investigated the control of the flow in this paper. The purpose was to ensure that particles in a low-speed flow could be precisely manipulated during MRN, when the magnetic gradients were set to 40 mT/m. This paper is organized as follows: at first, the TMMCs were synthesized using the flow-focusing technique [154]. Then the oscillating flow was investigated as the drifting method for the particles. Finally, we demonstrated that the combination of oscillating flow and MRN could successfully navigate the particles into the targeted branch of a Y-shaped channel.

4.3 Methodology

4.3.1 Particles

The flow-focusing technique was applied to fabricate the MMCs, i.e. TMMCs without therapeutics [154]. Alginate solution (1.5%) (Sigma-Alrich, St. Louis, MO) was used to encapsulate water-based ferrofluid (fluidMAG-D, Chemicell GmbH, Germany). The ferrofluid contains 200 nm superparamagnetic particles whose concentration is 25 mg/ml. Magnetic moments of the fluid were measured using the vibrating sample magnetizer (EV9, microsence), and it was

known that the saturation magnetization reaches 1.36 emu/g through the hysteresis curve. Then, 0.5 ml alginate and 0.1 ml ferrofluid were mixed together, and were spayed into calcium solution (1%) (Sigma-Alrich, St. Louis, MO) by the flow-focusing device. Based on the optical images (ZEISS AxioImager microscope), the resulting MMCs have an average diameter of ~200 µm, as shown in figure 4-1.

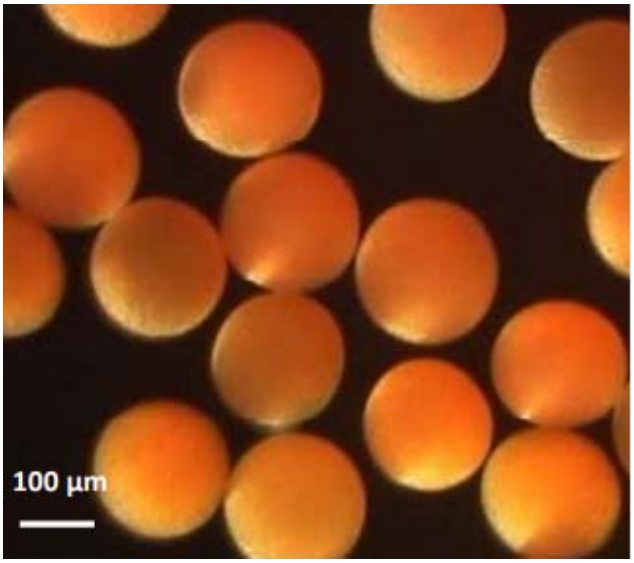

Figure 4-1: Photo of the magnetic micro beads.

4.3.2 Experimental setup and oscillating flow

A polymethylmethacrylate (PMMA) based phantom was manufactured by micro-milling (LPKF Protomat 95s/II) and thermal sealing techniques. The phantom has a Y-shaped channel. The main channel has a depth of 0.9 mm and a width of 1.5 mm, and the two following branches have a width of 1.2 mm and a depth of 0.9 mm. The main channel was parallel to B_0 (Z-direction) of the MRI magnetic field. A 5F catheter used for particle injection was inserted into the main channel, and the position of catheter tip could be turned manually. The phantom was placed at the center of a 1.5 T Siemens Sonata MRI (Siemens, Erlangen, Germany). A 3D set of gradient coils was used to generate the magnetic gradients. An MRI compatible camera (MRC Systems GmbH, Heidelberg, Germany) located above the phantom was used to record the movement of the MMCs.

We describe the oscillating flow by its amplitude, frequency, and mean flow rate (constant flow) [155], as shown in Fig. 4-2(b). When the constant flow is 0, the oscillating flow is defined as vibrating flow. Therefore, the oscillating flow can be defined as the combination of constant flow

and vibrating flow in this paper. We used a medical pump (Baxter 6301, USA) and an electro-magnetic coil actuation vibrator to provide these two flows. Prior to the experiment, DI water was injected into the tube, and bubbles were carefully evacuated because the gas is easy to be compressed and could cause a significant absorption of vibration. Then the saline water (0.9 wt %) was injected at room temperature.

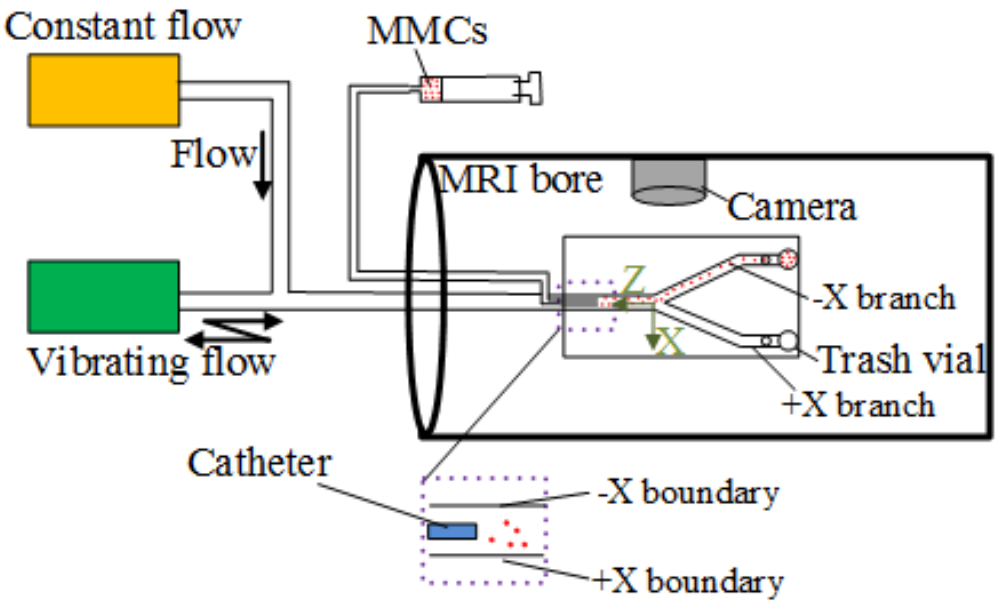

(a)

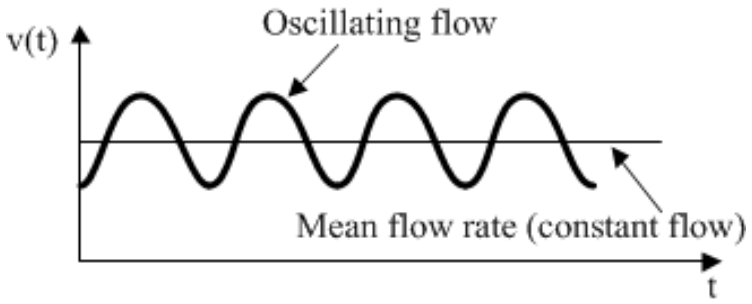

(b)

Figure 4-2: Experimental setup. (b) The pattern of an oscillating flow.

4.3.3 Phenomena and principle

In the first experimental section, we researched the manipulation characteristics of particles in different fluid patterns, which include the drifted movement by flow and the navigation velocity by magnetic gradients. Magnetic particles have a strong tendency to agglomerate in the presence

of the high strength uniform B_0 field. In our experiments, the aggregates were usually made of groups of 2-5 particles. The initial flow was constant at a speed of 0.97 ml/min. This yielded a flow velocity of 1.2 cm/s in the main channel. Figure 4-3 shows the process of drifting four aggregates before two branches. From the snapshots a1-a3, it is easily observed that aggregate 1 moved into the -X branch with a mean velocity of 2 mm/s, while aggregate 2, 3 and 4 were stationary. The phenomena above were caused by the non-uniform distribution of various forces on the particles, such as gravity, Van der Waals force and electrostatic force [156]. Moreover, the non-uniform flow distribution in the channel further promoted the different behaviors of drifted particles. Then magnetic gradients of 40 mT/m were applied in the X direction. We found that 1) the moving aggregates did not have sufficient time to be navigated into the selected channel branch, and 2) the stationary aggregates kept stationary and had no response to the magnetic steering force. The first phenomenon could be explained by the low velocity ratio U_m/U_f; the second was induced by the small steering force which was not significant enough to move the stationary particles.

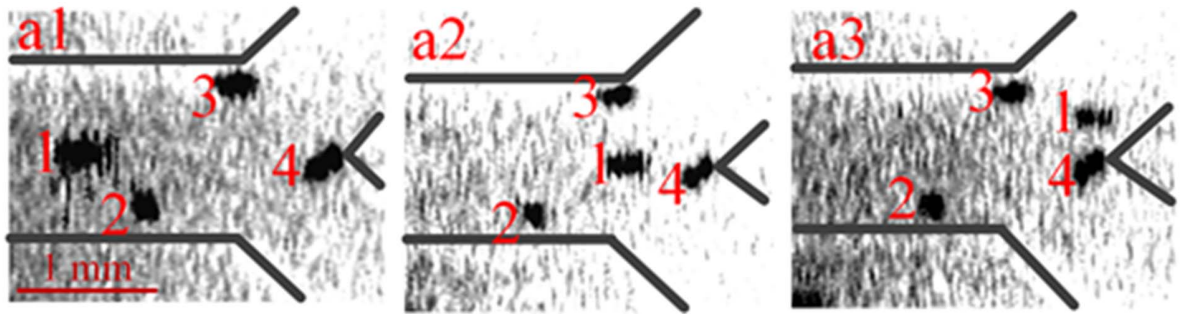

Figure 4-3: Movement of MMC aggregates drifted by a constant flow with a known velocity of 1.2 cm/s.

After this, a vibrating flow generated from a magnetic vibrator was applied. The amplitude of the vibrating flow was tuned for easy observation of particle vibrations. The aggregates were vibrating at an amplitude of 200 μm (peak-peak) around their own equilibrium positions, and the vibration was always parallel to the direction of the channel. The operating frequency of the vibrator was set to 8 Hz. Then the constant flow was re-initiated, and a 1 mm/s flow was injected into the main channel. It was observed that all aggregates started to move at a stable velocity of 260 μm/s while maintaining their vibrating state. When the constant flow was switched off, the aggregates stopped immediately, and they also instantly restarted moving when the constant flow

restarted. We also demonstrated that the magnetic gradients could induce a stable velocity to the vibrating aggregates. The value was about 50 μm/s when the gradients were 40 mT/m.

In summary, when a particle is stationary, many forces, such as dipolar interactions can induce attractive forces between particles and tunnel surface, which can prevent particles from moving even when submitted to a constant flow. However, the attractive forces may be overcome by the shear force from the vibrating flow. The flow can also maintain a vibrating status over particles around their own equilibrium positions. After the constant flow or the magnetic force is applied on the vibrating particles, a small displacement vector is generated along the direction of the inducing force. This explains why the oscillating flow can make the manipulation of particles easier in fluid.

4.4 Results

To investigate the navigation characteristics of the MMC using the oscillating flow and magnetic steering force, a 1mm/s constant flow and an 8 Hz vibrating flow were applied again. Before the steering experiments, an aggregate had been moved close to the -X boundary of the channel using strong magnetic gradients (400 mT/m). The aggregate was initially 4 mm in front of the channel intersection. The MMC amplitude was 200 μm (peak-peak), and the magnetic gradient in the +X direction was 40 mT/m. The aggregate moved at a velocity of 260 μm/s in the -Z direction, and generally went along the +X direction at a steering velocity of 50 μm/s. As shown in figure 4-4, the aggregate was finally navigated into the +X branch of the phantom. In comparison, without magnetic steering force, the aggregates would be moved along the -X boundary, and enter the -X branch at the end.

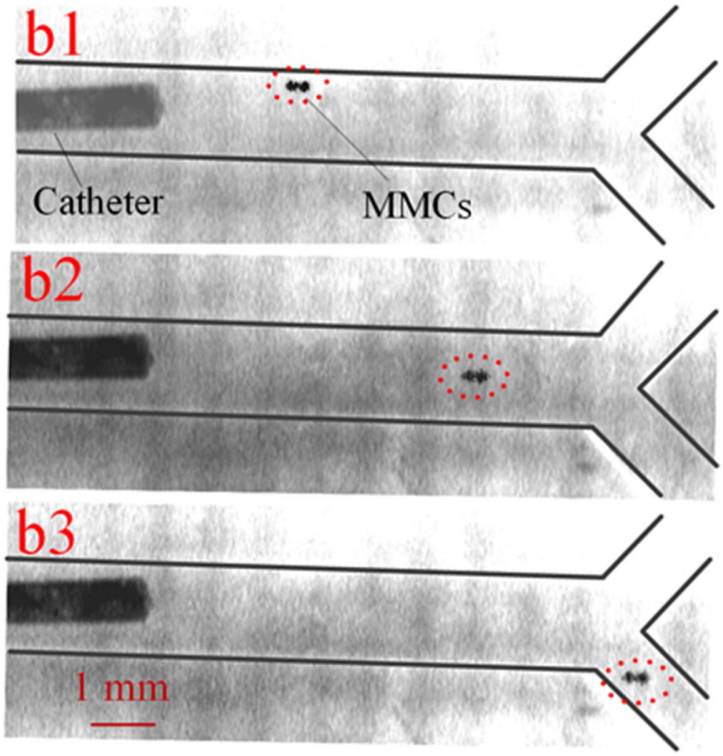

Figure 4-4: Sequence of images to show different positions of the MMC aggregates during the navigation using the oscillating flow and magnetic steering force.

We further measured the drifted velocities of particles when a constant flow velocity was set to 1, 1.5, 2, 2.5 and 3 mm/s. Throughout the measurement process, the diameter of the particles was kept at 200 μm. Based on the measured results, the effect of the flow rate on the deflection of MMCs is presented in figure 4-5. The critical displacement is defined as the minimum navigation displacement which ensures that all particles are navigated into the selected branch from the main channel, and the value is 0.75 mm, i.e. half of the width of the main channel. It indicates that a MMC that is 4 mm away from the channel intersection might enter the unselected branch if the flow velocity is more than 1 mm/s, which has been demonstrated by our experiments.

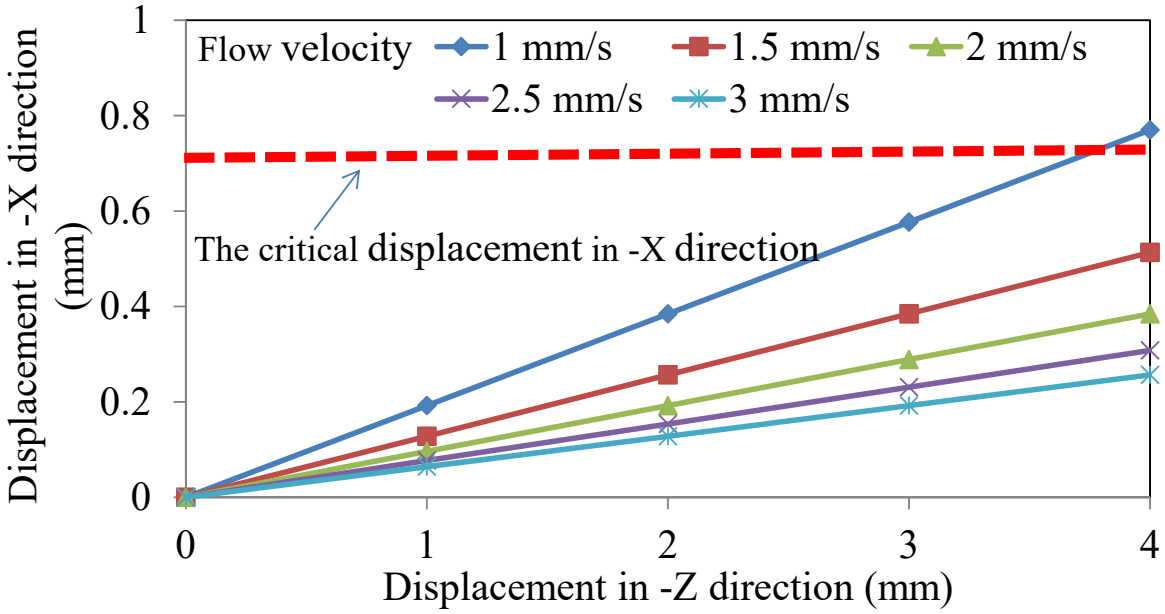

Figure 4-5: The calculated deflection pattern of microparticles during the navigation.

4.5 Discussion

In our experiments, the combination of oscillating flow and MRN made the targeted navigation of micro carriers possible. The flow could maintain a vibrating state for micro particles, and the particles were easy to be manipulated by low-velocity flows or small magnetic steering forces. In the in-vivo applications, the vibration will become weak along the vessels because of the absorption from the vessels wall. Therefore, the characteristics about vibration loss should be further researched in future work. Moreover, a magnetic vibrator is used to supply vibrating flows; as the distance between the vibrator and the MRI should be more than 5 meters for safety, the long tube is another factor for vibration loss. The MRI-compatible actuator is a preferred choice when the operation is in MRI.

Several parameters used in our experiments should be comprehensively considered before the in vivo experiments. The frequency selection should be guided based on physiological and physical conditions. We only tried a frequency of 8 Hz in this paper. However, the 5-50 Hz flows have been experimentally tested to research the changes of vascular resistance in animal vessels [155, 157].

In our experiments, the video camera for visual imaging and tracking is suitable in the in vitro research. The proposed strategy cannot be independently used in drifting of micro particles in the

body, but should be combined with other medical devices, such as ultrasonic imagining machine, MRI, or X-ray devices, to achieve the particle imaging

4.6 Conclusion

In conclusion, we experimentally demonstrated that the combination of vibrating and constant flows could increase the manipulation capability of particles in a liquid. Then, the method was integrated with MRN for targeted manipulation. MMCs encapsulating superparamagnetic nanoparticles were successfully navigated into the desired branch of a Y-shaped phantom even if the magnetic gradients were 40 mT/m. The method proposed in our paper is not limited to MRN, and it may also work with other medical intervention methods, such as electric fields, ultrasound, and hyperthermia, to name but a few examples.

ACKNOWLEDGEMENT

This study was funded by the Canada Research Chairs and an Operating Grant: Collaborative Health Research Projects (NSERC Partnered).

CHAPTER 5 ARTICLE 2: MRI-COMPATIBLE INJECTION SYSTEM FOR MAGNETIC MICROPARTICLE EMBOLIZATION

Ning Li [1], Francois Michaud [2], Zeynab Nosrati [3], Dumitru Loghin [1], Charles Tremblay [1], Rosalie Plantefève [1,4], Katayoun Saatchi [3], Urs O. Häfeli [3], Sylvain Martel [1], and Gilles Soulez [2,5]

[1] Laboratory of NanoRobotics, Department of Computer Engineering, Institute of Biomedical Engineering, Polytechnique Montreal, Montreal, QC, Canada.

[2] Laboratoire clinique du traitement de l'image, Centre de recherche du Centre Hospitalier de l'Université de Montréal (CRCHUM), Montréal, Québec, Canada.

[3] Faculty of Pharmaceutical Sciences, University of British Columbia, Vancouver, BC, Canada.

[4] Medical Laboratory, Department of Computer and Software Engineering, Institute of Biomedical Engineering, Polytechnique Montréal, Montréal, QC, Canada.

[5] Department of Radiology, Radiation Oncology and Nuclear Medicine, University of Montréal, Montreal, QC, Canada.

Published in *IEEE Transactions on Biomedical Engineering,* on 20 December 2018. (DOI: 10.1109/TBME.2018.2889000)

5.1 Abstract

Objective: Dipole field navigation (DFN) and magnetic resonance navigation (MRN) exploit B_0 magnetic fields and imaging gradients for targeted intra-arterial therapies by using magnetic drug-eluting beads (MDEBs). The strong magnetic strength (1.5 or 3 T) of clinical magnetic resonance imaging (MRI) scanners is the main challenge preventing the formation and controlled injection of specific-sized particle aggregates. Here, an MRI-compatible injector is proposed to solve the above problem. *Methods:* The injector consists of two peristaltic pumps, an optical counter, and a magnetic trap. The magnetic property of microparticles, the magnetic compatibility of different parts within the injector, and the field distribution of the MRI system were studied to determine the

optimal design and setup of the injector. The performance was investigated through 30.4 emu/g biocompatible magnetic microparticles (230 ± 35 μm in diameter) corresponding to the specifications needed for trans-arterial chemoembolization (TACE) in human adults. *Results:* The system can form aggregates containing 20 to 60 microparticles with a precision of 6 particles. The corresponding aggregate lengths range from 1.6 to 3.2 mm. Based on the injections of 50 MRI-visible boluses into a phantom which mimics realistic physiological conditions, 82% of the aggregates successfully reached subbranches. *Conclusion and Significance:* This system has the capability to operate within the strong magnetic field of a clinical 3T MRI, to form proper particle aggregates and to automatically inject these aggregates into the MRI bore. Moreover, the versatility of the proposed injector renders it suitable for selective injections of MDEBs during MR-guided embolization procedures.

Key words—MRI-compatible particle injection system, magnetic resonance navigation, hepatocellular carcinoma intra-arterial therapies, magnetic nanoparticles, drug-eluting beads.

5.2 Introduction

HEPATOCELLULAR Carcinoma (HCC) is a common type of cancer with a high fatality rate worldwide [158]. For non-resectable HCC, trans-arterial chemoembolization (TACE), a palliative and minimally invasive cancer therapy, is the preferred treatment [159]. The TACE technique consists of the injection of chemotherapeutic agents through a catheter inserted into the vascular system, followed by the injection of embolizing agents to block the tumor perfusion. The high selectivity of the method is owed to the physician's ability to insert a microcatheter into selected vessel branches [45, 46]. However, the principal drawbacks of this method are the need to perform catheterization repeatedly and the risks of exposure to ionizing X-ray radiation which, even if not significant for a patient with advanced liver cancer, can be harmful to the staff and the interventional radiologist performing the procedure. Besides, possible non-target embolization which results in damages to normal tissues is a significant concern. Intra-arterial chemotherapy with an implantable arterial port has been proposed as a means to avoid repeated catheterization procedures [160]. However, this technique does not allow simultaneous chemotherapy and embolization which are both required to maximize the local effect of chemotherapy since the whole liver would otherwise be affected. MRI-based interventions are promising techniques that aim to navigate Magnetic Drug-Eluting Beads (MDEBs) into a targeted site [9, 93, 161-163]. In this

technique, superparamagnetic nanoparticles are embedded into Drug-Eluting Beads to induce the sufficient magnetic force from an external magnetic source, allowing the anti-tumor drugs to be steered and delivered to tumor sites [105, 164]. The superparamagnetic property of the nanoparticles is clinically important since it allows them to be magnetized when exposed to a magnetic field while not retaining any net magnetization once removed from the field. MDEBs can, therefore, be navigated in aggregates due to magnetic dipole-dipole interactions when exposed to a magnetic field and disaggregate into individual particles after the patient is removed from the MRI. The sizes of the embedded nanoparticles typically range from 5 to 20 nm in order to exhibit superparamagnetic properties while being safely phagocytosed in the body [165].

Two different approaches have been reported to successfully navigate MDEBs in an MRI bore: Dipole Field Navigation (DFN) and Magnetic Resonance Navigation (MRN) [9, 89, 166-168]. In DFN, the uniform magnetic field of a clinical MRI scanner is distorted by using soft ferromagnetic cores placed at strategic locations [169]. With this method, the gradients are static and spatially distributed, allowing a continuous injection of particles. However, with this technique, imaging cannot be performed during injections because of the distorted magnetic field [90]. This makes the computation of the delivered dose in each liver section difficult: continuous injections will have to be halted and the source of distortion removed to allow imaging sequences to be launched. An injector that has the ability of delivering a precise amount of particles could drastically simplify the procedure. Indeed, once the desired number of particles is reached in a specific liver segment, only small adjustments of the ferromagnetic cores are required to target another part of the liver. On the other hand, MRN allows fast and easy alternations between steering and imaging sequences, thus enabling targeted efficiency assessments. Although in vivo applications of MRN were successful, MDEBs were navigated through a single bifurcation. Hence, the continuous injection was possible [17]. For MRN across several arterial bifurcations, the MDEBs would be steered in the target vessel by switching the direction of the gradient, depending on the position of particles and the orientation of the vessel bifurcations [170]. The gradients in MRN act on all particles. Thus, the next aggregate injection cannot be triggered until the previous bolus reaches the target. This is defined as a pulsed-bolus injection. Therefore, an injector capable of controlling pulsed-bolus injections would be essential to perform multi-bifurcation navigation.

Besides magnetic navigation of particles, advancements in MR-guided catheter navigation techniques could eventually make it compatible with selective embolization of liver tumors [82,

171]. Again, an MRI-compatible injector could be useful to inject a precise dose of MDEB in different feeders supplying a tumor.

Regarding MRN, the magnetic steering force in Newton on a particle is computed as

$$\boldsymbol{F_m} = V_p(\boldsymbol{M} \cdot \nabla)\boldsymbol{B} \quad \text{(Eq. 5-1)}$$

where V_p is the volume of magnetic material (m^3), $\boldsymbol{M}$ is the volume magnetization of the particles (A/m), $\boldsymbol{B}$ is the magnetic flux density, and $\boldsymbol{\nabla B}$ is the magnetic gradient (T/m).

When a particle navigates in a fluid, the magnetic force must be balanced with drag forces because of the magnetically induced velocity $\boldsymbol{U_m}$ (m/s) [95]

$$\boldsymbol{U_m} = \boldsymbol{F_m}(6\pi r\mu)^{-1} \quad \text{(Eq. 5-2)}$$

where r is the radius of the particle, and μ is the dynamic viscosity of the fluid.

From Eq. 5-1 and Eq. 5-2, we can conclude that the magnetic force increases at a cubic rate with the particle radius, while the resulting velocity in a viscous flow increases quadratically with the radius. This suggests that larger microparticles or aggregates can be navigated more efficiently. However, the size of aggregates needs to fall within the limits of the inner diameter of approved catheters and the blood vessels they transit into. Therefore, a control of the number of particles per aggregate is crucial.

To our knowledge, no MRI-compatible injector that has the function of accurately controlling the amount of magnetic microparticles per injection has been reported. Although a catheter-based injector has been previously proposed to inject particle boluses into an MRI [116], the injector simply uses serial coils to capture and release magnetic particles. Thus, this injector did not allow the obtainment of a real-time particle count or a control over the aggregates' size, which are crucial for successful navigation and patient safety.

This study aims to investigate the design of an MRI-compatible particle injection system to precisely and repeatedly generate and inject particle boluses with the desired particle numbers and aggregate sizes. Here, we hypothesize that our injection system: 1) is compatible with a strong magnetic field (3 T), 2) is capable of controlling the aggregate size, as well as the particle number in each aggregate and 3) allows for the injection of intact aggregates into the MRI bore through a catheter.

5.3 Method

Before designing the injector, the optimal size of aggregates in the context of MRN is determined based on vessel dimensions. Here, we choose the vessels that are used in the HCC interventions as reference. The common, right and left hepatic arteries have respectively internal diameters (mean ± standard deviation) of 4.5 ± 0.3, 3.0 ± 0.3, and 3.6 ± 0.4 mm [172]. Consequently, the maximum length of the particle aggregate perpendicular to the target branch direction should be about 3 mm in order to be navigated into the left or right branch division of the hepatic artery. Therefore, in this paper, the targeted aggregate sizes were set to about 3 mm. Moreover, considering the fact that 5 French catheters are often used to catheterize the main hepatic artery during routine chemoembolization [45, 46, 116], the aggregate should also be able to pass through the catheters.

5.3.1 Injector design

As shown in figure 5-1, the injector is composed of two main functional parts: the controller, which controls the capture and release of magnetic particles, and the MRI-compatible actuator, which sends out the measured signal for monitoring the particle number while acting as a mechanical actuator for particle aggregation and release. Unlike the previous injector which uses serial coils to capture and release magnetic particles, our injector added a counting chamber and the corresponding circuit to calculate the particle numbers and aggregate sizes.

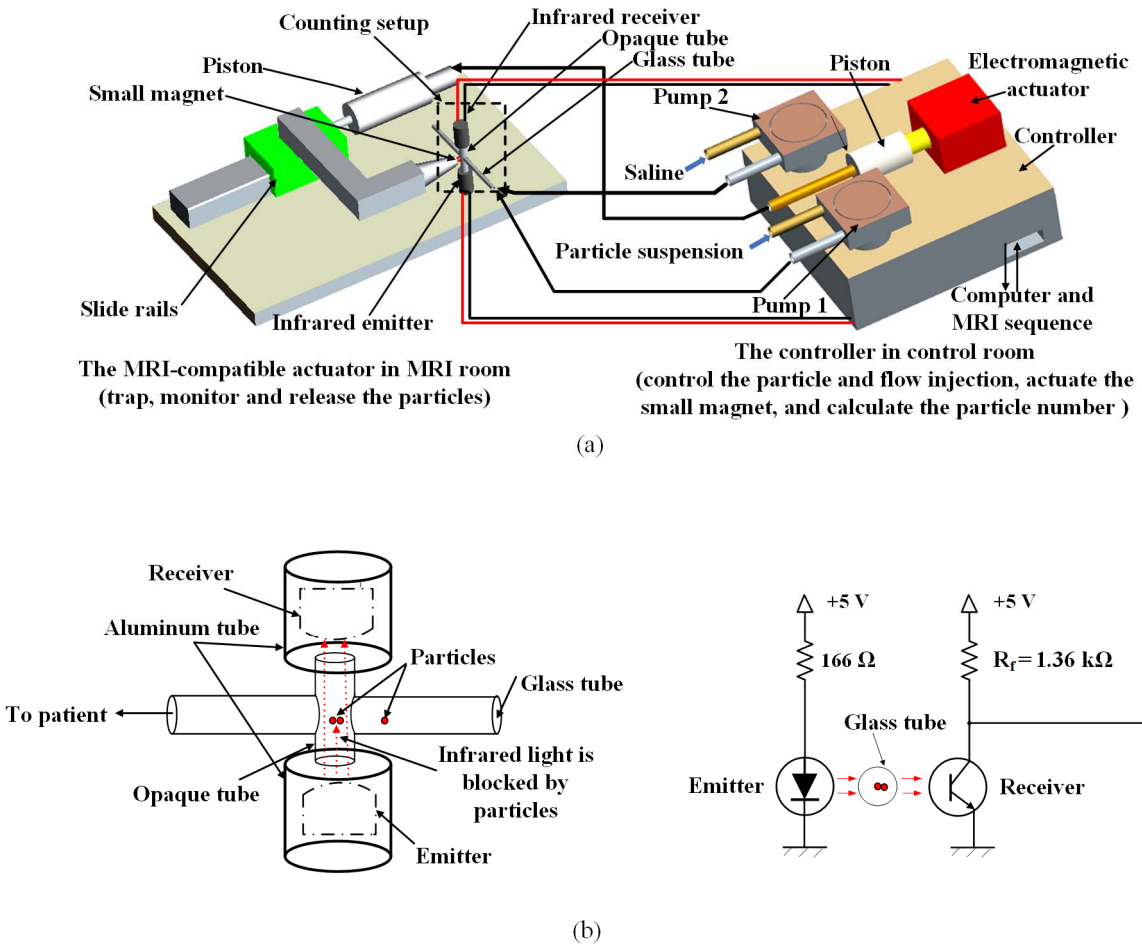

Figure 5-1: Experimental setup used for particle injections. (a) Schematic diagram of the injector. (b) The counting chamber (left) and the corresponding circuit diagram (right).

In terms of hardware setup, the injector consists of two microcontroller boards, two peristaltic pumps and an electromagnetic actuator. The microcontroller boards use an Arduino Uno and an ARD-MD Arduino Motor driver shield. Two peristaltic pumps, Pump 1 and Pump 2, are used to transport the particle suspension and saline (0.9% NaCl in distilled water), respectively. The electromagnetic actuator is an electromagnet-based piston, which generates a hydraulic driving force to another piston holding a small cylindrical neodymium magnet (1/16" diameter × 1/16" thickness, K&J Magnetics, Inc., USA). In its resting position, the magnet holds particles in the counting chamber by means of magnetic force, while more are incoming. An aggregate is released when the electromagnetic actuator activates and pulls the small magnet away from the counting chamber.

To estimate the total number of particles in the counting chamber, an infrared (IR) emitter (LTE-3371T, Lite-On Inc., Taiwan) and a receiver (LTE-3208, Lite-On Inc., Taiwan) are used. These two electronic devices were selected randomly from our toolbox. When putting them in the high magnetic field inside the MRI bore, they were both satisfied requirements for particle detection.

To increase the measurement sensitivity and to decrease the noise signal from the natural light, the IR emitter and receiver are encapsulated into two aluminum tubes, and the tubes are linked by an opaque plastic tube. A transparent glass tube has been vertically inserted into a hole in the middle of the plastic tube, as shown in figure 5-1(b), such that the infrared light from the emitter could pass through the lumen of the plastic tube to be detected by the receiver. We chose a glass tube with an internal diameter of 0.9 mm to match the inner lumen of 5 French catheters. The tubing between pumps and actuator also has a diameter of 0.9 mm. This ensures a consistent diameter from the pumps to the patient, decreasing the possibility of aggregates clogging up. The light reaching the receiver diminishes as the opaque magnetic particles accumulate in the counting chamber, resulting in a higher ohmic resistance detected by the circuitry since fewer photons are now reaching the IR receiver. The tube is considered to be the bolus generator channel. A simple circuit is used to measure the resistance R which is given by

$$R = \frac{(\mathrm{U}-\mathrm{V}_f)R_f}{\mathrm{V}_f} \quad \text{(Eq. 5-3)}$$

where R_f is a serial resistance, V_f is the measured voltage from the Arduino, and U is the total voltage of the serial circuit. In our experimental setting, R_f is 1.36 kΩ and U is 5 V. These values are used to calculate the resistance using Eq. 5-3.

This circuit was tested in a 1.5 T (Sonata, Siemens, Erlangen, Germany) and a 3 T MRI scanner (Skyra, Siemens, Erlangen, Germany). No change of recorded resistivity from the receiver was observed.

The complete injection workflow protocol is outlined in figure 5-2. The injector works as a subsystem in MRN, which consists of an MRN sequence, a flow control system and the injector described here. The MRN sequence determines the imaging, tracking, navigation and particles injection steps required for targeted therapies. When a bolus needs to be injected, a trigger signal #1 is sent by the MRN sequence. After the signal is received by our injector, Pump 1 pushes the particles into the counting chamber. These particles are captured in the area because of the presence of a strong pulling force induced by the small magnet. Meanwhile, the controller continuously

monitors the R in Eq. 5−3 to determine whether the number of particles has reached the desired value. Then, Pump 1 shuts down to prevent more particles from entering the counting chamber. Simultaneously, the electromagnetic actuator engages to release the aggregate and Pump 2 is activated to push the aggregate into the arterial catheter located inside the MRI scanner. When the aggregate reaches the tip of the catheter, the trigger signal #2 from the MRN sequence is sent to the injector, thus switching off the electromagnetic actuator and Pump 2. Then, the injector maintains its initial status until the next trigger signal #1 is received.

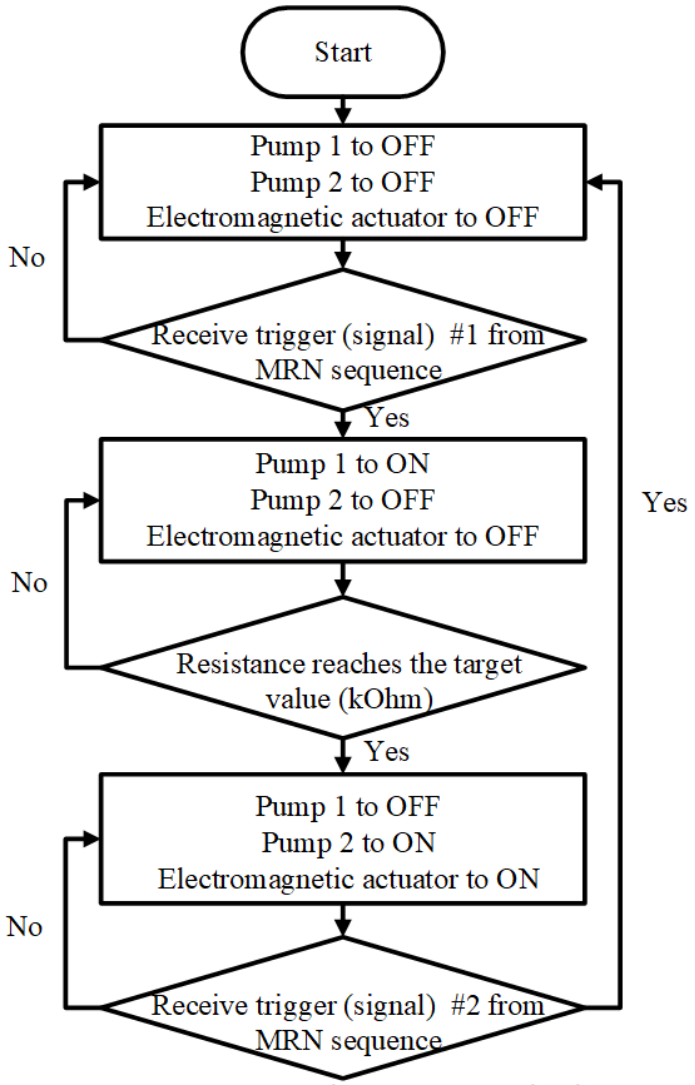

Figure 5-2: Workflow of the injector and possible interface with MRI for MRN. This workflow could be adapted for DFN or selective embolization using MR-guidance.

5.3.2 Particle design

The preferred size of microparticles (superparamagnetic nanoparticles with therapeutics embedded in a polymer matrix) for human liver chemoembolization is about 100–300 μm, which is based on the diameter of the arterioles used for embolization [173].

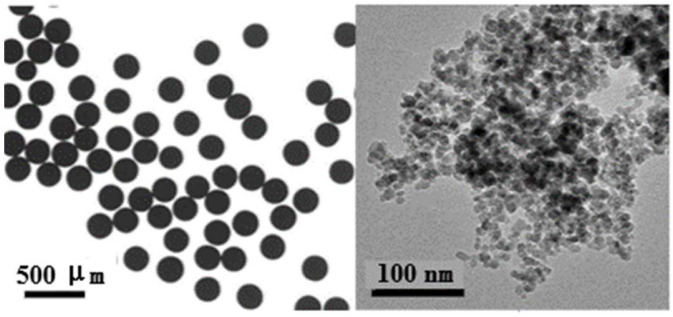

(a)

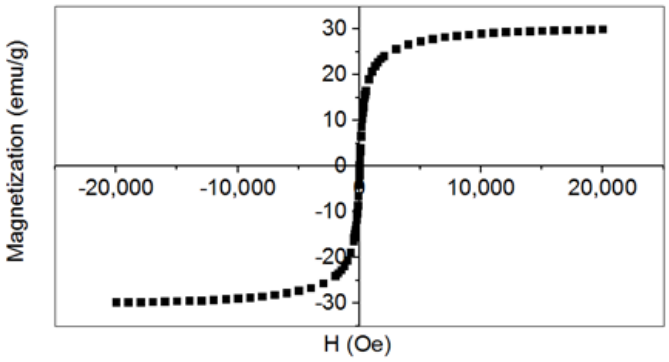

(b)

Figure 5-3: Design and magnetic characteristics of magnetic particles. (a) Monodisperse magnetic microparticles shown in the microscope (left) are made from 60 wt.% magnetite nanoparticles (right) and 40 wt.% biodegradable polymer PLGA. (b) Magnetization curve of the microparticles.

Microparticles composed of 40% poly (lactic-co-glycolic) acid (PLGA) (Durect Corporation, USA) and 60% biocompatible iron oxide (Fe_3O_4) nanoparticles made through the co-precipitation method [106, 174] were used in the experiment, as shown in figure 5-3.

A vibrating sample magnetometer (EV9, Microsense) was used to measure the magnetic characteristics of the microparticles (figure 5-3(b)). The hysteresis curve shows that the

microparticles are highly saturated in a 1.5 T (15000 Oe) magnetic field. The saturation magnetization is 30.4 emu/g. There is no hysteresis as expected for superparamagnetic particles. The microparticles are quasi-monodispersed with an average diameter of 230 ± 35 µm. They were used at a concentration of 0.21 mg/mL dispersed in saline (0.9 wt.% NaCl).

5.3.3 Preparation of the injector for testing

A complete prototype of the injector was built as described above. All experimentations were performed using a clinical 3 T MRI scanner (Skyra, Siemens, Erlangen, Germany). An MRI-compatible camera (MRC Systems GmbH, Heidelberg, Germany) used at a recording speed of 15 frames/s was utilized to record the performance of particle injections. Figure 5-4 shows the MRI-compatible actuator positioned in front of the MRI scanner.

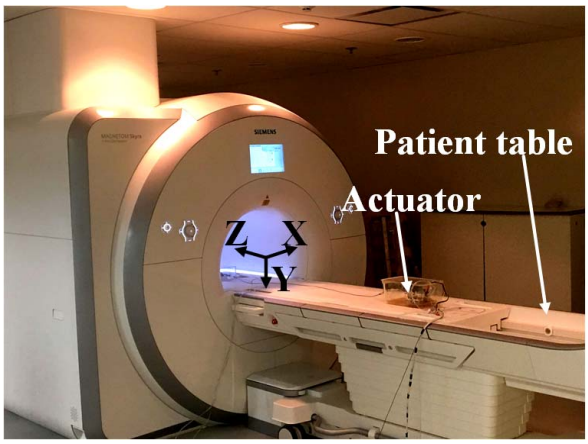

(a)

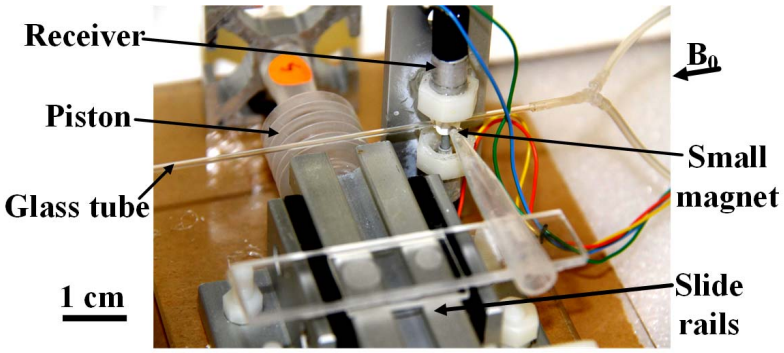

(b)

Figure 5-4: Setup of the MRI-compatible actuator during the experiments (a) and close-up of the actuator (b).

5.4 Experiments and results

5.4.1 System optimization

5.4.1.1 Determination of actuator position and orientation in MRI magnetic field

The main considerations that determined the position of the actuator were:

1) The actuator cannot be inside the MRI scanner because the bore only allows limited space for one patient.

2) The actuator can be easily installed on the patient table (see figure 5-4(a)), which is just in front of the MRI bore. The actuator and table can be positioned accurately at an optimal distance with respect to the iso-center of the MRI.

3) The actuator cannot be positioned far away from the MRI bore. Without a sufficient magnetic field strength, the encapsulated superparamagnetic nanoparticles would not be fully magnetized, leading to a fragmentation of aggregates after being released from the counting chamber.

4) If too close to the MRI scanner bore, the strong gradients due to the fringe field could attract the particles into the counting chamber of the actuator even in the absence of flow.

To determine the ideal position for our injection system, we measured the magnetic field strength in the direction of B_0 field (the 3 T homogeneous field) in front of the MRI system by using a digital Tesla meter (SENIS, Switzerland). After calibration to zero in the control room, the sensor was initially positioned at the center of the patient table, with a distance of 235 cm from the iso-center of the MRI bore. The table was moved with 10 cm increments in the B_0 direction, i.e. +Z direction (see figure 5-4(a)), until the sensor reached the gantry which is 85 cm away from the iso-center of the MRI bore. After obtaining the curve of the magnetic field distribution, magnetic gradients were taken from the tangent slope of the curve (see figure 5-5(a)).

The optimal position for the actuator was defined as the minimum distance at which particles had no movement induced by the fringe field in the absence of flow in order to obtain the highest particle magnetization without particle migration. To obtain the optimal position for the actuator, 20, 30, 40 and 50 particles were placed into the glass tube of the actuator. As the method we used to measure the magnetic field strength, the actuator was initially positioned at the center of the patient table, with an initial distance of 235 cm from the iso-center of the MRI bore. The table was

moved with 10 cm increments toward the B_0 direction until particles moved because of the fringe field. Experiments were repeated at least three times for each particle numbers. The results revealed that 185 cm is the optimal distance. There, the magnetic field strength was 0.045 T and the gradient 0.22 T/m, while no particle motion was observed in the tube.

Therefore, after the actuator was placed at the optimal position, we compared the shape of aggregates when the glass tube was positioned with angles of 0°, 45° and 90° to B_0 (figure 5-5(b)). As seen in figure 5-5(b), a single aggregate composed of 30 particles changed to three smaller ones when the angle was increased from 0° to 45°. When the glass tube and B_0 were perpendicular to each other, 8 chain-like aggregates (see C in figure 5-5(b)) were formed since the longer axis of aggregates was constrained by the internal diameter of the glass tube, limiting the particle number in each smaller aggregate.

Thus, in the following experiments, the glass tube of the counting chamber on the actuator was always kept parallel to B_0 and was positioned 185 cm away from the MRI iso-center.

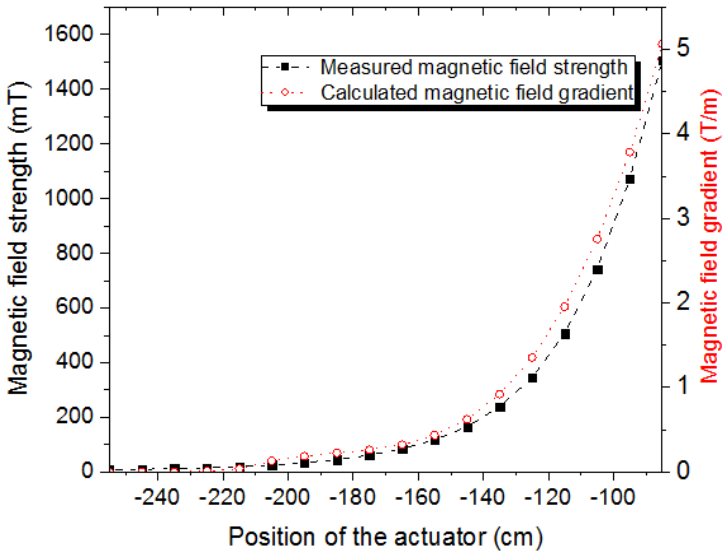

(a)

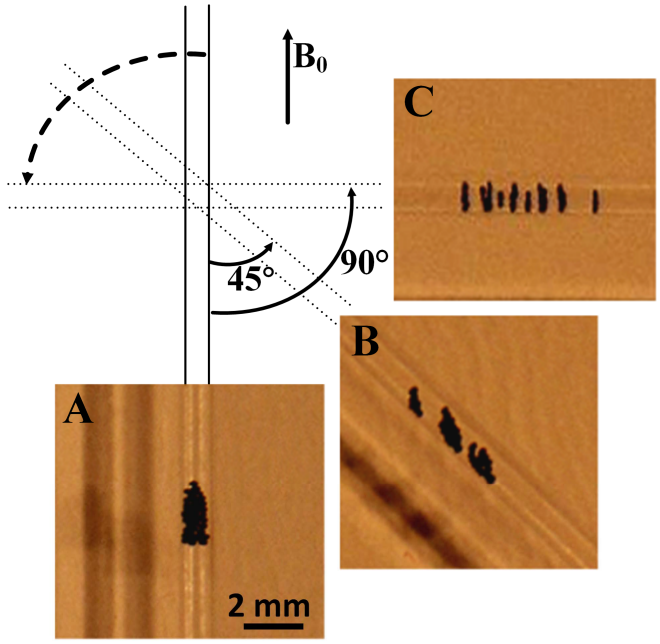

(b)

Figure 5-5: Mapping of the gradient strength according to the position of the actuator and shape of particle aggregates according to the orientation of the tube. (a) The strength of the magnetic field and the magnetic gradient along the +Z direction (B_0 direction). The iso-center of MRI bore was used as the reference zero (coordinates, 0, 0, 0). (b) Shapes of aggregates for different glass tube orientations with respect to the main field B_0.

5.4.1.2 Optimal flow rate for two pumps

After placing the actuator to the optimal position and orientation, the optimal flow rate for the two pumps was investigated. The calibration of the flow rate was done by measuring the pump output for a given injection time (30 s) according to the rotation speed and power frequency. Since the pump had a small diameter, was rotating at a high frequency and was connected to a 4.5 meters long tube, the flow in the actuator was almost constant. To determine the proper infusion rate for the two pumps, the initial flow was set to 6 mL/min and increased by 1 mL/min increments until the optimal flow rate was obtained.

The optimal flow rate from Pump 1 was defined as the highest flow at which particles can be effectively trapped by the magnet in order to minimize injection time while preventing unexpected particle release. At each flow rate, a single particle injection was performed three times. Microparticle migration from the trapping area was observed when the flow rate was higher than 16 mL/min, which was thereafter chosen as the optimal flow rate for Pump 1.

The optimal flow rate for Pump 2 was defined as the highest flow at which the aggregates cannot be broken by the effect of shear force. To obtain the optimal flow for Pump 2, 20 particles were injected into the actuator using Pump 1 and were released at different flow rates by Pump 2. A transparent tube (0.9 mm internal diameter), connected downstream to the actuator, was used to observe the shape of the particle aggregates. The experiment was also repeated three times at each flow rate. The optimal flow rate for Pump 2 was found to be 20 mL/min. With the same method and test times, the experiment results did not change when increasing the particle number to 30, 40 and 50 for each aggregate.

5.4.2 Controlling particle numbers and aggregate length by using our injector

Before determining the precise relationship between the R in Eq. 5-3 and the number of particles trapped in the glass tube, we roughly estimated it by injecting a known number of particles into the actuator to obtain a searching range. Twenty and sixty particles were selected because their aggregate sizes are 2 mm and 3.5 mm (see Fig. 5b) which falls perfectly within the desired range, according to hepatic vessel dimensions. The induced R in Eq. 5-3 were about 80 and 180 kΩ.

We set the bolus release resistance value between 80 and 180 kΩ with increments of 20 kΩ and performed five injections for each value. For each injection the number of particles present in the

aggregate was counted as follows: Pump 2 was manually switched off after the aggregate had reached a distance of about 135 cm away from the MRI iso-center and the transparent plastic tube was rotated at 90° such that the large aggregate breaks into several chain-like aggregates, while remaining at the same position because the magnetic force on particles was perpendicular to the tube wall. We observed that the particle aggregates always kept intact before rotating the tube. In our experiments, we manually tapped the tube in order to amplify the aggregates' "broking effect" until the particle number of each disaggregated aggregate was no more than 4, a counting method that is more efficient than only rotating the tube as seen in the phenomena in Fig. 5-5 (b)-C. This allowed an easy manual count.

After counting the particle number at different R in front of the MRI bore, we used new aggregates with the same R range used above to take the measurements of aggregate length inside the MRI bore. The aggregates were still advancing in the entry of the MRI bore induced by the fringe field after switching off Pump 2. They eventually stopped their progression when entering the area of the uniform static field B_0 inside the tunnel of the MRI system. At that time, the aggregates were always intact. The aggregate length was measured using the pictures taken from the videos obtained from the MRI-compatible camera. The camera was perpendicular to the B_0, making the length of each aggregate visible. The width was not measured as it was constrained by the inner diameter of the tube.

To quantitatively determine the relationship between the trapped particle number and R in Eq. 5-3, a linear regression was performed using the generalized least squares method (Figure 5-6(b)). From the regression result, we obtained the following expression for the particle number n:

$$n = 0.405\mathrm{R} - 12.23 \quad (80\ \mathrm{k\Omega} \leq \mathrm{R} \leq 180\ \mathrm{k\Omega}) \quad \text{(Eq. 5-4)}$$

Based on the linear regression, the formed aggregates ranged from 20 to 60 particles and the maximum observed error with the theoretical value was 6 particles. Another linear regression gave us the following expression for the relationship between aggregate length L and the receiver resistance R (figure 5-6(c)):

$$\mathrm{L} = 0.01579\mathrm{R} + 0.38286 \quad (80\ \mathrm{k\Omega} \leqslant \mathrm{R} \leqslant 180\ \mathrm{k\Omega}) \quad \text{(Eq. 5-5)}$$

The lengths of aggregates ranged from 1.6 to 3.2 mm and the maximum observed error with the theoretical value was 0.5 mm.

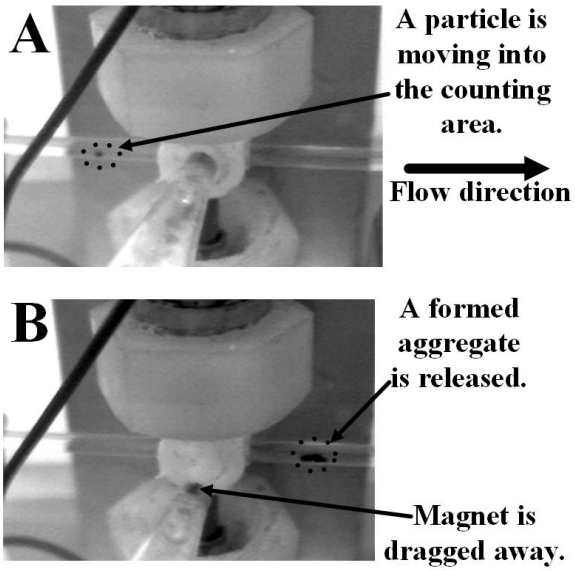
A
A particle is moving into the counting area.
Flow direction
B
A formed aggregate is released.
Magnet is dragged away.

(a)

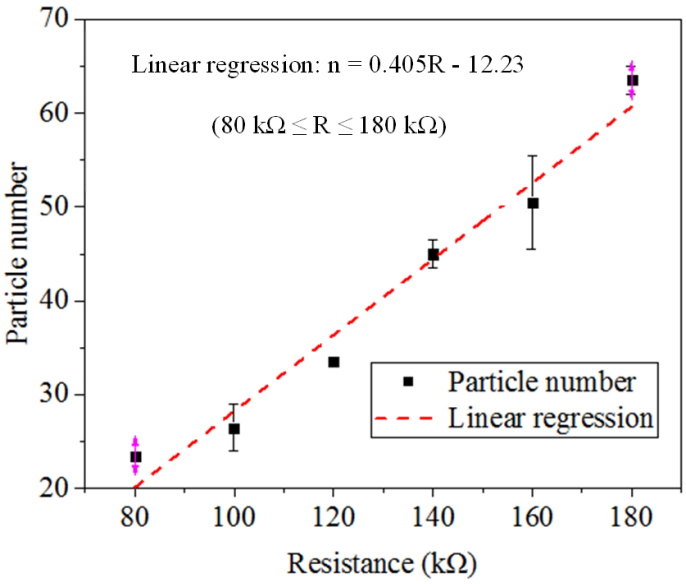
Linear regression: n = 0.405R - 12.23
(80 kΩ ≤ R ≤ 180 kΩ)
Particle number
Linear regression
Particle number
Resistance (kΩ)
70
60
50
40
30
20
80
100
120
140
160
180

(b)

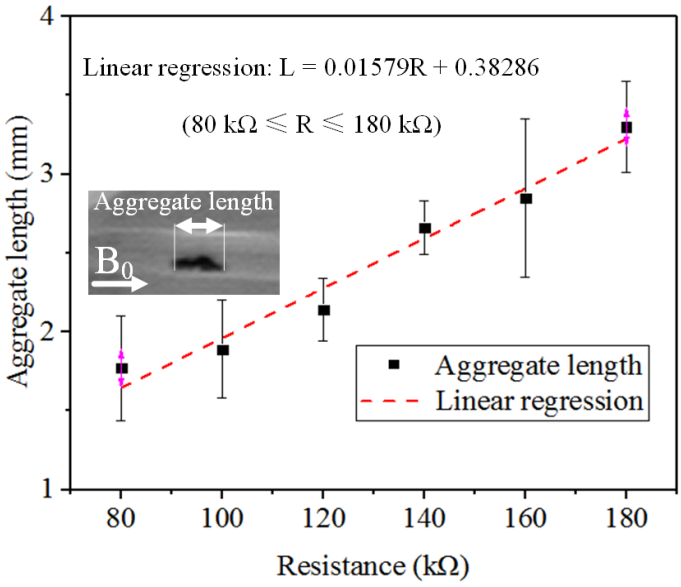

(c)

Figure 5-6: In (a), two snapshots showing a single particle (A) being injected into the counting chamber and a larger aggregate (B) being released after the resistance of the receiver reached the chosen value (Rc = 80 kΩ). The graphs show the relationship between receiver resistance and particle number (b) and the aggregate length (c). Data are shown as the mean ± standard deviation and n experiments = 5.

5.4.3 In-Vitro injectability and MR imaging capability tests

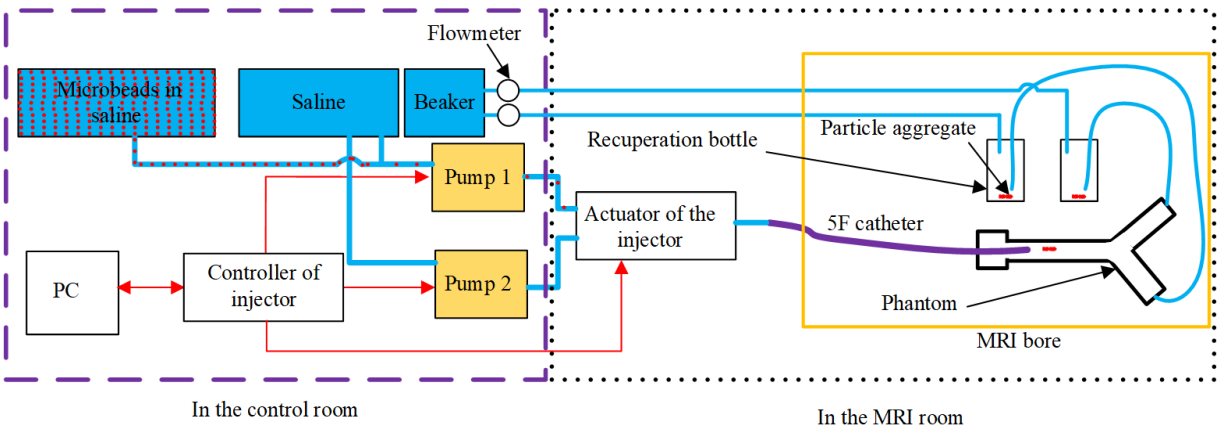

Figure 5-7: Experimental setup used for injecting the formed particle aggregates into a phantom located in the MRI scanner.

To check whether our injector could successfully deliver a particle aggregate in a vascular bifurcation, aggregates were injected into a symmetric Y-shaped glass tube inside the iso-center of the MRI bore. The experimental setup is depicted in figure 5-7. The tube had a constant inner diameter of 2.1 mm. We set an equal flow rate in the two branches of the bifurcation by using two GH-03217-24 150-mm correlated flowmeters (Cole-Parmer). Particle aggregates were injected through a 5 French, 150 cm long, 0.043' inner diameter straight Glidecath catheter (Terumo, Tokyo, Japan). The catheter tip was inserted into a Y-valve connected to the phantom. Two recuperation bottles were placed after the two output branches to collect particles. The R in Eq. 5-3 was set to accumulate aggregates made of 25 particles in the counting chamber. With this value, the length of the aggregate ranged from 1.3 to 2.1 mm, ensuring that it could pass easily through the 2.1 mm diameter tube. To prevent any possibility of occlusion in the tube by particles, Pump 2 was set at 0.6 mL/s when a particle aggregate reached the phantom. By checking video frames from the MRI-compatible camera, an injection was deemed successful if it satisfied two conditions:

1) A particle aggregate was effectively released into the phantom after actuation.

2) The released aggregate did not break apart before it reached the phantom branches.

The time required for an aggregate to pass through a 150 cm catheter (5 French) was about 4-5 s in the experiments conducted in this study. Based on 50 injections of aggregates, when the main branch was parallel to B_0 (see b in figure 5-8), 88% of the injections were recorded as successful while 10% of them broke into several aggregates and 2% could not be located by the video. The success rate was also examined when the angle between the main branch and B_0 was set at 45° and 90° (see c and d in figure 5-8)). After 50 injections at each angle, the success rate reached 86% (45°) and 82% (90°), respectively ($p = 0.78$).

Aggregates can be well imaged using spin-echo or gradient-echo sequences since they appeared as magnetic artifacts on the MRI acquisition performed after injection [175]. To image particle aggregates, T1-weighted spin echo images were acquired (TR = 900 ms, TE = 9.0 ms, pixel bandwidth = 250 Hz, slice thickness = 4.0 mm, slice interval = 4.3 mm). During the imaging acquisition (see e and f in figure 5-8), the flow was stopped such that the aggregate remains in a branch. We confirmed the location and absence of motion of the aggregate during MR acquisition by analyzing the video capture. The graph paper below the phantom helps us to pinpoint exactly

the position of the aggregate. The imaging experiments were repeated 4 times for each phantom orientation (0°, 45°, and 90° to B_0).

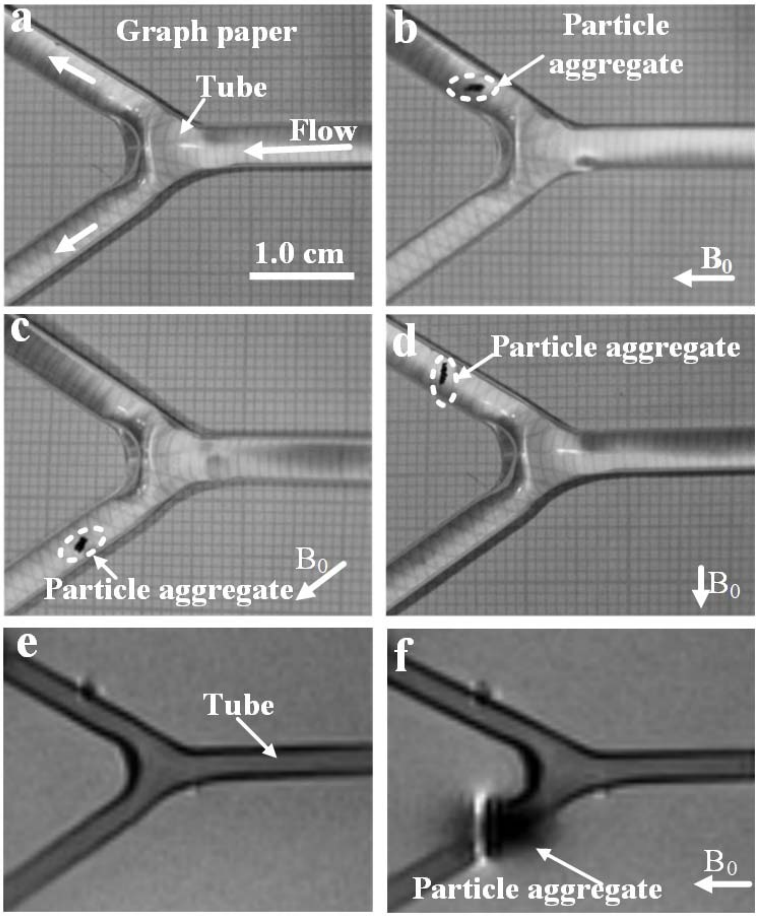

Figure 5-8: The movement of a particle aggregate in the phantom into the lower left tube branch is shown in the coronal direction (a, b, c, d) optically and (e, f) by magnetic resonance imaging. Fig. 5-8 a-d show the particle aggregates before (a) and after (b, c, d) entering the phantom with the help of an MRI-compatible camera. Fig. 5-8 e and f show a coronal image of the phantom taken before (e) and after (f) an aggregate reached the branch. The dark areas and white line around the particle aggregate were caused by susceptibility artifacts [134]. Note: 1. For different particle aggregates, the probability of entering different tube branches was random because there was no magnetic navigation force. We also randomly selected one video snapshot when the angle between the main branch and B_0 is 0°, 45° and 90° (see b, c, d). 2. MR correlation is only showed when the main branch and B_0 are parallel because different angulation to B_0 did not affect the imaging results.

5.5 Discussion

MRI-compatible injection systems should be able to handle both high magnetic fields and high gradients. The proposed injector proved to be capable of working properly inside a 3 T MRI magnetic field. Moreover, its design makes use of the fact that this field easily magnetizes and saturates superparamagnetic particles to form aggregates through dipole-dipole interactions. These aggregates exhibit higher magnetization than isolated particles and could be steered with more efficiency inside the MRI bore using the MR-imaging gradients. All these considerations have been taken into account in the development of this injector. Besides, in the context of MRN, for the same delivered dose, the procedure time would be significantly shorter when using aggregates instead of individual particles.

Once the aggregates are formed in the glass tube, they need to be injected into the circulatory system through an inserted catheter. To achieve a successful delivery, the ideal design requires the glass tube and catheter to have a similar internal diameter. Decreasing the internal diameter would increase its compatibility with smaller catheters but would significantly decrease the maximum possible number of particles per aggregate. The 82% success rate of aggregate injections with our current design is considered satisfactory since we were injecting with a constant flow of 0.6mL/s in a 2.1 mm internal diameter tube which is about the size of the segmental artery. The main hepatic artery has the internal diameter within the range of 4-5 mm. For the same flow rate (0.6mL/s), we can expect a decreased velocity and shear stress, thus fewer aggregate failures will occur at the level of the first branch division (right and left hepatic branch). The guidelines recommend segmental (super selective) over lobar (selective) embolization since whole liver embolization can lead to more complications (liver failure) [176]. Hence, it is crucial we can expect to have a higher proportion of intact aggregates and close to 100% selectivity at the first bifurcation (right/left lobe). We need a good but not necessarily perfect selectivity at the second bifurcation (segmental level) since non-target embolization beyond the second bifurcation is not clinically detrimental. We could also expect an increase in the success rate when using a vibrating flow that will reproduce a stop and go motion on the particles. By doing so, it will give a chance to the broken aggregates to re-aggregate with the magnetic field of MRI.

We were able to determine the optimal injection rate for Pump 1 and 2 to ensure that the particles can be injected in short periods of time while being effectively trapped by the magnet and then

released safely as aggregates. In our setup, the particle suspension was injected using Pump 1 which was about 4.5 meters away from the 3 T MRI scanner. In this area, the magnetic strength is lower than 0.0005 T and the gradient is close to 0 T/m. The main reason for this positioning was to prevent the formation of aggregates before the particles would reach the counting chamber. However, in some instance, aggregates are formed nevertheless which explains the small differences in particle number obtained for the same resistance value. Ideally, the particles should be injected into the glass tube one by one to accurately control the particle number in each aggregate. To prevent particle aggregate formation before they enter the counting chamber, increasing the mean distance between two adjacent particles is an easy yet effective method. It can be achieved by decreasing the internal diameter of the feeding tube from Pump 1. This will also induce a faster velocity, resulting in a shorter delivery time. However, a smaller diameter may increase the risks of clogging up the feeding tube. Another alternative is to decrease particle concentrations. However, this would increase the total fluid volume injected into the body as well as the procedural time. As shown above, since the magnetic field at the position of the actuator needs to be sufficiently strong to maintain the shape of the aggregates after being released, the position of the actuator cannot be changed arbitrarily. In our experimental setting, stepper motor-based pumps were used to inject particles and saline, which restricts the use of the pumps in the MRI room. Using MRI-compatible pumps and actuators may ultimately make the system more clinically compatible.

Our injector has demonstrated the ability to control the particle number in each aggregate. Although there are no drugs in particles used in this study, the possibility to load magnetic particles with doxorubicin (or other therapeutics) to create MDEBs has been previously demonstrated [17]. The ability to have a real-time estimation of particle numbers is an advantage since it renders feasible the calculation of the exact amount of drugs during chemoembolization with MDEBs which contain a fixed amount of drugs [177].

The 82% success rate of aggregate injections through a 5 French catheter makes our injector potentially useful for MRN, DFN and embolization performed after MR-Guided catheter navigation. Several teams have shown the feasibility of performing selective catheterization under the MR guidance [171, 178]. Besides the reduction of exposure to ionizing radiation for the staff performing these procedures routinely, the advantage of MRI over digital subtraction angiography is the possibility to add functional imaging to quantify flow, perfusion and also particle distribution when using magnetic particles [175, 179, 180].

The procedure time required is an important factor to be considered before any new medical technology is introduced. Regarding MRN, for a typical chemoembolization with drug-eluting beads, we need 2 ml of particles to load 75 mg of Doxorubicin (standard dose of 50 mg/m^2 body surface). For 100-300 μm particles (mean volume of 0.014 mm^3), it will take 140000 particles, while this number is only 18181 for the 300-500 μm particles (mean volume of 0.11 mm^3). Thus, the MRN would take 7.8 (100-300 μm particles) or 1 (300-500 μm particles) hour to inject if each aggregate has 25 particles and each navigation takes 5 s [181]. To decrease the procedure time, we can define an *in vivo* protocol starting with small particles to penetrate the tumor and then inject larger particles to occlude the flow and treat the tumor margin. Moreover, the gradient in our previous experiments was only 20 mT/m while the MRI can supply 40 mT/m [181]. Currently, the injector has the ability of forming an aggregate within 3 s. We can anticipate with higher gradients and a faster flow able to inject aggregates every 3 s and probably less after injector optimization. Thus, we can anticipate a therapy time below 2 hours which is not more than the time required for hyper-selective catheter-directed chemoembolization under fluoroscopic guidance.

Future work has been planned to navigate magnetic particles from the main hepatic artery to the second level bifurcation, allowing for a segmental embolization. In this setting, microcatheters will not be required and the MRN will be ideally performed through an implantable arterial port with a 4 or 5 French catheter, both of very similar internal diameters, positioned in the hepatic artery to avoid repeated catheterizations. We are currently working on the integration of this system with the MRN software to enable a synchronization of MDEB boluses with gradient actuations.

5.6 Conclusion

The proposed injector design is compatible with a controlled injection of magnetic particles inside an MRI bore. The particle numbers and aggregate sizes per injection can be set according to the actual demands. Each aggregate contains 20 to 60 microparticles with a precision of 6 particles and the corresponding aggregate length is 1.6 to 3.2 mm. At last, we have demonstrated that our formed aggregates can be injected into the MRI bore without breaking apart using a 5 French catheter. The success rate of aggregate injections is no less than 82%.

ACKNOWLEDGEMENTS

The authors acknowledge Yasamin Majedi and Yuting Jiang for their assistance during the paper modification.

CHAPTER 6 ARTICLE 3: MAGNETIC RESONCANCE NAVIGATION FOR TARGETED EMBOLIZATION IN A TWO-LEVEL BIFURCATION PHANTOM

Ning Li [1],Yuting Jiang[2, 3], Rosalie Plantefève[2], Francois Michaud [2,3], Zeynab Nosrati[4], Charles Tremblay[1], Katayoun Saatchi[4], Urs O. Häfeli [4], Samuel Kadoury[1,2], Gerald Moran[5], Florian Joly[6] , Sylvain Martel[1], Gilles Soulez[2,3]

[1] Laboratory of NanoRobotics, Department of Computer Engineering, Institute of Biomedical Engineering, Polytechnique Montreal, Montreal, QC, Canada.

[2] Laboratoire clinique du traitement de l'image, Centre de recherche du Centre Hospitalier de l'Université de Montréal (CRCHUM), Montréal, Québec, Canada.

[3] Department of Radiology, Radiation Oncology and Nuclear Medicine, University of Montréal, Montreal, QC, Canada.

[4] Faculty of Pharmaceutical Sciences, University of British Columbia, Vancouver, BC, Canada.

[5] Siemens Canada, Oakville, ON, Canada.

[6] National Institute for Research in Computer Science and Control, Paris, France.

Submitted to *Annals of biomedical engineering,* on 30 January 2019. (Manuscript Number: ABME-D-19-00091).

6.1 Abstract

This work combines a particle injection system with our proposed magnetic resonance navigation (MRN) sequence with the intention of validating MRN in a two-bifurcation phantom for endovascular treatment of hepatocellular carcinoma (HCC). A theoretical physical model used to calculate the most appropriate size of the magnetic drug-eluting bead (MDEB, 200 μm) aggregates was proposed. The aggregates were injected into the phantom by a dedicated particle injector while a trigger signal was automatically sent to the MRI to start MRN which consists of interleaved tracking and steering sequences. When the main branch of the phantom was parallel to B_0, the aggregate distribution ratio in the left–left, left–right, right–left and right–right divisions was obtained with results of 8%, 68%, 24% and 0% respectively at baseline (no MRN) and

increased to 84%, 100%, 84% and 92% ($P < 0.001$, $P = 0.004$, $P < 0.001$, $P < 0.001$) after implementing our MRN protocol. When the main branch was perpendicular to B_0, the right-left branch, having the smallest baseline distribution rate of 0%, reached 80% ($P < 0.001$) after applying MRN. Moreover, the success rate of MRN was always more than 92% at the 1st bifurcation in the experiments above.

Key words—Magnetic resonance navigation, two-bifurcations navigation, hepatocellular carcinoma, embolization.

6.2 Introduction

Liver cancer is the third most frequent cause of cancer-related deaths worldwide, among which, hepatocellular carcinoma (HCC), the most common type of this disease, makes up approximately 80%-90% of all cases of primary liver cancer in the United States [182]. Surgical resection, liver transplantation and transcatheter arterial chemoembolization (TACE) are three therapeutic choices used to treat HCC [2]. Surgical resection is generally associated with better prognoses. However, poor liver function and/or the disease's severity prevent more than 70% of the patients to be eligible for surgical resection [183]. Liver transplantation eligibility is also limited. Recent reports published on the website of the U.S. Department of Health & Human Services (OPTN) have shown that among those patients who are eligible and placed in the waiting list, only about 40-50% of them will undergo liver transplantation per year. Meanwhile, TACE, a palliative treatment, has a wider range of applications. It is not only suitable for patients with intermediate stage HCC ineligible for surgery or transplantation, but can also be used as a temporary treatment to downsize tumor burden and bridge patients before liver transplantation, thus potentially reducing the waitlist mortality rate and/or resection surgeries [184]. TACE requires selective catheterization and intra-arterial infusion of a chemotherapeutic agent combined with embolization [185]. Conventional TACE consists of the injection of chemotherapeutic drugs mixed with an oil-based contrast medium (Lipiodol), followed by the occlusion of feeding hepatic arteries supplying the tumor with an embolizing agent [186]. Nowadays, anti-tumorous drugs can be encapsulated into biodegradable microbeads called drug-eluting beads (DEBs) [17]. Compared with conventional TACE which involves the sequential injection of drugs and beads, DEBs have the ability to simultaneously embolize arteries and deliver the chemotherapeutic drug. Moreover, the drug encapsulated into the microbeads can be slowly released with their breakdown, thus increasing drug concentration and

therapeutic window while lowering the probability of hepatoxicity [111]. During TACE, the beads are injected supra-selectively into the tumor arterial feeders arising from the branch divisions of the hepatic artery through a catheter inserted by femoral or radial approach [44]. Current limitations of conventional and DEB TACE for liver tumors are: 1) Lack of selective tumoral targeting after release from the catheter and the need for supra-selective catheterization; 2) Potential damage to healthy liver tissues due to non-targeted embolization; 3) Poor visualization of tumor coverage after embolization; and 4) Invasiveness of the procedure requiring supra-selective catheterization, repeated embolization sessions, exposure to ionizing radiation and iodine contrast in addition to potential hospitalization for complications.

Magnetic resonance navigation (MRN) uses the outstanding imaging properties of MRI to detect liver tumors [187], the B_0 magnetic field to magnetize MDEBs and the imaging gradient generated by imaging gradient coils to steer them in the segmental arteries feeding the liver tumor network [188]. MDEBs could be released from an intra-arterial implantable port positioned in the hepatic artery percutaneously [189]. Advantages of an approach combining MDEB-TACE by MRN include: 1) Eliminating the need for repeated invasive and complex catheterization procedures; 2) Treatment fragmentation to improve efficacy while reducing morbidity; and 3) Real-time monitoring of MDEB distribution in the tumor with MRI.

The MRN technology can be divided into 5 steps below (Fig. 6-1):

1. Particle design

It has been demonstrated that 100-300 μm sized DEBs have the best tumor penetration with, potentially, better drug delivery than larger particle [111, 173] and less liver complications than smaller DEBs [106, 112]. Within this size range, the particles delivered can penetrate the tumor and its margin [56].

For this purpose, 200 μm MDEBs made of Fe_3O_4 superparamagnetic nanoparticles encapsulated with the therapeutic payload (Doxorubicin (DOX)) in a biocompatible biodegradable polymer (PGLA) are used [17, 106]. Those magnetic nanoparticles (5–20 nm) are nanosized so that they can be phagocytosed without any negative or toxic effects after the MDEBs have biodegraded into the body [104]. Moreover, the superparamagnetic property of the nanoparticles makes it so that the MDEB have no remnant magnetization once the patient is removed from the MRI field [105].

2. Flow control

The method used to control arterial flow is very important for MRN techniques because blood flow will drive and drag the particles forward. Since the MRN steering force on MDEB aggregates is limited, we need to control the flow to have enough time to deviate the particles into the target branches. We have demonstrated that the combination of vibrating and constant flow can generate a stop and go motion of the MDEB aggregates [190]. In our previous experiments, the vibrating flow could maintain a vibrating status over the particles, thus the attractive forces, such as dipolar interactions, could be overcome. Therefore, with a small displacement vector and MRN steering force, we can obtain satisfactory MRN success rates.

3. Formation of microparticle aggregates with controllable sizes

Injecting particle aggregates is a better choice compared to single-particle injections because:

(1) The internal diameter of the third level (segmental) hepatic arteries is about 1-4 mm [172], which allows larger particle aggregates to enter the arteries.

(2) An overall bigger size can make MRN easier since the aggregates' velocity and the induced magnetic force acting on them increase at, respectively, quadratic and cubic rates with aggregate sizes [190].

(3) The total therapeutic time will be significantly reduced compared to the single-particle injections since fewer injections will be required for the same amount of therapeutic drug.

(4) The aggregates that have reached the targeted branch can break into individual particles and move to the proximity of the tumor margin after patients are moved out of the MRI field.

Once particle aggregates are in the MRI scanner, the aggregates have a longer axis along the B_0 direction, meaning they are more elongated in the B_0 direction [115]. Owing to the fact that the orientation of most hepatic vessels may point to any 3D direction while the B_0 generated by an MRI is always in the Z direction, an appropriate range for the aggregates' sizes needs to be established in order to make it possible for them to be navigated into selected vessels. Although an MRI-compatible particle injector has been previously proposed by our research group, that work only focused on controlling the size of particle aggregates, and did not study the influence of MDEB aggregate sizes and vessel orientations on MRN performance [191]. This paper is an attempt to elucidate this new field.

4. MRN software

Previous works have been done to navigate a single millimetric magnetic bead across 2 or 3 bifurcations which is not applicable for DEB-TACE [116]. After the injection of MDEB aggregates, the navigation of those aggregates is controlled by MRN sequences. Unlike in single-bifurcation MDEB aggregate navigations where the magnetic gradient points continuously towards a single direction, as we have done previously [192], when doing multi-bifurcations navigations, the MRN software must be able to achieve two functions: first, track particles, which is mainly used to determine when or where to change the gradient direction based on the aggregate's position while taking into consideration the vessel bifurcations' orientations; and second, particle navigation, which uses the gradient coils to apply magnetic forces onto the MDEB aggregates.

5. Integration of all parts to achieve successful MRN.

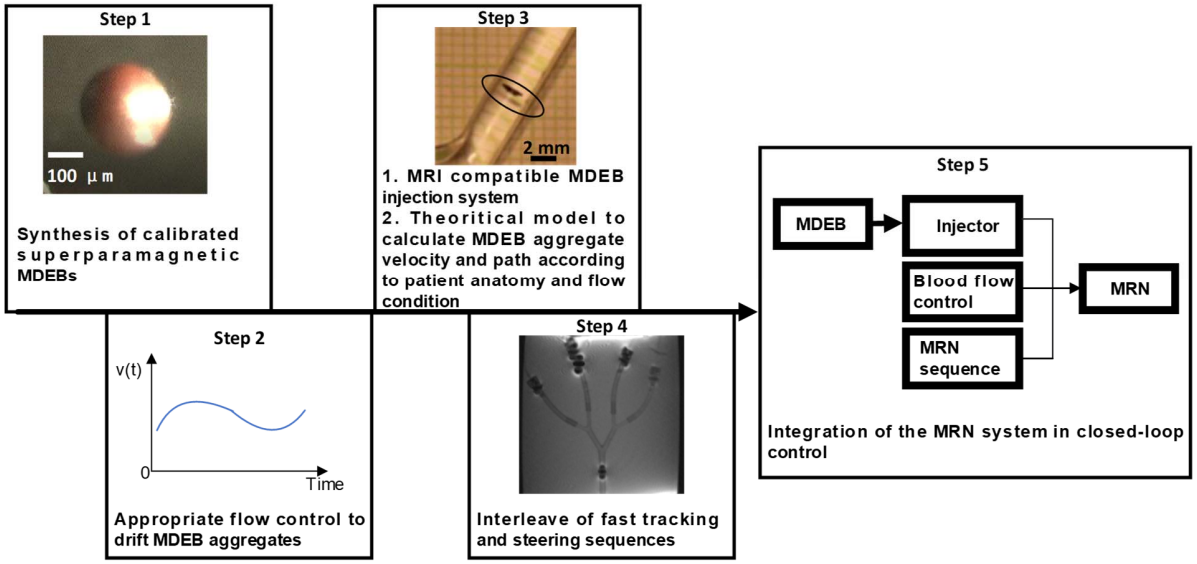

Figure 6-1: Five steps of the MRN technology and the corresponding research work for each step. Step 1 shows a single DEB (diameter = 200 µm), Step 2 shows the oscillating flow pattern used in this paper, Step 3 shows the formation of a MDEB aggregate after its injection in the phantom, and Step 4 shows the MDEB aggregate position by True FISP acquisition.

Table 6-1: Research status of the MRN in relation to this work's aims

Research team	Microparticle design	Particle aggregate with controllable size	Presence of flow	MR steering	MR tracking	Bifurcation number
Pouponneau et al. 2011 [17]	Y	N	Y	Y	N	1
Bigot et al. 2014 [117]	N	N	N	Y	N	3
Mellal et al. 2015 [164]	Y	N	Y	Y	Y	1
Felfoul et al. 2016 [188]	N	N	N	Y	Y	> 3
Li et al. 2017 [190]	Y	N	Y	Y	N	1
Li et al. 2018 [191]	Y	Y	N	N	N	1
Michaud et al. 2018 [192]	Y	Y	Y	Y	N	1
Our aims	Y	Y	Y	Y	Y	2

Table 6-1 lists recent MRN research along with our proposed studies. The MRN field has significantly progressed over the last few years, but no single research group has simultaneously investigated all the steps necessary for a real-life MRN operation as explained above.

This work aims to combine the particle injection system with our proposed MRN sequence with the intention of achieving MRN of MDEB aggregates in a two-bifurcation phantom. Using the 200 μm MDEBs reported recently by our research group, our three most important objectives are first, to propose a theoretical model as a means to calculate the most appropriate MDEB aggregate size to optimize MRN; second, to design MRN sequence interleaving tracking and navigation of those

aggregates; and third, to integrate the MDEB aggregate injection system with the MRN software to show the MRN accuracy in a two-bifurcation vascular phantom.

To the best of our knowledge, the device we are proposing is the first injector-MRI synchronization system that possesses the capability to form, track, and navigate MDEB aggregates in a two-bifurcation phantom.

6.3 Materials and methods

6.3.1 Particle design and agglomeration with proper sizing

The particles (200 μm), composed of poly-(lactic-co-glycolic) acid (PLGA) and superparamagnetic biocompatible iron oxide (Fe_3O_4) nanoparticles, have been described previously [106]. The nanoparticles have a diameter of 12 ± 3.6 nm which allows them to be phagocytosed [165]. Their saturation magnetization is 30 emu/g (≥ 1.5 T) based on the hysteresis curve determined in a vibrating sample magnetometer (EV9, Microsense). For this set of experiments, we did not load the MDEBs with doxorubicin.

The magnitude of the magnetic gradient (20 mT/m) was too weak to guide a single MDEB. Thus, large magnetic aggregates were created while ensuring their overall size was always smaller than the internal diameter of the targeted vessels. Here, an MR-compatible injector was used to control aggregate sizes, as well as the number of particles per aggregate [191].

To determine the characteristics of an aggregate that has both an optimal size and a high-steering efficiency, a simple theoretical model was proposed. When an ellipsoidal particle aggregate is injected into a tube, the aggregate will be at the lowest position of the tube since its gravity is greater than the liquid buoyancy (Figure 6-2 (left)). The longer axis of any aggregate is always parallel to the B_0 direction. To navigate the aggregate into a targeted branch, the magnetic force must induce a sufficient deviation from the centerline to ensure the whole aggregate will enter the targeted branch. The magnitude of this deviation will vary according to the diameter of the vessel and the angulation of the long axis of the vessel and B_0 (see figure 6-2, right). The equation below summarizes the situation:

$$\frac{L}{2}\sin Q \leq d \qquad \text{(Eq. 6-1)}$$

where L is the length of a particle aggregate and d is the displacement of the aggregate from the tube's center-axis that is induced by the magnetic gradient force and Q the angulation between vessel centerline and B_0.

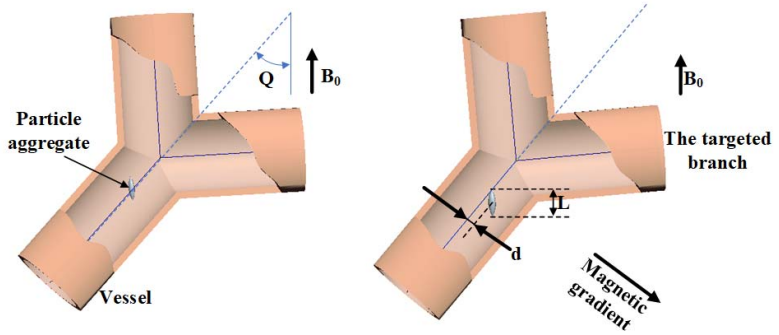

(a)

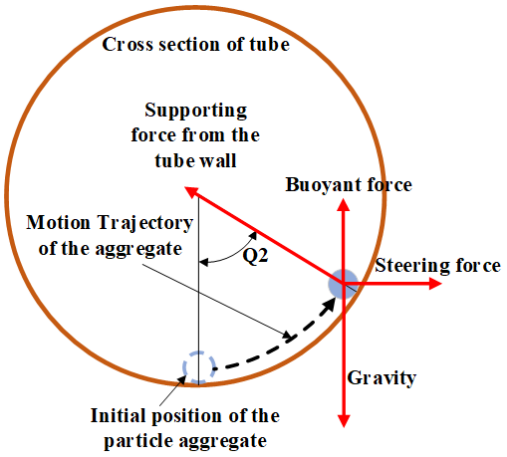

(b)

Figure 6-2: A schematic diagram showing a longitudinal view, an aggregate reaching the bifurcation of the tube with (a-right) and without (a-left) magnetic gradients. The angle between the centerline of the tube and B_0 is Q. In (b), we show, on an axial view, the aggregate motion along the vessel wall and the interaction between magnetic, gravitational and buoyant forces during MRN. Note that: in the calculation of Q_2, we ignore the effect of the particle size.

The magnetic force $\boldsymbol{F_m}$ acting on all particles is

$$\mathbf{F}_m = V_p \ (\boldsymbol{M_p} \bullet \nabla) \ \mathbf{B} \qquad \text{(Eq. 6-2)}$$

where V_p is the volume of magnetic particles (m^3), M_p the magnetization of the particles (A/m), **B** the strength of the magnetic field (T), and $\nabla \boldsymbol{B}$ the magnetic gradient (T/m). If the adhesion forces between the particles and the substrate surface is 0, the rotation angles (Q_2, see figure 6-2(b)) of the particles around the centerline of vessels and in the longitudinal section of the tube or vessel can be calculated using

$$Q_2 = Arc\tan\left(\frac{\boldsymbol{F_m}}{(\rho_p-\rho_f)\cdot V_p \cdot g}\right) \quad \text{(Eq. 6-3)}$$

where, ρ_p is the MMS density (kg/m^3), ρ_f the fluidic density (kg/m^3) and g the acceleration of gravity (N/kg). The displacement d of the aggregate from the tube's center-axis can be calculated using

$$d = \mathrm{r} \cdot \sin Q_2 \quad \text{(Eq. 6-4)}$$

where r is the radius of the tube.

From the Eq. 6-1-Eq. 6-4, we can get that

$$L \leq 2 \cdot r \cdot \left(\frac{\sin\left(Arc\tan\left(\frac{(\boldsymbol{M_p}\bullet\nabla)\,\mathbf{B}}{(\rho_p-\rho_f)\cdot g}\right)\right)}{\sin Q}\right) \quad \text{(Eq. 6-5)}$$

6.3.2 Synchronization of the MRN sequence

All experiments reported in this paper were performed with a 3 T clinical MRI scanner (Skyra, Siemens, Erlangen, Germany). It is important to have a good synchronization between aggregate release and MRN especially under in vivo conditions due to the presence of blood flow [117]. Therefore, MRN sequences must start automatically after an aggregate is released from the injector. To achieve it, a 2-V, 100-ms pulse rectangular trigger signal generated by a trigger generator is sent to the scanner. The actuator was located 1.8-m away from the MRI's iso-center. After a bolus is released from the injector, the time required to arrive at the phantom was estimated at 4 seconds. Thus, the trigger signal was set at a 4-sec delay in order to decrease the actuation of MRN sequence and minimize heat accumulation, which can be quite damaging to the MRI system.

6.3.3 MRN sequence for particle steering and tracking

The overall MRN sequence is made up of two major parts: a gradient sequence and an imaging sequence. Hence, it is necessary to determine a gradient time (T_g, see figure 6-3) within each MRN segment for particle steering and select an optimal MRI sequence for particle tracking.

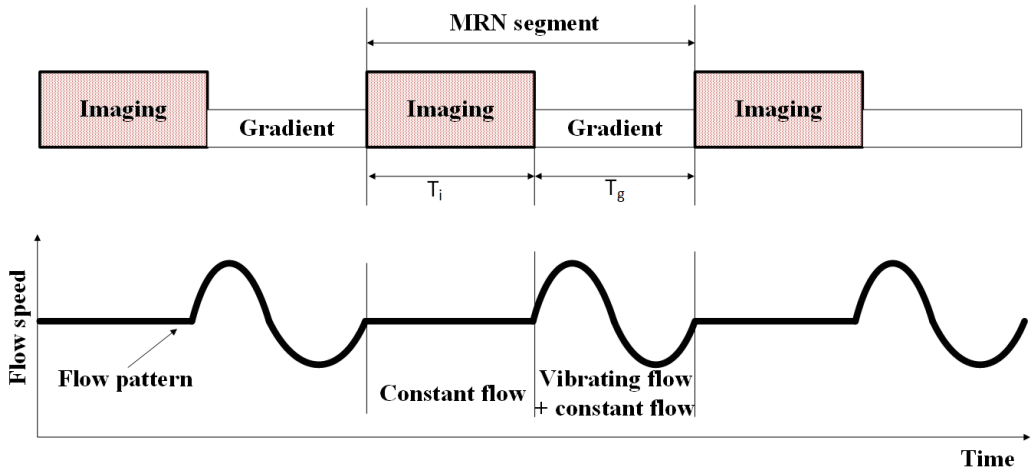

Figure 6-3: A schematic drawing of the MRN sequence (upper) and the corresponding fluid pattern (downwards). The flow pattern ensures that the particle only moves when the gradients are operational.

Before determining a proper T_g, a gradient sequence was programmed by the Integrated Development Environment for (MR) Applications (IDEA, Siemens, Germany), which is able to produce a constant gradient in any desired 3D direction. For the first branch division, the gradient is applied to steer the MDEB aggregate in the targeted branch division. After the aggregate had passed through the first bifurcation, the gradient's direction needs to be adjusted based on the orientation of the second targeted branch. This meant that the aggregate had to be localized between the first and second bifurcation. We then estimated the shortest time T_s required for aggregates to transit from the first to the second targeted branch. To have a good steering efficiency T_g need to be close to or smaller than T_s. Our previous research has demonstrated that the combination of a constant flow and an oscillating bypass flow can induce a stop and go motion of the aggregate [190]. The aggregate will move only when the vibrating flow is on. This stop and go motion was recorded by an MRI-compatible camera (MRC Systems GmbH, Heidelberg, Germany). By analyzing the videos, we obtained T_s.

Regarding particle tracking, the sequence needs to be optimized to obtain a high temporal resolution with an acceptable spatial resolution to track the susceptible magnetic artifacts [94]. The

tracking of the magnetic nanoparticle aggregates has been tested by our research group using a steady-state coherent sequence (True FISP) with the following parameters: TR = 4.23 ms, TE = 2.12 ms, pixel spacing = 0.83 × 0.83 mm^2, imaging resolution = 192 × 192, slice thickness = 8.0 mm, scanning time for a single image = 1.01 s [22].

6.3.4 Experimental setup

A symmetric transparent glass phantom was built to mimic a hepatic arterial tree (Figure 6-4(a)). The main, first and second branches had internal diameters of 4 mm, 3 mm, and 2 mm, respectively. These values were selected because the sizes were within dimension ranges of the main hepatic artery and the secondary branches. For each tube junction, the angle between the two bifurcations was set at 60° and the distance between the first and second bifurcation was set to 2 cm. The phantom was sealed at the center of a rectangular box (20 cm × 10 cm × 8 cm) filled with saline. A 5 French, 150 cm long, 0.043' inner diameter straight Glidecath catheter (Terumo, Tokyo, Japan) was inserted into the main branch of the glass phantom. The position of the catheter's tip was positioned 3.5 cm away from the first bifurcation. The hub of the catheter was connected to the actuator of our particle injector. The test phantom was put onto the MRI patient table and positioned in the iso-center of the MRI scanner bore.

The catheter was introduced into the glass phantom through a 5 Fr introducer sheath allowing the injection of a bypass flow injected around the catheter. The catheter itself was perfused with a constant flow (0.2 mL/s) generated by one of the injector pumps (see the controller of the injector in figure 6-4(b)). The bypass flow was set to 0.4 mL/s, to reproduce the flow obtained in previous in vivo experiments [192]. The bypass flow oscillated with a frequency of 1 Hz and an amplitude of 0.4 mL to generate a stop and go motion of the MDEB aggregates.

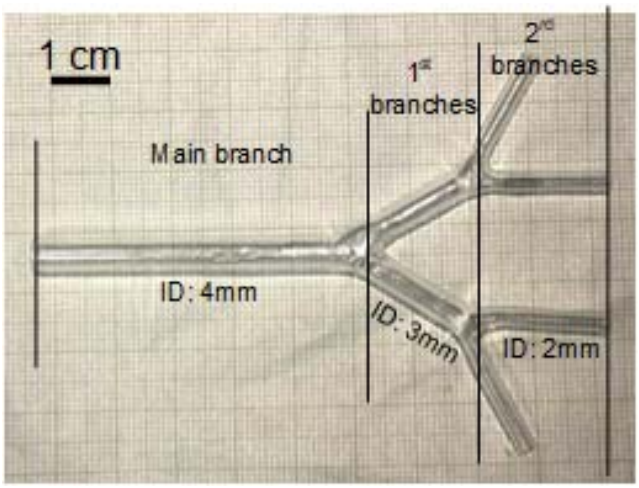

(a)

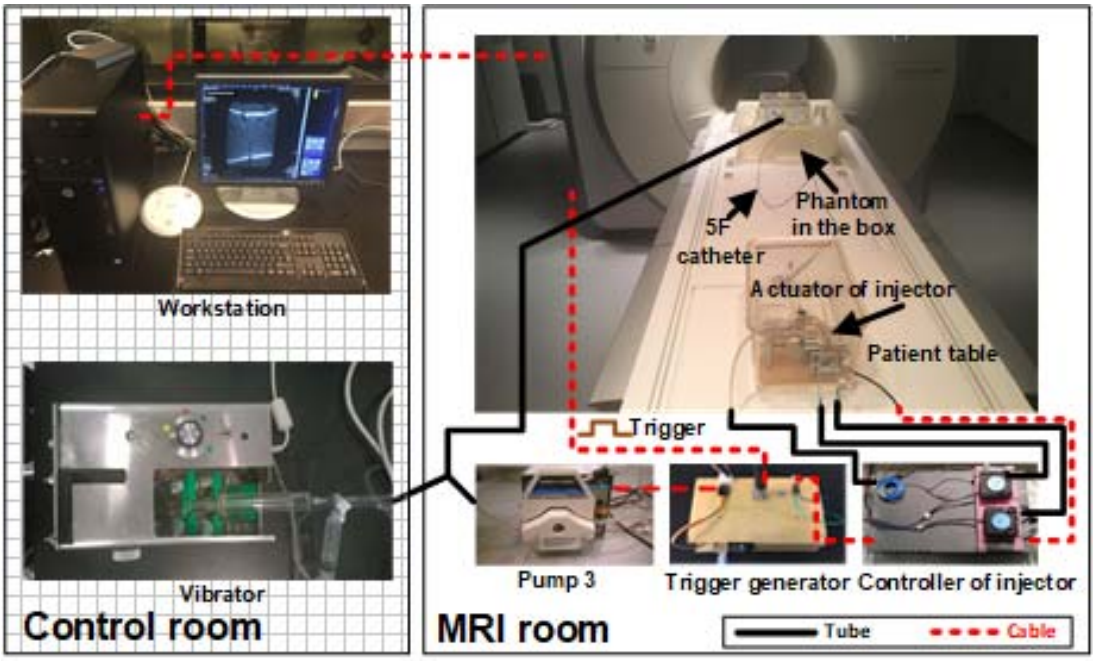

(b)

Figure 6-4: (a) Glass phantom used for MRN. (b) Integration of MRN and automated injection system.

A 20 mT/m steering gradient was continuously applied perpendicular to the centerline of the current branch pointing in the direction of the next targeted branch. The steering gradient was set off following each successful branch embolization.

6.4 Results

6.4.1 MDEB aggregate sizing and MDEB count

The appropriate aggregate length was calculated when the main branch was either parallel or perpendicular to B_0. The length of the aggregate needs to be shorter when the lumen centerline is perpendicular to B_0 since the long axis of the aggregate will be aligned to B_0 and then have a perpendicular orientation to the target branch division. From the Eq. 6-5 ($\rho_p = 2.1\ g/cm^3$, $\rho_s = 1.0046\ g/cm^3$, $r = 3\ mm$, $\nabla \boldsymbol{B} = 20$ mT/m and $g = 9.8\ N/kg$), we have obtained that the maximum length (L) of aggregates should be about 1.2 mm. which correspond to 16 MDEBs [191].

The resistance of the counting chamber was set to inject 16 MDEB per aggregates. Thirty aggregates were continuously injected, and we manually counted the precise number of individual particles in each aggregate. The results are presented in figure 6-5.

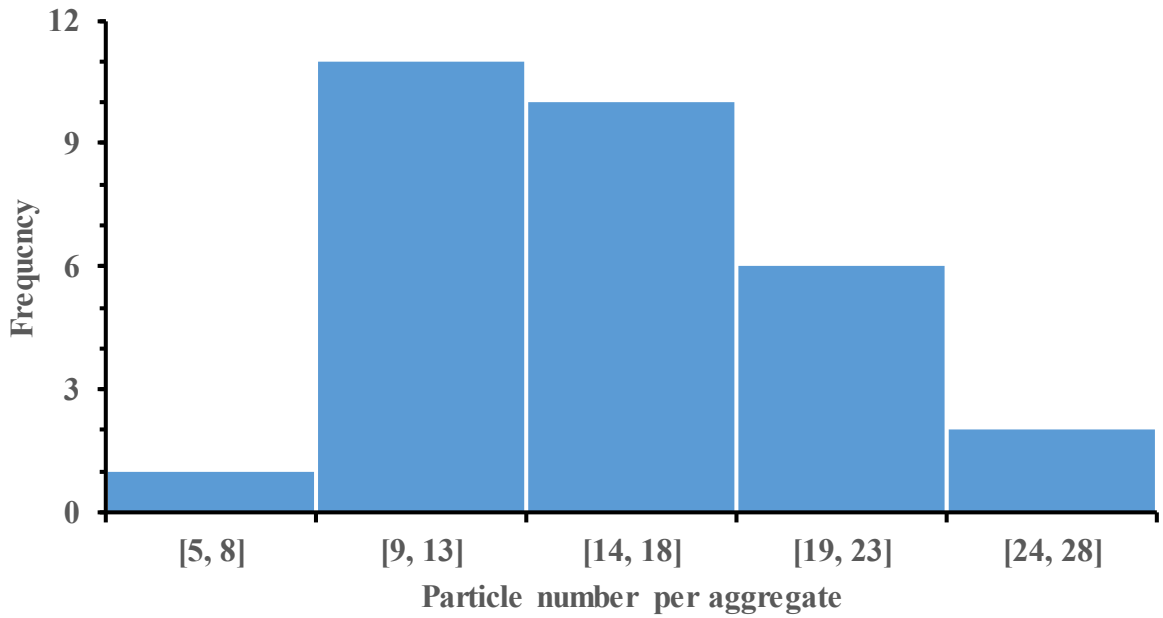

Figure 6-5: Particle number per aggregate.

The average value was about 15.83 MDEBs per aggregate with a standard deviation of about 5.17 particles, the maximum value being 28 and the minimum value being 5. We used a high concentration of particle upstream from the injector to reduce the time required for aggregate formation. But this may cause upstream aggregation of particles and lead to the release of

aggregates exceeding the desired particle number, mainly towards the higher end. Despite the above issue and range of aggregate sizes, the mean length of particle aggregates was estimated at 1.2 ± 0.5 mm with this particular particle number [191], matching our theoretical value for MRN.

6.4.2 Determine the parameters of MRN sequence

To determine T_s, which is the shortest transit time between the 1st and 2nd bifurcation, 34 aggregates were released into the phantom without MRN using the vibrating flow detailed above. After analyzing the video captures, T_s was estimated at 1.79 ± 0.64 seconds (mean ± standard deviation). Here, T_g was set to a similar value (2 seconds): it means that the vibrating flow and magnetic steering gradients both simultaneously lasted for 2 seconds in each MRN segment. When a particle aggregate was detected in the first branches, the gradient direction would be altered accordingly. Figure 6-6 shows a particle aggregate arriving at the first and second bifurcations, in different pathways.

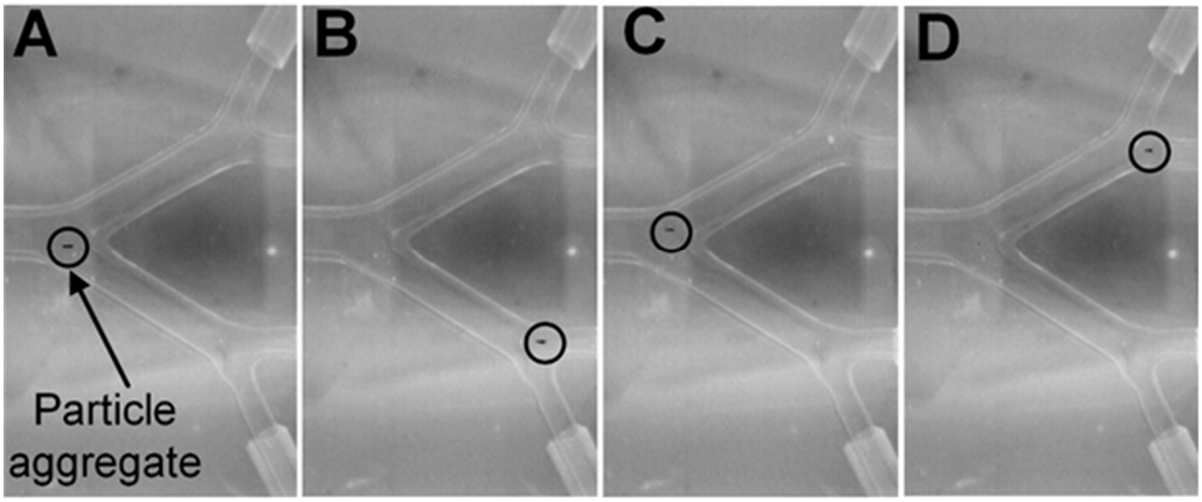

Figure 6-6: The images show the movement of a single particle aggregate from the first bifurcation （A or C） to the two second bifurcations (B or D).

The optimization of acquisition times and spatial resolutions during MRN (T_i, see figure 6-3) was done using the True FISP sequence and an aggregate consisting of 16 particles injected into the glass phantom. The vibrating flow was stopped in order to make the aggregates settle down into the main branch. The following imaging parameters (TR = 440.8 ms, TE = 1.7 ms, pixel bandwidth = 1020 Hz, slice thickness = 10 mm) were used. Three different resolutions: 80 × 80, 192 × 192 and 288 × 288 were tested. Then, the image quality of each capture was optically

evaluated. In table 6-2, the imaging time required for different resolutions is shown. Figure 6-7 shows the captured images of aggregates for three different spatial resolutions. For the following MRN experiments, the highest resolution (288 × 288) was selected since it had the clearest image of the MDEB aggregate which is optimal for pinpointing an object's position, although it takes 4x longer to the image than the 80 × 80 resolution. However, the required scanning time for each image was 0.43 second.

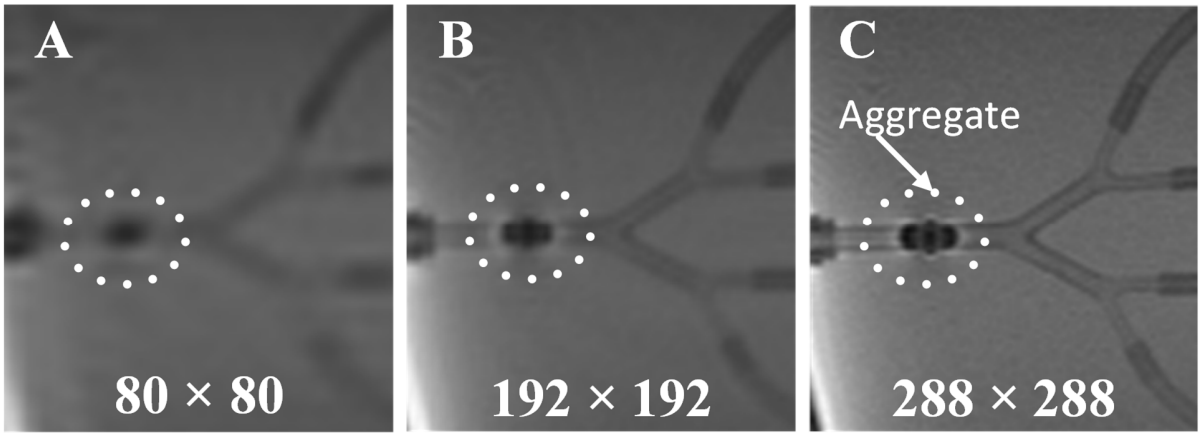

Figure 6-7: The MR images of an aggregate at three different resolutions.

Table 6-2: Imaging time required at different resolutions

Resolution	TR (ms)	TE (ms)	BW (Hz)	ST (mm)	Time (s)
80 × 80	104.5	1.2	1010	10	0.1
96 × 96	125.4	1.3	1000		0.12
112 × 112	146.5	1.3	1000		0.14
128 × 128	166.9	1.3	1000		0.16
144 × 144	190.3	1.4	990		0.18
160 × 160	214.2	1.4	1010		0.21
176 × 176	237.5	1.4	1015		0.23
192 × 192	263.2	1.5	1000		0.26
208 × 208	289.8	1.5	1000		0.28
224 × 224	316.5	1.5	1015		0.31
240 × 240	346.9	1.6	990		0.34
256 × 256	377.5	1.6	975		0.37
272 × 272	407.0	1.6	1020		0.4
288 × 288	440.8	1.7	1020		0.43

*Note: BW = bandwidth; ST = slice thickness.

6.4.3 *In vitro* MRN

After establishing the experimental parameters above, MRN was used to guide particle aggregates inside the two-bifurcation phantom. Figure 6-8 shows particle aggregates that were navigated into four different second-level branches, when the main tube of the phantom is either parallel (A-F) or perpendicular (G-L) to B_0. To get a precise evaluation of our MRN efficiency, the success rate of MRN was defined as the aggregate number capable of reaching the targeted branch divided by the total number of injections. When the main tube was parallel to B_0, the aggregates (n = 25) without MRN were divided into 8%, 68%, 24% and 0% for the pathways L-L (Left-Left), L-R (Left-Right), R-L (Right-Left) and R-R (Right-Right), respectively. With MRN, the success rate was 84%, 100%, 84% and 92% ($P < 0.001$, $P = 0.004$, $P < 0.001$, $P < 0.001$) for each pathway respectively (same order as above). We also gave an estimation of the success rate at the first branch division. For MRN performed for the pathways R-L and R-R when the main tube was parallel to B_0, the aggregates that reached the first right branch was 24% on the baseline

and 92% and 100% ($P < 0.001$, $P < 0.001$) after the application of MRN. For L-L and L-R MRN, the aggregates that reached left first branch were 76% on the baseline and 100% and 100% ($P = 0.022$, $P = 0.022$) after MRN.

Then, the phantom was rotated 90 degrees in the horizontal plane. We found that 8%, 88%, 0% 4% of particle aggregates were respectively directed toward the L-L, L-R, R-L and R-R branch ($n = 25$, see table 6-3) when no MRN was applied. The R-L branch has the worst outcome at baseline (0%). Thus, we tested this particular branch, which represents the most challenging branch to steer aggregates into, while the phantom was rotated 90 degrees, combining two unfavorable circumstances in order to see how our system will perform. With our MRN model and the main tube still perpendicular to B_0, the R-L pathway ($n = 25$) was able to reach a success rate of 80% ($P < 0.001$). Even at the right first branch that has 4% aggregate distribution without MRN, the branch got 92% ($P < 0.001$) MRN success rate.

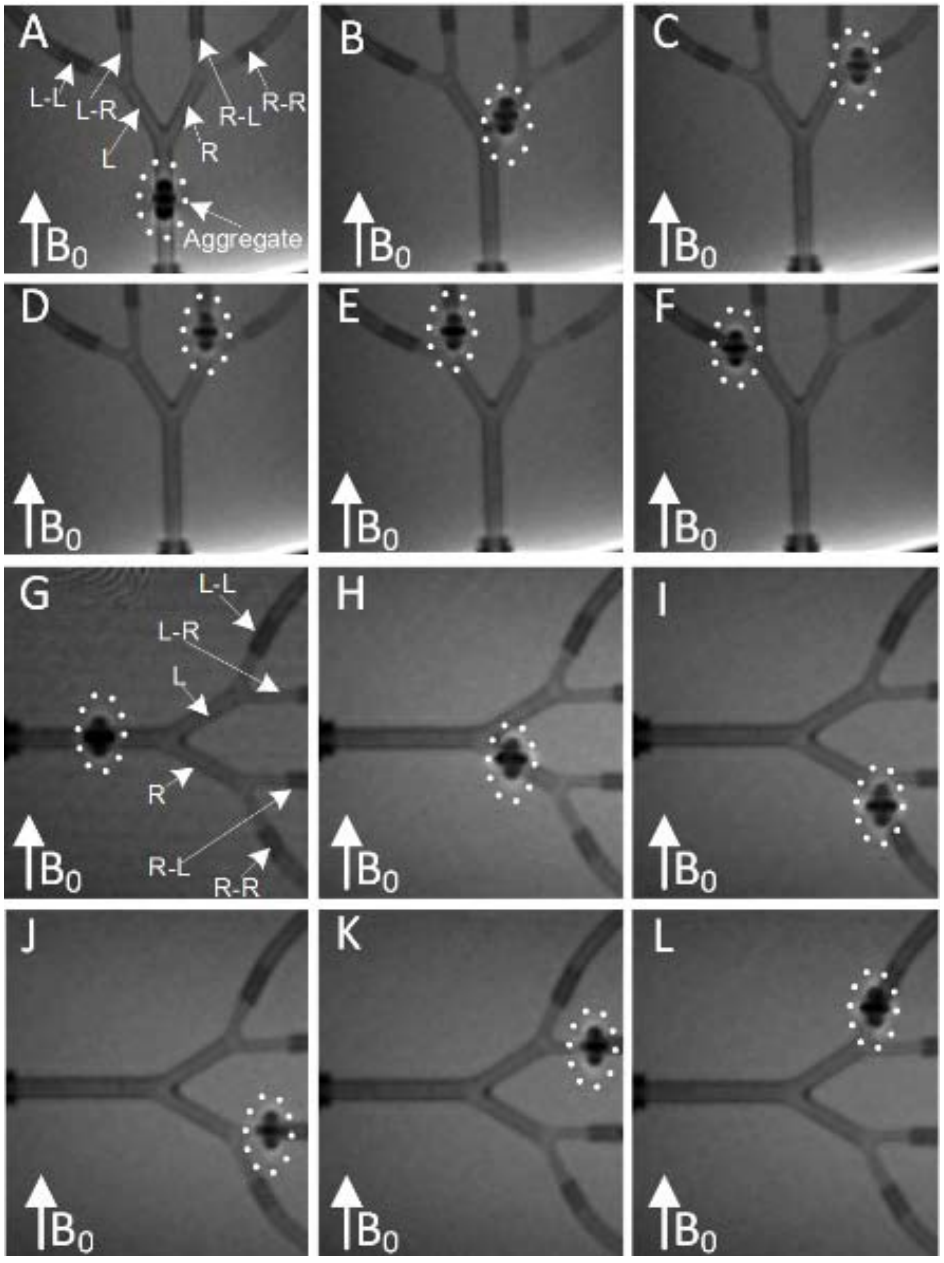

Figure 6-8: The particle aggregates were navigated into different second tube branches when the main tube is either parallel (A-F) or perpendicular (G-L) to B_0. The magnetic resonance imaging was taken from the coronal plane. Figure 6-8A-C and G–I show the particle aggregates reaching the main (A and G), first (B and H) and second (C and I) branches when carrying out R-R MRN. Figure 6-8B–E and I-L show that the particle aggregates had successfully reached four different second branches through MRN.

Table 6-3: Success rate of two-bifurcation MRN

MRN operation	First Branches	L-L Branch	L-R Branch	R-L Branch	R-R Branch
The main tube is parallel to B_0					
Baseline (n = 25) :	n/a	8%	68%	24%	0%
L-L navigation (n = 25):	100% (L)	84%	16%	0%	0%
L-R navigation (n = 25):	100% (L)	0%	100%	0%	0%
R-L navigation (n = 25):	96% (R)	0%	4%	84%	12%
R-R navigation (n = 25):	100% (R)	0%	0%	8%	92%
The main tube is perpendicular to B_0					
Baseline (n = 25) :	n/a	8%	88%	0%	4%
R-L navigation (n = 25):	92%* (R)	0%	8%*	80%	12%

*Note that: In n = 25, two particle aggregates were too big to pass through the first bifurcation. After closing MRN, the two aggregates were drifted into the L-R branch by using the high flow.

6.5 Conclusion and discussion

We have demonstrated the feasibility of MRN combining tracking and navigating sequences to navigate MDEB aggregates in a two-bifurcation phantom recreating realistic controlled pulsatile flow.

The navigated microparticles had a mean diameter of 200 µm which is just within the desired size range for liver embolization [112]. The microparticles were aggregated together to form bigger boluses, in order to reach a balance between high navigation efficiency and particle fluidity in vessels. We have determined a compromise in aggregate size to maximize steering force while being compatible with navigation in small branch division for different angulation to B_0. Moreover, the size of the aggregate is proportional to the number of MDEB and the desired amount of drug delivery for a single patient [192]. Finally, larger aggregates will minimize procedure time.

A theoretical model was proposed as a means to calculate the optimal aggregate length in order to ensure successful MRN. The model was based on the vessel size, the density and magnetization of particles, the magnetic steering gradients, the buoyancy, the gravity and the vessel direction relative to B_0. The appropriate aggregate size can be calculated before each bifurcation along the desired navigation pathway. The optimal aggregate length will be chosen so that we obtain high

MRN success rates while ensuring the maximum number of particles per aggregate is injected for decreasing the treatment duration.

The injector sends a trigger signal to start the MRN sequence automatically after an aggregate has been released into the phantom. When constant gradients are used to supply steering forces, there is a high rate of heat accumulation which may be harmful to the MRI. Thus, although the MRI gradient coils could theoretically supply a gradient up to 40 mT/m, we only used half of the maximum value which is 20 mT/m. The MRN sequence was only switched on after receiving the trigger signal from the injector to further decrease heat accumulation.

A simple MRN sequence consisting of tracking and navigating functions was proposed. The gradient time (T_g) required to steer the particle was determined by measuring the time required for particles to pass through the first branches. When doing the tracking and navigating experiments, the True FISP sequence, having both a high spatial resolution and a short acquisition time, performed excellently in its tracking tasks. Meanwhile, the quick imaging speed also decreases location errors often caused by a patient's breathing motions, making breath-holds unnecessary during MRN.

The success rate of aggregate navigation was always more than 80% through our proposed MRN methods. The rate can be further improved by increasing the magnetization of particles. However, the concentration of Fe_3O_4 is already 50 weight% in our particles. Higher concentrations lead to non-spherical and inhomogeneous particles, both in size and shape. Higher magnetization materials, such as FeCo, are possible but are in general not regarded as biocompatible [193].

Non-target embolization at the 2nd bifurcation has a less clinical consequence than that at the 1st bifurcation. We demonstrated that the MRN success rate is more than 92% at the 1st bifurcation in our paper. Although we got 100% MRN success rate in a single bifurcation phantom in the previous research [192], this value was obtained based on the condition of a continuous steering force during MRN. Our current MRN sequence can not supply the steering force during imaging. This may be the reason that decreases the success rate. An MRN sequence that is capable of simultaneously steering and imaging magnetic particles has been reported [188].

Although the phenomenon where the combination of vibrating and constant flow can increase MRN success rate has been reported [190], related parameters, such as the rate of the constant flow and the frequency of the vibrating flow, are different here. As explained above, the flow rate in the phantom was 0.6 ml/s, in order to mimic the flow obtained in previous in vivo experiments [192]. During these in vivo experiments, it was possible in a porcine liver model to control the flow in the hepatic artery with an occlusion balloon and obtain T_s compatible with MRN with a similar injection rate. The vibrator was set to 1 Hz with an amplitude of 0.4 ml, to create a stop and go motion of MDEB aggregates. Here, the reason for choosing the frequency of 1 Hz was based on the normal human heart rate ranging from 60 to 100 beats a minute.

To be compatible with two-bifurcation navigation and different angulation to B_0, we decreased the size of the aggregates (ranging from 1.6 to 3.2 mm in previous publications) [191]. The dimensions of the counting area of the injector were decreased to 1.2 mm and the chosen resistance was 57 kΩ. The injector exhibited good performances in its task of forming consistently our desired aggregate sizes.

Even though the MRI could obtain the coordinate position of particles [188], in our experiments, after each particle steering, we visually checked their position from the control room of the MRI using the true FISP sequence. If the particle aggregate was located in the first branch division, the gradient direction was set manually. This would be difficult and complex, and prone to human error for a whole MDEB TACE procedure requiring a high number of injections. Thus, the MRN software needs to be optimized and automatized. A complete control-loop software is required to be able to change the gradient direction automatically based on the position feedback of MDEB aggregates on each MR image. The tracking and steering sequences will be integrated into one to further decrease the switching time between the two individual sequences.

In this study, we first demonstrated the feasibility of integrating a particle injection system with MRN sequences to achieve two-level bifurcation MRN using 1.2 mm long aggregates made of 200 µm MDEBs. The flow in the phantom consisted of vibrating and constant flow, which had been demonstrated to increase the control of MDEB aggregate motion. In order to achieve a high success rate in our experimentations, a theoretical model was proposed to determine the most appropriate size of each particle aggregate for MRN. Then, the motion characteristics of all particles had been investigated in the phantom, while the True FISP sequence had been used to track and locate those

particles. The duty cycle of the steering gradient and true FISP sequences were then arranged based on the kinetic characteristics of the particles and the measured imaging parameters. After integrating all parts of the MRN system, the success rate of MRN was always more than 92% and 80% at the 1st and 2nd bifurcations. We are now planning to evaluate the feasibility of this technique in vivo.

ACKNOWLEDGEMENTS

This work was supported by grants from the Natural Sciences and Engineering Research Council of Canada (NSERC), Operating Grant - CHRP (CIHR Partnered) (CHRP 478474-15) and Canadian Institutes of Health Research (CIHR), Operating Grant - CHRP (NSERC Partnered) (CPG-140179).

.

CHAPTER 7 GENERAL DISCUSSION

HCC was the fourth most common cause of cancer-related deaths last year based on the data collected by the world health organization. The traditional TACE technology is a therapy method of choices but it is difficult to achieve a high targeting efficiency. The MRN technique can use a clinical MRI system to track and navigate magnetic drug-eluting beads to targeted positions through the patients' vascular networks [91-93]. However, the gradients supplied by clinical MRI systems are typically limited to about 40 mT/m. Considering the fact that the blood velocity in hepatic arteries can be tens of centimeters per second, under such a low gradient value (40 mT/m), navigating MDEBs composed of degradable materials, anti-tumor drugs and magnetic nanoparticles, is difficult because of limited magnetic forces. To exactly understand the obstacles of successful MRN in the clinical MRI settings, our proposed MRN technology system is divided into 5 steps below: particle design, flow control, the formation of MDEB aggregates with controllable sizes, MRN software, and integration of all the individual systems to achieve successful MRN. The problems encountered and anticipated at each step were solved accordingly.

7.1 Particle design

For MRN, MDEBs are generally composed of three components: base materials, anti-tumor drugs and superparamagnetic nanoparticles. MDEBs need to satisfy the conditions below: 1) The size of MEDBs must be between 100 and 300 μm in order to meet the criteria for both optimal tumor penetration and lowest rates of liver complications [110, 111]; 2) The used materials (base materials, anti-tumor drugs and superparamagnetic nano-particles) must be bio-compatible and/or degradable; 3) The sizes of the embedded nanoparticles typically range from 5 to 20 nm in order to exhibit superparamagnetic properties while they can, at the same time, be safely phagocytosed in the body [103, 104].

Before my research, magnetic nanoparticles were successfully encapsulated into a biodegradable material (PLGA) to obtain microparticles (MDEBs) for MRN [105]. Despite the base material being bio-compatible and degradable material, the encapsulated nanoparticles were FeCo nanoparticles, a bio-toxic material. Furthermore, the size of the microparticles (58 μm) and the encapsulated nanoparticles (182 nm) were both not within the desired ranges (100-300 μm and 5-20 nm) mentioned above.

In my preliminary study (Appendix A), microparticles were fabricated using the gas-liquid flow focusing approach. The mean diameter of these microparticles was 200 μm, matching the size requirement of TACE for HCC therapy. The base material was alginate which is biocompatible and biodegradable [194]. The encapsulated magnetic nanoparticles (Fe_3O_4) were superparamagnetic and were not bio-toxic. However, the size of these nanoparticles (200 nm) was bigger than our desired value (5-20 nm). The saturation magnetization of the microparticles was 1.36 emu/g, a value that would be very difficult to further increase because the ferrofluid brought from Chemicell GmbH company has a limited particle concentration. The microparticles were used in the *in vitro* researches in chapter 3.

Then, with the help of Prof. Urs´ lab, another type of microparticles was made [106]. The size was still about 200 μm and the base material used was PLGA. Superparamagnetic bio-compatible iron oxide (Fe_3O_4) nanoparticles with a diameter of 12 ± 3.6 nm lead to a saturation magnetization reaching up to 30 emu/g. Thus, these new microparticles satisfy our requirements for MRN. Although the anti-tumor drugs were not encapsulated, the possibility to load PLGA-based magnetic microparticles with doxorubicin has been previously demonstrated [17]. This type of microparticles was used in the researches in chapters 4 and 5.

Table 7-1 Parameters of the existed particles used for MRN

Research team	Base material		Anti-tumor drug	Superparamagnetic nanoparticles		The size of the obtained microparticle (MDEB)
	Bio-compatible	Degradable		Size	Bio-compatible	
Pouponneau et al. 2011 [17]	Yes (PLGA)	Yes	Yes	182 nm	No (FeCo)	58 μm
Li et al. 2017 [190]	Yes (Alginate)	Yes	No	200 nm	Yes (Fe_3O_4)	200 μm
Nosrati et al. 2018 [106]	Yes (PLGA)	Yes	No	12 ± 3.6 nm	Yes (Fe_3O_4)	200 μm

7.2 Flow control

For any clinical MRI system, the amplitude of gradients is limited to 40 mT/m. In [195], the blood speed in the hepatic artery was measured at 57 cm/s such that the blood must slow down to allow the magnetic steering force to have more time to bring the particles into the right side of a bifurcation. Different types of methods or tools can be used to block or reduce the blood speed [122, 123, 196]. Already, in [17], a balloon catheter had been installed in order to significantly slow the flow in the common hepatic artery.

In Appendix C and [129], we demonstrated the possibility of using a balloon catheter to precisely control the blood flow in the proper hepatic artery through the *in vivo* experiments. The method involved the hepatic artery being fully stopped by inflating the balloon of a catheter, followed by the precise-speed injection of the saline solution.

Then, to check whether the constant laminar flow is enough to ensure a high MRN success rate, in chapter 4, I compared the phenomena of particle MRN with the constant flow to the other one with the oscillating flow. The experiments revealed that 1) The low-velocity constant flow can not increase the success rate of MRN, and 2) The oscillating flow composed of a vibrating flow and a constant flow can make the drifting speed of the particles low and stable, allowing a high success rate for MRN.

In [129] or Appendix B, we reproduced the flow speed obtained in the *in vivo* experiments. Then, the oscillating flow with an amplitude of 0.4 mL and a frequency of 1 Hz was added. After applying a corresponding gradient (20 mT/m), a 100% success rate was obtained when navigating MDEB aggregates across the first bifurcation of a glass phantom mimicking physiological conditions, no matter the orientation of the phantom in regard to B_0.

7.3 Formation of MDEB aggregates with controllable sizes

Although previous researches studied the phenomenon of magnetic aggregation and investigated the importance of using particle aggregates in MRN. No reports have reported an injector capable of controlling the aggregate size, as well as the particle number in each aggregate. In 2016, an injector prototype composed of a bead capture and a bead detection system was proposed by Alexandre Bigot et al. [116]. There are two limitations for the bead capture subsystem: 1) There are no necessary sensors capable of controlling the particle number, as well as aggregate sizes; 2)

The navigated beads were made of chrome steel, allowing low-power coils to trap such a high-magnetization material. When I designed the new injector, infrared sensors were used to solve the first problem. A small cylindrical neodymium magnet driven by an electromagnet-based piston to control the trap and release of MDEBs was used, which made it possible to avoid overheating problems induced by the electromagnetic trap.

My proposed injector is not solely limited to MRN. DFN is another technique that can be brought into play to navigate MDEBs [89]. This technique distorts the uniform magnetic field of a clinical MRI scanner using soft ferromagnetic cores placed at strategic locations. With this method, the continuous injection of particles is feasible because the successive gradients are static and spatially distributed. However, for DFN, the distorted magnetic field induced by the ferromagnetic cores could be a concern if real-time MRI is required [197]. To cope with the distortions when performing an imaging sequence, a method was developed to move the ferromagnetic cores away from their locations and move them back after imaging [197]. Thus, the injection of particles is only suitable during the navigation phase in DFN, resulting in a similar pulsed-bolus injection. The ability to have a real-time estimation of particle numbers is also a real advantage in selective catheterization under MR guidance [171, 178].

7.4 MRN software

The MRN software needs to have two basic abilities including steering and tracking particle aggregates.

The steering force on each particle was supplied by the magnetic gradient coils of the MRI system. Thus, the maximum amplitude of gradients is limited to about 40 mT/m. The methods that can be used to improve gradient force efficiency are restricted to two devices: space-limited coils [117] or high-cost ultrahigh gradient MRI scanners [118]. Despite space and cost problems, when we did the one-bifurcation MRN experiments in Appendix B, the amplifier coil temperature increased from 20 up to a maximum of 50°C even if the gradient was only 20 mT/m. Thus, although the maximum amplitude of gradients can reach up to 40 mT/m, a higher gradient magnitude will induce a faster and higher heating rate. Hence, in chapter 6, a 20 mT/m gradient was used.

To track particle aggregates formed by my proposed injector, True FISP sequences were used. I confirmed their performances with the imaging speed and imaging resolutions. The sequences have

not gotten coordinate positions of the aggregates in the experiments. A complete control-loop MRN sequence software needs to change the gradient direction automatically based on the position feedback of the MDEB aggregates. In [22], after getting the images through True FISP sequence, particles were localized based on the "Center Of Gravity" of the artifacts [198, 199].

We have demonstrated that: the MRN success rate is 100% when using continued gradient forces in Appendix B, but the rate decreased to 92% and 80% after adding the tracking sequence (True FISP) which can not supply the steering force. Simultaneously steering and imaging magnetic particles is a good choice to further increase the MRN success rate [188]. Therefore, a new MRN sequence, capable of simultaneously steering and localizing of magnetic particles, can be expected in the future.

7.5 Integration of all parts to achieve successful MRN

Although I have designed the injector that is capable of controlling aggregate sizes, a theoretical model is still required as a means to calculate the optimal aggregate length in order to ensure successful MRN. Thus, a model relative to the vessel size, the density and magnetization of particles, the magnetic steering gradients, the buoyancy, the gravity, and the vessel direction relative to B_0 was proposed.

After an aggregate is released from the catheter, a signal is required to be sent out to trigger the MRN sequence. Thus, in [116], a bead detection system consisting of two identical coils-one emitters and one receiver-was designed. When a bead entered the space between two coils, the natural resonance frequency changed and thus the output of the receiver shifted. I did not use this design. The reasons are as follows: 1) The design relies on micromachining technology to fabricate two identical coils at the tip of the catheter, which will increase costs; 2) The balloon catheter will be used to preciously control blood flow, leaving limited spaces for the two coils. In my design, a 2-V, 100-ms pulse rectangular trigger signal generated by a trigger generator was sent to the scanner. After a bolus was released from the injector, the time required to arrive at the phantom was measured. The delay time was set in the trigger generator. Once the signal is received from the injector, after the delay time, the generator will send out the corresponding trigger signal to start the MRN sequence. This is an easy and low-cost way in order to synchronize particle injections and MRN. This method reduced the work duty of the MRN software such that the heating accumulation reduced.

However, all MRN experiments were done in a 2D space. It is necessary to test our MRN system the 3D MRN before implementing *in vivo* experiments. In Appendix B, I theoretically and practically demonstrated that if we want to overcome the gravity of MDEBs, the steering gradient needs to be higher than approximately 70 mT/m, which is almost 2 times bigger than the maximum value of the normal clinical MRI system. To further increase the concentration of Fe_3O_4 is difficult because the current concentration value has reached about 50%-60%. Instead of overcoming the gravity to achieve 3D navigation, we can take advantage of gravitational forces to develop a new MRN strategy using both the gravity and magnetic steering forces to guide the particles.

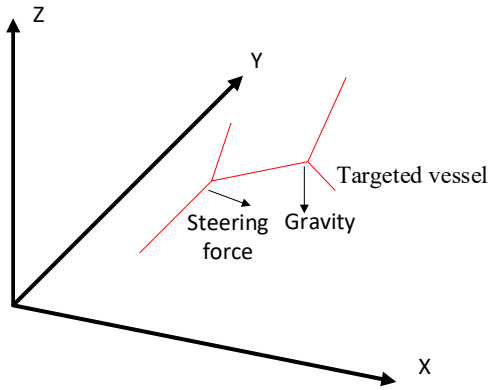

Figure 7-1: Schematic diagram of the combination of the steering force and the gravity to achieve 3D MRN.

CHAPTER 8 CONCLUSION AND RECOMMENDATIONS

8.1 Conclusion

This thesis is aimed at solving the unsolved problems of the validation of magnetic resonance navigation (MRN) in multi-bifurcation phantoms in clinical MR scanners. The problems mainly include: 1) How to ensure a high success rate when the magnetic gradients of clinical MRI systems can not be higher than 40 mT/m; 2) How to control the aggregate sizes, as well as the particle number for each injection; 3) How to determine the aggregate size for different vessel dimensions; 4) How to integrate all the individual systems together to achieve successful MRN.

Initially, the possibility of controlling blood flow in the hepatic artery was studied through the *in vivo* experiment (Appendix B). A balloon catheter was inserted into the hepatic artery to block or decrease the blood flow, followed by injections of a saline solution through the catheter. Then, the flow velocity in vessels was measured through the 2D MRI phase-contrast cine sequence. After comparing the measured flow velocity with the injected one, we demonstrated the possibility of controlling blood flow (constant flow) in hepatic arteries. However, this research did not answer the question of how to form other types of flow patterns in vessels.

Subsequently, after making the proper sized particles (Appendix A), the MRN phenomenon within a context of constant flow was researched. I found that, under a 40 mT/m gradient, successful MRN can not be achieved when using a constant flow. Then, the oscillating flow, composed of a constant flow and a vibrating flow, was tested in the MRN operations. I experimentally demonstrated that the proposed flow pattern (oscillating flow) can increase the success rate of MRN (chapter 4).

Thereafter, to control the size of each aggregate, an infrared emitter and a receiver were used. The principle is that, the light reaching the receiver diminishes as the opaque magnetic particles accumulate in the counting chamber which is in-between the emitter and receiver, resulting in a higher ohmic resistance detected by the circuitry since fewer photons are now reaching the receiver. My experiments showed that the principle can still be applicable even in the 1.5 T or 3 T MRI system. The injector system (chapter 5) was divided into two main functional parts: the controller, which controls the capture and release of magnetic particles, and the MRI-compatible actuator, which sends out the measured signal for monitoring the particle number while acting as a

mechanical actuator for particle aggregation and release. It means that, I can set a resistance value in the controller, and a particle aggregate will be atomically released when the receiver resistance reaches the set value. The relationship between the receiver resistance and the aggregate size was experimentally measured. This allows us to define particle numbers and aggregate sizes per injection by simply setting the resistance value in the controller. This injector is designed for the MRN technique. However, it can also be used in other MRI-based targeted therapy methods, such as the DFN technique.

I have integrated the particle injection system with MRN to test targeted embolization in a two-level bifurcation phantom (chapter 6). In this section, a theoretical model was proposed to calculate the optimal aggregate length in order to ensure successful MRN. The model is based on the force balance of particles after being applied to the magnetic force. The parameters include the vessel size, the density and magnetization of particles, the magnetic steering gradients, the buoyancy, the gravity, and the vessel direction relative to B_0. After using the model to calculate the appropriate aggregate size for successful MRN, an MRN software was proposed and researched. I experimentally demonstrated that the True FISP sequences have both fast imaging speeds and high resolutions. Thus, these sequences were chosen as the tracking segments in the MRN software. Then, the duty cycle of the steering gradient and True FISP sequences were arranged based on the kinetic characteristics of the particles and the measured imaging parameters. In a two-level bifurcation phantom, I demonstrated that the success rate of MRN was always greater than 92% and 80% at the 1^{st} and 2^{nd} bifurcations. However, the MRN software proposed in this section is not capable of getting the coordinates of particle aggregates. It means that this software can not change the gradient direction automatically based on the position feedback of particle aggregates on each MR image.

8.2 Recommendations

This thesis presents an original contribution to our understanding of MRN in the clinical MRI system. At the same time, new questions are generated and need to be explored in future studies, which include:

• In-vitro and in-vivo validation of vibrating flow with a dual-lumen balloon catheter, and optimization of MDEB aggregate propulsion

Theoretically, decreasing the flow velocity in vessels can increase the MRN success rate. In Appendix B, we have demonstrated the possibility of precisely controlling the flow rate in hepatic arteries by using a balloon catheter. However, in chapter 4, I found that the low-velocity flow can not increase the MRN success rate. How to form the flow pattern, proposed in chapter 4, in vessels is an unsolved problem. Here, the dual-lumen balloon catheters are a possible choice to form the oscillating flow in vessels, by inflating and deflating the balloon.

• Understand rheological modification during embolization

The peripheral resistance will progressively increase when MDEBs are embolized in segmental arteries. Thus, the flow to the embolized segments will decrease. We need to adapt the flow in vessels according to this flow variation during the embolization procedure.

• Development of a closed loop MRN software

A new MRN software needs to be developed and has to capable of measuring the flow speed, getting the coordinate positions of the navigated aggregates, and changing the gradient direction automatically based on the positions of the aggregates.

• Combination of gravity and steering forces to improve the success rate of MRN (Appendix C)

We can take advantage of gravitational forces to develop a new MRN strategy using both the gravity and magnetic steering forces. In some cases, maybe we can simply rotate the patient's body to take advantage of gravitational forces.

• Research of the degradation rate of MDEBs

An important reason for this research is to have a feasibility assessment of using high magnetization materials, such as $Fe_{55}Co_{45}$ (about 270 emu/g) instead of Fe_3O_4 nanoparticles (about 75.3 emu/g), in MDEBs. Although the cobalt has shown to be toxic for human bodies, the delayed degradation speed can make the nanoparticles release slow, thus decreasing systemic toxicity levels induced by cobalt materials.

• Experimental Study: In-vivo feasibility/ efficacy assessment of the MRN technology

We need to prove the clinical feasibility and efficacy of the MRN technique.

• Possibility of using the proposed injector in other MRI-based targeted methods such as DFN technique

REFERENCES

[1] P. Bertuccio, F. Turati, G. Carioli, T. Rodriguez, C. La Vecchia, M. Malvezzi, and E. Negri, "Global trends and predictions in hepatocellular carcinoma mortality," *Journal of Hepatology,* vol. 67, no. 2, pp. 302-309, Aug 2017.

[2] L. P. Waller, V. Deshpande, and N. Pyrsopoulos, "Hepatocellular carcinoma: A comprehensive review," *World J Hepatol,* vol. 7, no. 26, pp. 2648-63, Nov 18 2015.

[3] S. Ma, "Biology and clinical implications of CD133(+) liver cancer stem cells," *Experimental Cell Research,* vol. 319, no. 2, pp. 126-132, Jan 15 2013.

[4] Z. Wang, G. Zhang, J. Wu, and M. Jia, "Adjuvant therapy for hepatocellular carcinoma: current situation and prospect," *Drug Discov Ther,* vol. 7, no. 4, pp. 137-43, Aug 2013.

[5] C. R. de Lope, S. Tremosini, A. Forner, M. Reig, and J. Bruix, "Management of HCC," *J Hepatol,* vol. 56 Suppl 1, pp. S75-87, 2012.

[6] A. F. H. Lum, M. A. Borden, P. A. Dayton, D. E. Kruse, S. I. Simon, and K. W. Ferrara, "Ultrasound radiation force enables targeted deposition of model drug carriers loaded on microbubbles," *Journal of Controlled Release,* vol. 111, no. 1-2, pp. 128-134, Mar 10 2006.

[7] E. Wagner, "Programmed drug delivery: nanosystems for tumor targeting," *Expert Opin Biol Ther,* Review vol. 7, no. 5, pp. 587-93, May 2007.

[8] A. K. Miri and F. G. Mitri, "Acoustic Radiation Force on a Spherical Contrast Agent Shell near a Vessel Porous Wall - Theory," *Ultrasound in Medicine and Biology,* vol. 37, no. 2, pp. 301-311, Feb 2011.

[9] S. Martel, J. B. Mathieu, O. Felfoul, A. Chanu, E. Aboussouan, S. Tamaz, and P. Pouponneau, "Automatic navigation of an untethered device in the artery of a living animal using a conventional clinical magnetic resonance imaging system," *Applied Physics Letters,* vol. 90, no. 11, Mar 12 2007.

[10] P. K. Selbo, A. Høgset, L. Prasmickaite, and K. Berg, "Photochemical internalisation: a novel drug delivery system," *Tumor biology,* vol. 23, no. 2, pp. 103-112, 2002.

[11] E. Chang, S. Chalikonda, J. Friedl, H. Xu, G. Q. Phan, F. M. Marincola, H. R. Alexander, and D. L. Bartlett, "Targeting vaccinia to solid tumors with local hyperthermia," *Human gene therapy,* vol. 16, no. 4, pp. 435-444, 2005.

[12] C. Chouly, D. Pouliquen, I. Lucet, J. J. Jeune, and P. Jallet, "Development of superparamagnetic nanoparticles for MRI: Effect of particle size, charge and surface nature on biodistribution," *Journal of Microencapsulation,* vol. 13, no. 3, pp. 245-255, May-Jun 1996.

[13] O. Clement, N. Siauve, C. A. Cuenod, V. Vuillemin-Bodaghi, I. Leconte, and U. Frija, "Mechanisms of action of liver contrast agents: Impact for clinical use," *Journal of Computer Assisted Tomography,* vol. 23, pp. S45-S52, Nov 1999.

[14] J. J. Abbott, K. E. Peyer, M. C. Lagomarsino, L. Zhang, L. Dong, I. K. Kaliakatsos, B. J. Nelson, "How should microrobots swim?," *The Int. J. Robot Res,* vol. 28, no. 11-12, pp. 1434-1447, 2009.

[15] P. Vartholomeos, M. Fruchard, A. Ferreira, and C. Mavroidis, "MRI-Guided Nanorobotic Systems for Therapeutic and Diagnostic Applications," *Annual Review of Biomedical Engineering, Vol 13,* vol. 13, pp. 157-184, 2011.

[16] G. Vidal, S. Martel, "Measuring the magnetophoretic characteristics of magnetic agents for targeted diagnostic or therapeutic interventions in the vascular network," *Journal of Micro-Bio Robotics,* vol. 8, no. 2, pp. 65-71, 2013.

[17] P. Pouponneau, J. C. Leroux, G. Soulez, L. Gaboury, and S. Martel, "Co-encapsulation of magnetic nanoparticles and doxorubicin into biodegradable microcarriers for deep tissue targeting by vascular MRI navigation," *Biomaterials,* Research Support, Non-U.S. Gov't vol. 32, no. 13, pp. 3481-6, May 2011.

[18] S. Martel, J. B. Mathieu, O. Felfoul, A. Chanu, E. Aboussouan, S. Tamaz, and P. Pouponneau, "Automatic navigation of an untethered device in the artery of a living animal using a conventional clinical magnetic resonance imaging system," *Applied Physics Letters,* vol. 90, no. 11, p. 114105, Mar 12 2007.

[19] N. Olamaei, F. Cheriet, and S. Martel, "Magnetic resonance imaging of microvessels using iron-oxide nanoparticles," *Journal of Applied Physics,* vol. 113, no. 12, Mar 28 2013.

[20] K. S. Im, K. Fezzaa, Y. J. Wang, X. Liu, J. Wang, and M. C. Lai, "Particle tracking velocimetry using fast x-ray phase-contrast imaging," *Applied Physics Letters,* vol. 90, no. 9, Feb 26 2007.

[21] M. A. Rube, A. B. Holbrook, B. F. Cox, J. G. Houston, and A. Melzer, "Wireless MR tracking of interventional devices using phase-field dithering and projection reconstruction," *Magnetic Resonance Imaging,* vol. 32, no. 6, pp. 693-701, Jul 2014.

[22] N. Olamaei, F. Cheriet, S. Deschenes, and S. Martel, "Dynamic tracking of magnetic nanoparticles for mapping microvascular networks using a clinical 1.5 T magnetic resonance scanner," *Applied Physics Letters,* vol. 104, no. 21, p. 213703, May 26 2014.

[23] E. A. F. T. S. O. T. Liver, "EASL–EORTC clinical practice guidelines: management of hepatocellular carcinoma," *Journal of hepatology,* vol. 56, no. 4, pp. 908-943, 2012.

[24] M. A. Gomes, D. G. Priolli, J. G. Tralhão, and M. F. Botelho, "Hepatocellular carcinoma: epidemiology, biology, diagnosis, and therapies," *Revista da Associação Médica Brasileira,* vol. 59, no. 5, pp. 514-524, 2013.

[25] P. Ferenci, M. Fried, D. Labrecque, J. Bruix, M. Sherman, M. Omata, J. Heathcote, T. Piratsivuth, M. Kew, and J. A. Otegbayo, "World gastroenterology organisation global guideline. Hepatocellular carcinoma (hcc): A global perspective," *J gastrointestin liver dis,* vol. 19, no. 3, pp. 311-317, 2010.

[26] D. M. Parkin, F. Bray, J. Ferlay, and P. Pisani, "Global cancer statistics, 2002," *CA: a cancer journal for clinicians,* vol. 55, no. 2, pp. 74-108, 2005.

[27] K. M. Elsayes, J. C. Hooker, M. M. Agrons, A. Z. Kielar, A. Tang, K. J. Fowler, V. Chernyak, M. R. Bashir, Y. Kono, and R. K. Do, "2017 version of LI-RADS for CT and MR imaging: an update," *Radiographics,* vol. 37, no. 7, pp. 1994-2017, 2017.

[28] J. K. Heimbach, L. M. Kulik, R. S. Finn, C. B. Sirlin, M. M. Abecassis, L. R. Roberts, A. X. Zhu, M. H. Murad, and J. A. Marrero, "AASLD guidelines for the treatment of hepatocellular carcinoma," *Hepatology,* vol. 67, no. 1, pp. 358-380, 2018.

[29] P. Stefaniuk, J. Cianciara, and A. Wiercinska-Drapalo, "Present and future possibilities for early diagnosis of hepatocellular carcinoma," *World journal of gastroenterology: WJG,* vol. 16, no. 4, p. 418, 2010.

[30] A. Doyle and M. Sherman, "Liver Biopsy for Hepatocellular Carcinoma (HCC): Should this be a Routine?," *Current Hepatology Reports,* vol. 16, no. 1, pp. 46-50, 2017.

[31] E. Caturelli, L. Solmi, M. Anti, S. Fusilli, P. Roselli, A. Andriulli, F. Fornari, C. D. V. Blanco, and I. De Sio, "Ultrasound guided fine needle biopsy of early hepatocellular carcinoma complicating liver cirrhosis: a multicentre study," *Gut,* vol. 53, no. 9, pp. 1356-1362, 2004.

[32] A. von Herbay, J. Westendorff, and M. Gregor, "Contrast-enhanced ultrasound with SonoVue: Differentiation between benign and malignant focal liver lesions in 317 patients," *Journal of Clinical Ultrasound,* vol. 38, no. 1, pp. 1-9, 2010.

[33] R. Dhanasekaran, A. Limaye, and R. Cabrera, "Hepatocellular carcinoma: current trends in worldwide epidemiology, risk factors, diagnosis, and therapeutics," *Hepatic medicine: evidence and research,* vol. 4, p. 19, 2012.

[34] S. H. Kim, B. I. Choi, J. Y. Lee, S. J. Kim, Y. H. So, H. W. Eun, J. M. Lee, and J. K. Han, "Diagnostic accuracy of multi-/single-detector row CT and contrast-enhanced MRI in the detection of hepatocellular carcinomas meeting the milan criteria before liver transplantation," *Intervirology,* vol. 51, no. Suppl. 1, pp. 52-60, 2008.

[35] Y. R. Choi, J. W. Chung, M. H. Yu, M. Lee, and J. H. Kim, "Diagnostic accuracy of contrast-enhanced dynamic CT for small hypervascular hepatocellular carcinoma and assessment of dynamic enhancement patterns: Results of two-year follow-up using cone-beam CT hepatic arteriography," *PloS one,* vol. 13, no. 9, p. e0203940, 2018.

[36] J. M. Willatt, H. K. Hussain, S. Adusumilli, and J. A. Marrero, "MR Imaging of hepatocellular carcinoma in the cirrhotic liver: challenges and controversies," *Radiology,* vol. 247, no. 2, pp. 311-330, 2008.

[37] G. A. Krinsky, V. S. Lee, N. D. Theise, J. C. Weinreb, G. R. Morgan, T. Diflo, D. John, and L. W. Teperman, "Transplantation for hepatocellular carcinoma and cirrhosis: sensitivity of magnetic resonance imaging," *Liver transplantation,* vol. 8, no. 12, pp. 1156-1164, 2002.

[38] S. K. Olsen, R. S. Brown Jr, and A. B. Siegel, "Hepatocellular carcinoma: review of current treatment with a focus on targeted molecular therapies," *Therapeutic advances in gastroenterology,* vol. 3, no. 1, pp. 55-66, 2010.

[39] J. M. Llovet, C. Brú, and J. Bruix, "Prognosis of hepatocellular carcinoma: the BCLC staging classification," in *Seminars in liver disease*, 1999, vol. 19, no. 03, pp. 329-338: © 1999 by Thieme Medical Publishers, Inc.

[40] V. Mazzaferro, E. Regalia, R. Doci, S. Andreola, A. Pulvirenti, F. Bozzetti, F. Montalto, M. Ammatuna, A. Morabito, and L. Gennari, "Liver transplantation for the treatment of small hepatocellular carcinomas in patients with cirrhosis," *New England Journal of Medicine,* vol. 334, no. 11, pp. 693-700, 1996.

[41] G. Li, G. Cai, D. Li, and W. Yin, "MicroRNAs and liver disease: viral hepatitis, liver fibrosis and hepatocellular carcinoma," *Postgraduate medical journal,* vol. 90, no. 1060, pp. 106-112, 2014.

[42] N. Bhardwaj, M. T. P. R. Perera, and M. A. Silva, "Current Treatment Approaches to HCC with a Special Consideration to Transplantation," *Journal of Transplantation,* 2016.

[43] Y. X. J. Wang, T. De Baere, J. M. Idee, and S. Ballet, "Transcatheter embolization therapy in liver cancer: an update of clinical evidences," *Chinese Journal of Cancer Research,* vol. 27, no. 2, pp. 96-121, Apr 2015.

[44] R. C. Gaba, R. P. Lokken, R. M. Hickey, A. J. Lipnik, R. J. Lewandowski, R. Salem, D. B. Brown, T. G. Walker, J. E. Silberzweig, and M. O. Baerlocher, "Quality improvement guidelines for transarterial chemoembolization and embolization of hepatic malignancy," *Journal of Vascular and Interventional Radiology,* vol. 28, no. 9, pp. 1210-1223. e3, 2017.

[45] P. Wiggermann, D. Sieron, C. Brosche, T. Brauer, F. Scheer, I. Platzek, W. Wawrzynek, and C. Stroszczynski, "Transarterial Chemoembolization of Child-A hepatocellular carcinoma: drug-eluting bead TACE (DEB TACE) vs. TACE with cisplatin/lipiodol (cTACE)," *Med Sci Monit,* vol. 17, no. 4, pp. CR189-95, Apr 2011.

[46] E. Liapi, C. C. Georgiades, K. Hong, and J.-F. H. Geschwind, "Transcatheter arterial chemoembolization: current technique and future promise," *Techniques in vascular and interventional radiology,* vol. 10, no. 1, pp. 2-11, 2007.

[47] L. Marelli, R. Stigliano, C. Triantos, M. Senzolo, E. Cholongitas, N. Davies, J. Tibballs, T. Meyer, D. W. Patch, and A. K. Burroughs, "Transarterial therapy for hepatocellular carcinoma:

which technique is more effective? A systematic review of cohort and randomized studies," *Cardiovascular and interventional radiology,* vol. 30, no. 1, p. 6, 2007.

[48] A. O. Chan, M. F. Yuen, C. K. Hui, W. K. Tso, and C. L. Lai, "A prospective study regarding the complications of transcatheter intraarterial lipiodol chemoembolization in patients with hepatocellular carcinoma," *Cancer,* vol. 94, no. 6, pp. 1747-1752, Mar 15 2002.

[49] K. Tam, "The roles of doxorubicin in hepatocellular carcinoma," *ADMET and DMPK,* vol. 1, no. 3, pp. 29-44, 2013.

[50] J. Kettenbach, A. Stadler, I. v. Katzler, R. Schernthaner, M. Blum, J. Lammer, and T. Rand, "Drug-loaded microspheres for the treatment of liver cancer: review of current results," *Cardiovascular and interventional radiology,* vol. 31, no. 3, pp. 468-476, 2008.

[51] T. Sato, "Locoregional immuno (bio) therapy for liver metastases," in *Seminars in oncology*, 2002, vol. 29, no. 2, pp. 160-167: Elsevier.

[52] K. Y. Tam, K. C.-F. Leung, and Y.-X. J. Wang, "Chemoembolization agents for cancer treatment," *European Journal of Pharmaceutical Sciences,* vol. 44, no. 1-2, pp. 1-10, 2011.

[53] Z. Kan and D. C. Madoff, "Liver anatomy: microcirculation of the liver," in *Seminars in interventional radiology*, 2008, vol. 25, no. 2, p. 77: Thieme Medical Publishers.

[54] T. Matsumoto, T. Yamagami, T. Kato, T. Hirota, R. Yoshimatsu, T. Masunami, and T. Nishimura, "The effectiveness of lymphangiography as a treatment method for various chyle leakages," *The British journal of radiology,* vol. 82, no. 976, pp. 286-290, 2009.

[55] R. R. Taylor, Y. Tang, M. V. Gonzalez, P. W. Stratford, and A. L. Lewis, "Irinotecan drug eluting beads for use in chemoembolization: in vitro and in vivo evaluation of drug release properties," *Eur J Pharm Sci,* vol. 30, no. 1, pp. 7-14, Jan 2007.

[56] M. Varela, M. I. Real, M. Burrel, A. Forner, M. Sala, M. Brunet, C. Ayuso, L. Castells, X. Montana, J. M. Llovet, and J. Bruix, "Chemoembolization of hepatocellular carcinoma with drug eluting beads: efficacy and doxorubicin pharmacokinetics," *J Hepatol,* Clinical Trial Research Support, Non-U.S. Gov't vol. 46, no. 3, pp. 474-81, Mar 2007.

[57] P. P. Rao, F. Pascale, A. Seck, A. Auperin, L. Drouard-Troalen, F. Deschamps, C. Teriitheau, A. Paci, A. Denys, P. Bize, and T. de Baere, "Irinotecan loaded in eluting beads:

preclinical assessment in a rabbit VX2 liver tumor model," *Cardiovasc Intervent Radiol,* Research Support, Non-U.S. Gov't vol. 35, no. 6, pp. 1448-59, Dec 2012.

[58] O. Jordan, A. Denys, T. De Baere, N. Boulens, and E. Doelker, "Comparative study of chemoembolization loadable beads: in vitro drug release and physical properties of DC bead and hepasphere loaded with doxorubicin and irinotecan," *J Vasc Interv Radiol,* vol. 21, no. 7, pp. 1084-90, Jul 2010.

[59] K. Malagari, "Drug-eluting particles in the treatment of HCC: chemoembolization with doxorubicin-loaded DC Bead™," *Expert review of anticancer therapy,* vol. 8, no. 10, pp. 1643-1650, 2008.

[60] M. Sadick, S. Haas, M. Loehr, M. Elshwi, M. V. Singer, J. Brade, S. O. Schoenberg, and S. J. Diehl, "Application of DC beads in hepatocellular carcinoma: clinical and radiological results of a drug delivery device for transcatheter superselective arterial embolization," *Oncology Research and Treatment,* vol. 33, no. 1-2, pp. 31-37, 2010.

[61] M. Grosso, C. Vignali, P. Quaretti, A. Nicolini, F. Melchiorre, G. Gallarato, I. Bargellini, P. Petruzzi, C. M. Saluzzo, and S. Crespi, "Transarterial chemoembolization for hepatocellular carcinoma with drug-eluting microspheres: preliminary results from an Italian multicentre study," *Cardiovascular and interventional radiology,* vol. 31, no. 6, pp. 1141-1149, 2008.

[62] J. Lammer, K. Malagari, T. Vogl, F. Pilleul, A. Denys, A. Watkinson, M. Pitton, G. Sergent, T. Pfammatter, and S. Terraz, "Prospective randomized study of doxorubicin-eluting-bead embolization in the treatment of hepatocellular carcinoma: results of the PRECISION V study," *Cardiovascular and interventional radiology,* vol. 33, no. 1, pp. 41-52, 2010.

[63] M. Varela, M. I. Real, M. Burrel, A. Forner, M. Sala, M. Brunet, C. Ayuso, L. Castells, X. Montana, J. M. Llovet, and J. Bruix, "Chemoembolization of hepatocellular carcinoma with drug eluting beads: Efficacy and doxorubicin pharmacokinetics," *Journal of Hepatology,* vol. 46, no. 3, pp. 474-481, Mar 2007.

[64] S. Gao, Z. Yang, Z. Zheng, J. Yao, M. Deng, H. Xie, S. Zheng, and L. Zhou, "Doxorubicin-eluting bead versus conventional TACE for unresectable hepatocellular carcinoma: a meta-analysis," ed, 2013.

[65] S. Han, X. Zhang, L. Zou, C. Lu, J. Zhang, J. Li, and M. Li, "Does drug-eluting bead transcatheter arterial chemoembolization improve the management of patients with hepatocellular carcinoma? A meta-analysis," *PloS one,* vol. 9, no. 8, p. e102686, 2014.

[66] R. Golfieri, E. Giampalma, M. Renzulli, R. Cioni, I. Bargellini, C. Bartolozzi, A. Breatta, G. Gandini, R. Nani, and D. Gasparini, "Randomised controlled trial of doxorubicin-eluting beads vs conventional chemoembolisation for hepatocellular carcinoma," *British journal of cancer,* vol. 111, no. 2, p. 255, 2014.

[67] R. C. Martin, 2nd, C. R. Scoggins, D. Tomalty, M. Schreeder, T. Metzger, C. Tatum, and V. Sharma, "Irinotecan drug-eluting beads in the treatment of chemo-naive unresectable colorectal liver metastasis with concomitant systemic fluorouracil and oxaliplatin: results of pharmacokinetics and phase I trial," *J Gastrointest Surg,* Clinical Trial, Phase I Multicenter Study vol. 16, no. 8, pp. 1531-8, Aug 2012.

[68] R. C. Martin, J. Howard, D. Tomalty, K. Robbins, R. Padr, P. M. Bosnjakovic, and C. Tatum, "Toxicity of irinotecan-eluting beads in the treatment of hepatic malignancies: results of a multi-institutional registry," *Cardiovasc Intervent Radiol,* Clinical Trial Multicenter Study Research Support, Non-U.S. Gov't vol. 33, no. 5, pp. 960-6, Oct 2010.

[69] R. C. Martin, 2nd, L. Rustein, D. Perez Enguix, J. Palmero, V. Carvalheiro, J. Urbano, A. Valdata, I. Kralj, P. Bosnjakovic, and C. Tatum, "Hepatic arterial infusion of doxorubicin-loaded microsphere for treatment of hepatocellular cancer: a multi-institutional registry," *J Am Coll Surg,* Multicenter Study vol. 213, no. 4, pp. 493-500, Oct 2011.

[70] G. Fiorentini, C. Aliberti, G. Turrisi, A. Del Conte, S. Rossi, G. Benea, and P. Giovanis, "Intraarterial hepatic chemoembolization of liver metastases from colorectal cancer adopting irinotecan-eluting beads: results of a phase II clinical study," *In Vivo,* Clinical Trial, Phase II vol. 21, no. 6, pp. 1085-91, Nov-Dec 2007.

[71] K. Eichler, S. Zangos, M. G. Mack, R. Hammerstingl, T. Gruber-Rouh, C. Gallus, and T. J. Vogl, "First human study in treatment of unresectable liver metastases from colorectal cancer with irinotecan-loaded beads (DEBIRI)," *Int J Oncol,* vol. 41, no. 4, pp. 1213-20, Oct 2012.

[72] G. Fiorentini, C. Aliberti, M. Tilli, L. Mulazzani, F. Graziano, P. Giordani, A. Mambrini, F. Montagnani, P. Alessandroni, V. Catalano, and P. Coschiera, "Intra-arterial infusion of

irinotecan-loaded drug-eluting beads (DEBIRI) versus intravenous therapy (FOLFIRI) for hepatic metastases from colorectal cancer: final results of a phase III study," *Anticancer Res,* vol. 32, no. 4, pp. 1387-95, Apr 2012.

[73] R. C. Martin, 2nd, C. R. Scoggins, M. Schreeder, W. S. Rilling, C. J. Laing, C. M. Tatum, L. R. Kelly, R. D. Garcia-Monaco, V. R. Sharma, T. S. Crocenzi, and S. M. Strasberg, "Randomized controlled trial of irinotecan drug-eluting beads with simultaneous FOLFOX and bevacizumab for patients with unresectable colorectal liver-limited metastasis," *Cancer,* vol. 121, no. 20, pp. 3649-58, Oct 15 2015.

[74] G. Scevola, G. Loreni, M. Rastelli, S. Sposato, S. Ramponi, and V. Miele, "Third-line treatment of colorectal liver metastases using DEBIRI chemoembolization," *Med Oncol,* vol. 34, no. 3, p. 37, Mar 2017.

[75] R. Duran, K. Sharma, M. R. Dreher, K. Ashrafi, S. Mirpour, M. Lin, R. E. Schernthaner, T. R. Schlachter, V. Tacher, A. L. Lewis, S. Willis, M. den Hartog, A. Radaelli, A. H. Negussie, B. J. Wood, and J. F. Geschwind, "A Novel Inherently Radiopaque Bead for Transarterial Embolization to Treat Liver Cancer - A Pre-clinical Study," *Theranostics,* vol. 6, no. 1, pp. 28-39, 2016.

[76] E. B. Levy, V. P. Krishnasamy, A. L. Lewis, S. Willis, C. Macfarlane, V. Anderson, I. M. van der Bom, A. Radaelli, M. R. Dreher, K. V. Sharma, A. Negussie, A. S. Mikhail, J. F. Geschwind, and B. J. Wood, "First Human Experience with Directly Image-able Iodinated Embolization Microbeads," *Cardiovasc Intervent Radiol,* vol. 39, no. 8, pp. 1177-86, Aug 2016.

[77] P. Popovic, B. Stabuc, R. Jansa, and M. Garbajs, "Survival of patients with intermediate stage hepatocellular carcinoma treated with superselective transarterial chemoembolization using doxorubicin-loaded DC Bead under cone-beam computed tomography control," *Radiol Oncol,* vol. 50, no. 4, pp. 418-426, Dec 1 2016.

[78] J. M. Idee and B. Guiu, "Use of Lipiodol as a drug-delivery system for transcatheter arterial chemoembolization of hepatocellular carcinoma: A review," *Critical Reviews in Oncology Hematology,* vol. 88, no. 3, pp. 530-549, Dec 2013.

[79] C. Heunis, J. Sikorski, and S. Misra, "Flexible Instruments for Endovascular Interventions," *IEEE ROBOTICS & AUTOMATION MAGAZINE,* vol. 25, no. 3, pp. 71-82, 2018.

[80] T. Roberts, W. Hassenzahl, S. Hetts, and R. Arenson, "Remote control of catheter tip deflection: an opportunity for interventional MRI," *Magnetic Resonance in Medicine: An Official Journal of the International Society for Magnetic Resonance in Medicine,* vol. 48, no. 6, pp. 1091-1095, 2002.

[81] L. Muller, M. Saeed, M. W. Wilson, and S. W. Hetts, "Remote control catheter navigation: options for guidance under MRI," *Journal of Cardiovascular Magnetic Resonance,* vol. 14, no. 1, p. 33, 2012.

[82] F. P. Gosselin, V. Lalande, and S. Martel, "Characterization of the deflections of a catheter steered using a magnetic resonance imaging system," *Medical physics,* vol. 38, no. 9, pp. 4994-5002, 2011.

[83] K. Zhang, A. J. Krafft, R. Umathum, F. Maier, W. Semmler, and M. Bock, "Real-time MR navigation and localization of an intravascular catheter with ferromagnetic components," *Magnetic Resonance Materials in Physics, Biology and Medicine,* vol. 23, no. 3, pp. 153-163, 2010.

[84] S. Hetts, M. Saeed, A. Martin, L. Evans, A. Bernhardt, V. Malba, F. Settecase, L. Do, E. Yee, and A. Losey, "Endovascular catheter for magnetic navigation under MR imaging guidance: evaluation of safety in vivo at 1.5 T," *American journal of neuroradiology,* 2013.

[85] T. Liu, R. Jackson, D. Franson, N. L. Poirot, R. K. Criss, N. Seiberlich, M. A. Griswold, and M. C. Çavuşoğlu, "Iterative Jacobian-Based Inverse Kinematics and Open-Loop Control of an MRI-Guided Magnetically Actuated Steerable Catheter System," *IEEE/ASME Transactions on Mechatronics,* vol. 22, no. 4, pp. 1765-1776, 2017.

[86] L. B. Kratchman, T. L. Bruns, J. J. Abbott, and R. J. Webster, "Guiding elastic rods with a robot-manipulated magnet for medical applications," *IEEE Transactions on Robotics,* vol. 33, no. 1, pp. 227-233, 2017.

[87] V. N. Le, N. H. Nguyen, K. Alameh, R. Weerasooriya, and P. Pratten, "Accurate modeling and positioning of a magnetically controlled catheter tip," *Medical physics,* vol. 43, no. 2, pp. 650-663, 2016.

[88] K. J. Boskma, S. Scheggi, and S. Misra, "Closed-loop control of a magnetically-actuated catheter using two-dimensional ultrasound images," in *Biomedical Robotics and Biomechatronics (BioRob), 2016 6th IEEE International Conference on*, 2016, pp. 61-66: IEEE.

[89] M. Latulippe and S. Martel, "Dipole field navigation: Theory and proof of concept," *IEEE Transactions on Robotics,* vol. 31, no. 6, pp. 1353-1363, 2015.

[90] M. Latulippe, O. Felfoul, P. E. Dupont, and S. Martel, "Enabling automated magnetic resonance imaging-based targeting assessment during dipole field navigation," *Applied Physics Letters,* vol. 108, no. 6, p. 062403, 2016.

[91] S. Martel, J. B. Mathieu, O. Felfoul, A. Chanu, E. Aboussouan, S. Tamaz, P. Pouponneau, L. Yahia, G. Beaudoin, G. Soulez, and M. Mankiewicz, "A computer-assisted protocol for endovascular target interventions using a clinical MRI system for controlling untethered microdevices and future nanorobots," *Computer Aided Surgery,* vol. 13, no. 6, pp. 340-352, Nov 2008.

[92] J. B. Mathieu and S. Martel, "Magnetic microparticle steering within the constraints of an MRI system: proof of concept of a novel targeting approach," *Biomedical Microdevices,* vol. 9, no. 6, pp. 801-808, Dec 2007.

[93] J. B. Mathieu, G. Beaudoin, and S. Martel, "Method of propulsion of a ferromagnetic core in the cardiovascular system through magnetic gradients generated by an MRI system," *Ieee Transactions on Biomedical Engineering,* vol. 53, no. 2, pp. 292-299, Feb 2006.

[94] J. F. Schenck, "The role of magnetic susceptibility in magnetic resonance imaging: MRI magnetic compatibility of the first and second kinds," *Medical Physics,* vol. 23, no. 6, pp. 815-850, Jun 1996.

[95] M. Suwa and H. Watarai, "Magnetoanalysis of micro/nanoparticles: A review," *Analytica Chimica Acta,* vol. 690, no. 2, pp. 137-147, Apr 1 2011.

[96] S. Vaidya, K. R. Tozer, and J. Chen, "An overview of embolic agents," *Semin Intervent Radiol,* vol. 25, no. 3, pp. 204-15, Sep 2008.

[97] M. A. Washington, D. J. Swiner, K. R. Bell, M. V. Fedorchak, S. R. Little, and T. Y. Meyer, "The impact of monomer sequence and stereochemistry on the swelling and erosion of biodegradable poly (lactic-co-glycolic acid) matrices," *Biomaterials,* vol. 117, pp. 66-76, 2017.

[98] J. M. Anderson and M. S. Shive, "Biodegradation and biocompatibility of PLA and PLGA microspheres," *Advanced drug delivery reviews,* vol. 28, no. 1, pp. 5-24, 1997.

[99] S. Han, X. Zhang, and M. Li, "Progress in research and application of PLGA embolic microspheres," *Front Biosci (Landmark Ed),* vol. 21, pp. 931-40, Jun 1 2016.

[100] D. Dufrane, R.-M. Goebbels, A. Saliez, Y. Guiot, and P. Gianello, "Six-month survival of microencapsulated pig islets and alginate biocompatibility in primates: proof of concept," *Transplantation,* vol. 81, no. 9, pp. 1345-1353, 2006.

[101] K. Liu, H.-J. Ding, J. Liu, Y. Chen, and X.-Z. Zhao, "Shape-controlled production of biodegradable calcium alginate gel microparticles using a novel microfluidic device," *Langmuir,* vol. 22, no. 22, pp. 9453-9457, 2006.

[102] B. Thu, P. Bruheim, T. Espevik, O. Smidsrød, P. Soon-Shiong, and G. Skjåk-Bræk, "Alginate polycation microcapsules: I. Interaction between alginate and polycation," *Biomaterials,* vol. 17, no. 10, pp. 1031-1040, 1996.

[103] C. Zhang and C. Shi, "Superparamagnetic Iron Oxide Nanaoparticles for in Vivo Stem Cell Tracking," *Experimental Hematology,* vol. 37, no. 9, pp. S102-S102, Sep 2009.

[104] J. S. Weinstein, C. G. Varallyay, E. Dosa, S. Gahramanov, B. Hamilton, W. D. Rooney, L. L. Muldoon, and E. A. Neuwelt, "Superparamagnetic iron oxide nanoparticles: diagnostic magnetic resonance imaging and potential therapeutic applications in neurooncology and central nervous system inflammatory pathologies, a review," *Journal of Cerebral Blood Flow and Metabolism,* vol. 30, no. 1, pp. 15-35, Jan 2010.

[105] P. Pouponneau, J. C. Leroux, and S. Martel, "Magnetic nanoparticles encapsulated into biodegradable microparticles steered with an upgraded magnetic resonance imaging system for tumor chemoembolization," *Biomaterials,* Research Support, Non-U.S. Gov't vol. 30, no. 31, pp. 6327-32, Oct 2009.

[106] Z. Nosrati, N. Li, F. Michaud, S. Ranamukhaarachchi, S. Karagiozov, G. Soulez, S. Martel, K. Saatchi, and U. O. Hafeli, "Development of a Coflowing Device for the Size-Controlled Preparation of Magnetic-Polymeric Microspheres as Embolization Agents in Magnetic Resonance Navigation Technology," *Acs Biomaterials Science & Engineering,* vol. 4, no. 3, pp. 1092-1102, Mar 2018.

[107] K. Malagari, M. Pomoni, H. Moschouris, A. Kelekis, A. Charokopakis, E. Bouma, T. Spyridopoulos, A. Chatziioannou, V. Sotirchos, T. Karampelas, C. Tamvakopoulos, D. Filippiadis,

E. Karagiannis, A. Marinis, J. Koskinas, and D. A. Kelekis, "Chemoembolization of Hepatocellular Carcinoma with Hepasphere 30-60 mu m. Safety and Efficacy Study," *Cardiovascular and Interventional Radiology,* vol. 37, no. 1, pp. 165-175, Feb 2014.

[108] P. Bastian, R. Bartkowski, H. Kohler, and T. Kissel, "Chemo-embolization of experimental liver metastases. Part I: distribution of biodegradable microspheres of different sizes in an animal model for the locoregional therapy," *European Journal of Pharmaceutics and Biopharmaceutics,* vol. 46, no. 3, pp. 243-254, Nov 1998.

[109] K. T. Brown, "Fatal pulmonary complications after arterial embolization with 40-120-micro m tris-acryl gelatin microspheres," *J Vasc Interv Radiol,* vol. 15, no. 2 Pt 1, pp. 197-200, Feb 2004.

[110] K. H. Lee, E. Liapi, J. A. Vossen, M. Buijs, V. P. Ventura, C. Georgiades, K. Hong, I. Kamel, M. S. Torbenson, and J. F. Geschwind, "Distribution of iron oxide-containing Embosphere particles after transcatheter arterial embolization in an animal model of liver cancer: evaluation with MR imaging and implication for therapy," *J Vasc Interv Radiol,* vol. 19, no. 10, pp. 1490-6, Oct 2008.

[111] B. C. Odisio, A. Ashton, Y. Yan, W. Wei, A. Kaseb, M. J. Wallace, J. N. Vauthey, S. Gupta, and A. L. Tam, "Transarterial hepatic chemoembolization with 70-150 microm drug-eluting beads: assessment of clinical safety and liver toxicity profile," *J Vasc Interv Radiol,* vol. 26, no. 7, pp. 965-71, Jul 2015.

[112] A. R. Deipolyi, R. Oklu, S. Al-Ansari, A. X. Zhu, L. Goyal, and S. Ganguli, "Safety and efficacy of 70-150 mum and 100-300 mum drug-eluting bead transarterial chemoembolization for hepatocellular carcinoma," *J Vasc Interv Radiol,* vol. 26, no. 4, pp. 516-22, Apr 2015.

[113] P. Vartholomeos, C. Mavroidis, and N. Hata, "Magnetic Targeting of Aggregated Nanoparticles for Advanced Lung Therapies: A Robotics Approach," *2010 3rd Ieee Ras and Embs International Conference on Biomedical Robotics and Biomechatronics,* pp. 861-868, 2010.

[114] J. Riegler, B. Allain, R. J. Cook, M. F. Lythgoe, and Q. A. Pankhurst, "Magnetically assisted delivery of cells using a magnetic resonance imaging system," *Journal of Physics D-Applied Physics,* vol. 44, no. 5, Feb 9 2011.

[115] J. B. Mathieu and S. Martel, "Aggregation of magnetic microparticles in the context of targeted therapies actuated by a magnetic resonance imaging system," *Journal of Applied Physics,* vol. 106, no. 4, p. 044904, Aug 15 2009.

[116] A. Bigot, G. Soulez, and S. Martel, "A prototype of injector to control and to detect the release of magnetic beads within the constraints of multibifurcation magnetic resonance navigation procedures," *Magn Reson Med,* vol. 77, no. 1, pp. 444-452, Jan 2017.

[117] A. Bigot, C. Tremblay, G. Soulez, and S. Martel, "Magnetic Resonance Navigation of a Bead Inside a Three-Bifurcation PMMA Phantom Using an Imaging Gradient Coil Insert," *Ieee Transactions on Robotics,* vol. 30, no. 3, pp. 719-727, Jun 2014.

[118] J. A. McNab, B. L. Edlow, T. Witzel, S. Y. Huang, H. Bhat, K. Heberlein, T. Feiweier, K. Liu, B. Keil, and J. Cohen-Adad, "The Human Connectome Project and beyond: initial applications of 300 mT/m gradients," *Neuroimage,* vol. 80, pp. 234-245, 2013.

[119] L. A. d. Silveira, F. B. C. Silveira, and V. P. S. Fazan, "Arterial diameter of the celiac trunk and its branches: anatomical study," *Acta cirurgica brasileira,* vol. 24, no. 1, pp. 43-47, 2009.

[120] B. J. Nelson, I. K. Kaliakatsos, and J. J. Abbott, "Microrobots for minimally invasive medicine," *Annual review of biomedical engineering,* vol. 12, pp. 55-85, 2010.

[121] G. Vidal and S. Martel, "Measuring the magnetophoretic characteristics of magnetic agents for targeted diagnostic or therapeutic interventions in the vascular network," *Journal of Micro-Bio Robotics,* vol. 8, no. 2, pp. 65-71, 2013.

[122] K. R. T. S. Vaidya, J. Chen "An overview of embolic agents," *Semin Intervent Radiol,* vol. 25, no. 3, pp. 204-15, 2008.

[123] J. E. lPPERA, "Embolization in Trauma: Principles and Techniques," *Semin Intervent Radiol.,* vol. 27, no. 1, pp. 14–28, 2010.

[124] V. G. P. S. R.Veeram Reddy, and S. K. Gualano, "Amplatzer vascular plug IV for occlusion of pulmonary arteriovenous malformations in a patient with cryptogenic stroke," *Ann Pediatr Cardiol.,* vol. 7, no. 2, pp. 145-147, 2014.

[125] L. Zhang, Q. Gong, H. Xiao, C. Tu, and J. Liu, "Control of blood loss during sacral surgery by aortic balloon occlusion," *Anesthesia & Analgesia,* vol. 105, no. 3, pp. 700-703, 2007.

[126] I. Timor-Tritsch, G. Cali, A. Monteagudo, N. Khatib, R. Berg, F. Forlani, and E. Avizova, "Foley balloon catheter to prevent or manage bleeding during treatment for cervical and Cesarean scar pregnancy," *Ultrasound in Obstetrics & Gynecology,* vol. 46, no. 1, pp. 118-123, 2015.

[127] M. Lubarsky, C. E. Ray Jr, and B. Funaki, "Embolization agents—which one should be used when? Part 1: large-vessel embolization," in *Seminars in interventional radiology*, 2009, vol. 26, no. 4, p. 352: Thieme Medical Publishers.

[128] D. E. Kiousis, A. R. Wulff, and G. A. Holzapfel, "Experimental studies and numerical analysis of the inflation and interaction of vascular balloon catheter-stent systems," *Annals of Biomedical Engineering,* vol. 37, no. 2, pp. 315-330, 2009.

[129] F. Michaud, N. Li, R. Plantefève, Z. Nosrati, C. Tremblay, K. Saatchi, G. Moran, A. Bigot, U. O. Häfeli, S. Kadoury, A. Tang, P. Perreault, S. Martel, and G. Soulez, "Selective Embolization with Magnetized Microbeads using Magnetic Resonance Navigation in a Controlled-flow Liver Model," *Medical Physics,* vol. 0, no. ja.

[130] G. B. Chavhan, P. S. Babyn, B. Thomas, M. M. Shroff, and E. M. Haacke, "Principles, techniques, and applications of T2*-based MR imaging and its special applications," *Radiographics,* vol. 29, no. 5, pp. 1433-1449, 2009.

[131] E. L. Hahn, "Spin echoes," *Physical review,* vol. 80, no. 4, p. 580, 1950.

[132] H. Y. Carr and E. M. Purcell, "Effects of diffusion on free precession in nuclear magnetic resonance experiments," *Physical review,* vol. 94, no. 3, p. 630, 1954.

[133] B. Jung and M. Weigel, "Spin echo magnetic resonance imaging," *Journal of magnetic resonance imaging: JMRI,* vol. 37, no. 4, pp. 805-817, 2013.

[134] T. Wortmann, C. Dahmen, and a. S. Fatikow, "Study of MRI Susceptibility Artifacts for Nanomedical Applications," *Journal of Nanotechnology in Engineering and Medicine* vol. 1, no. 4, p. 041002, 2010.

[135] F. De Guio, H. Benoit-Cattin, and A. Davenel, "Quantitative study of signal decay due to magnetic susceptibility interfaces: Mri simulations and experiments," in *Engineering in Medicine and Biology Society, 2007. EMBS 2007. 29th Annual International Conference of the IEEE*, 2007, pp. 1607-1610: IEEE.

[136] T. Allkemper, C. Bremer, L. Matuszewski, W. Ebert, and P. Reimer, "Contrast-enhanced blood-pool MR angiography with optimized iron oxides: effect of size and dose on vascular contrast enhancement in rabbits," *Radiology,* vol. 223, no. 2, pp. 432-438, 2002.

[137] M. Poustchi-Amin, S. A. Mirowitz, J. J. Brown, R. C. McKinstry, and T. Li, "Principles and applications of echo-planar imaging: a review for the general radiologist," *Radiographics,* vol. 21, no. 3, pp. 767-779, 2001.

[138] D. Holland, J. M. Kuperman, and A. M. Dale, "Efficient correction of inhomogeneous static magnetic field-induced distortion in Echo Planar Imaging," *Neuroimage,* vol. 50, no. 1, pp. 175-183, 2010.

[139] K. Scheffler and J. Hennig, "Is TrueFISP a gradient-echo or a spin-echo sequence?," *Magnetic Resonance in Medicine: An Official Journal of the International Society for Magnetic Resonance in Medicine,* vol. 49, no. 2, pp. 395-397, 2003.

[140] R. M. Lebel, R. S. Menon, and C. V. Bowen, "Relaxometry model of strong dipolar perturbers for balanced-SSFP: Application to quantification of SPIO loaded cells," *Magnetic Resonance in Medicine: An Official Journal of the International Society for Magnetic Resonance in Medicine,* vol. 55, no. 3, pp. 583-591, 2006.

[141] A.-R. Mohammadi-Nejad, G.-A. Hossein-Zadeh, and H. Soltanian-Zadeh, "Quantitative evaluation of optimal imaging parameters for single-cell detection in MRI using simulation," *Magnetic resonance imaging,* vol. 28, no. 3, pp. 408-417, 2010.

[142] J. L. Duerk, J. S. Lewin, M. Wendt, and C. Petersilge, "Remember true FISP? A high SNR, near 1-second imaging method for T2-like contrast in interventional MRI at. 2 T," *Journal of Magnetic Resonance Imaging,* vol. 8, no. 1, pp. 203-208, 1998.

[143] N. J. Pelc, R. J. Herfkens, A. Shimakawa, and D. R. Enzmann, "Phase contrast cine magnetic resonance imaging," *Magnetic resonance quarterly,* vol. 7, no. 4, pp. 229-254, 1991.

[144] J. Lotz, C. Meier, A. Leppert, and M. Galanski, "Cardiovascular flow measurement with phase-contrast MR imaging: basic facts and implementation," *Radiographics,* vol. 22, no. 3, pp. 651-671, 2002.

[145] P. Moran, R. Moran, and N. Karstaedt, "Verification and evaluation of internal flow and motion. True magnetic resonance imaging by the phase gradient modulation method," *Radiology,* vol. 154, no. 2, pp. 433-441, 1985.

[146] C. E. Spritzer, N. J. Pelc, J. N. Lee, A. J. Evans, H. D. Sostman, and S. J. Riederer, "Rapid MR imaging of blood flow with a phase-sensitive, limited-flip-angle, gradient recalled pulse sequence: preliminary experience," *Radiology,* vol. 176, no. 1, pp. 255-262, 1990.

[147] M. O'donnell, "NMR blood flow imaging using multiecho, phase contrast sequences," *Medical physics,* vol. 12, no. 1, pp. 59-64, 1985.

[148] G. Nayler, D. Firmin, and D. Longmore, "Blood flow imaging by cine magnetic resonance," *J Comput Assist Tomogr,* vol. 10, no. 5, pp. 715-722, 1986.

[149] W.-Y. I. Tseng, M.-Y. M. Su, and Y.-H. E. Tseng, "Introduction to cardiovascular magnetic resonance: technical principles and clinical applications," *Acta Cardiologica Sinica,* vol. 32, no. 2, p. 129, 2016.

[150] G. Cabibbo, F. Latteri, M. Antonucci, and A. Craxì, "Multimodal approaches to the treatment of hepatocellular carcinoma," *Nature Reviews Gastroenterology & Hepatology,* vol. 6, no. 3, p. 159, 2009.

[151] J. B. Mathieu and S. Martel, "Steering of Aggregating Magnetic Microparticles Using Propulsion Gradients Coils in an MRI Scanner," *Magnetic Resonance in Medicine,* vol. 63, no. 5, pp. 1336-1345, May 2010.

[152] S. Martel, "Microrobotics in the vascular network: present status and next challenges," *Journal of Micro-Bio Robotics,* vol. 8, no. 1, pp. 41-52, 2013.

[153] D. Kessel and C. Ray, *Transcatheter embolization and therapy*. Springer Science & Business Media, 2010.

[154] A. J. Acero, C. Ferrera, J. M. Montanero, and A. M. Ganan-Calvo, "Focusing liquid microjets with nozzles," *Journal of Micromechanics and Microengineering,* vol. 22, no. 6, Jun 2012.

[155] S. Kobayashi, N. Ohwada, T. Yambe, S. Nanka, S. Nitta, T. Fukuju, T. Hongou, and H. Hashimoto, "Effects of oscillation on the arteries measured by arterial impedance during left ventricular assistance," *Journal of Artificial Organs,* vol. 2, no. 1, pp. 8-12, 1999.

[156] B. Bhushan, *Nanotribology and Nanomechanics I: Measurement Techniques and Nanomechanics*. Springer Science & Business Media, 2011.

[157] S. Kobayashi, S. Nitta, T. Yambe, T. Sonobe, and H. Hashimoto, "Arterial resonance inferred from analysis of arterial impedance," in *Heart Replacement*: Springer, 1998, pp. 484-486.

[158] S. Mittal and H. B. El-Serag, "Epidemiology of Hepatocellular Carcinoma Consider the Population," *Journal of Clinical Gastroenterology,* vol. 47, pp. S2-S6, Jul 2013.

[159] J. M. Llovet, M. I. Real, X. Montaña, R. Planas, S. Coll, J. Aponte, C. Ayuso, M. Sala, J. Muchart, and R. Solà, "Arterial embolisation or chemoembolisation versus symptomatic treatment in patients with unresectable hepatocellular carcinoma: a randomised controlled trial," *The Lancet,* vol. 359, no. 9319, pp. 1734-1739, 2002.

[160] H. Y. Kim, J. D. Kim, S. H. Bae, J. Y. Park, K. H. Han, H. Y. Woo, J. Y. Choi, S. K. Yoon, B. K. Jang, and J. S. Hwang, "A comparative study of high-dose hepatic arterial infusion chemotherapy and transarterial chemoembolization using doxorubicin for intractable, advanced hepatocellular carcinoma," *The Korean journal of hepatology,* vol. 16, no. 4, p. 355, 2010.

[161] A. Amirfazli, "Nanomedicine: magnetic nanoparticles hit the target," *Nature nanotechnology,* vol. 2, no. 8, p. 467, 2007.

[162] S. Tognarelli, V. Castelli, G. Ciuti, C. Di Natali, E. Sinibaldi, P. Dario, and A. Menciassi, "Magnetic propulsion and ultrasound tracking of endovascular devices," *Journal of robotic surgery,* vol. 6, no. 1, pp. 5-12, 2012.

[163] E. M. Cherry, P. G. Maxim, and J. K. Eaton, "Particle size, magnetic field, and blood velocity effects on particle retention in magnetic drug targeting," *Medical physics,* vol. 37, no. 1, pp. 175-182, 2010.

[164] L. Mellal, K. Belharet, D. Folio, and A. Ferreira, "Optimal structure of particles-based superparamagnetic microrobots: application to MRI guided targeted drug therapy," *Journal of Nanoparticle Research,* vol. 17, no. 2, p. 64, 2015.

[165] C. Zhang and C. Shi, "Superparamagnetic Iron Oxide Nanaoparticles for in Vivo Stem Cell Tracking," in *Experimental Hematology*, 2009, vol. 37, no. 9, pp. S102-S102: ELSEVIER SCIENCE INC 360 PARK AVE SOUTH, NEW YORK, NY 10010-1710 USA.

[166] M. P. Kummer, J. J. Abbott, B. E. Kratochvil, R. Borer, A. Sengul, and B. J. Nelson, "OctoMag: An electromagnetic system for 5-DOF wireless micromanipulation," *IEEE Transactions on Robotics,* vol. 26, no. 6, pp. 1006-1017, 2010.

[167] B. Shapiro, K. Dormer, and I. B. Rutel, "A two-magnet system to push therapeutic nanoparticles," in *AIP conference proceedings*, 2010, vol. 1311, no. 1, p. 77: NIH Public Access.

[168] S. Tamaz, R. Gourdeau, A. Chanu, J. B. Mathieu, and S. Martel, "Real-time MRI-based control of a ferromagnetic core for endovascular navigation," *Ieee Transactions on Biomedical Engineering,* vol. 55, no. 7, pp. 1854-1863, Jul 2008.

[169] M. Latulippe and S. Martel, "Evaluation of the Potential of Dipole Field Navigation for the Targeted Delivery of Therapeutic Agents in a Human Vascular Network," *IEEE Transactions on Magnetics,* vol. 54, no. 2, pp. 1-12, 2018.

[170] S. Martel, "Magnetic Navigation Control of Microagents in the Vascular Network CHALLENGES AND STRATEGIES FOR ENDOVASCULAR MAGNETIC NAVIGATION CONTROL OF MICROSCALE DRUG DELIVERY CARRIERS," *Ieee Control Systems Magazine,* vol. 33, no. 6, pp. 119-134, Dec 2013.

[171] P. V. Lillaney, J. K. Yang, A. D. Losey, A. J. Martin, D. L. Cooke, B. R. H. Thorne, D. C. Barry, A. Chu, C. Stillson, L. Do, R. L. Arenson, M. Saeed, M. W. Wilson, and S. W. Hetts, "Endovascular MR-guided Renal Embolization by Using a Magnetically Assisted Remote-controlled Catheter System," *Radiology,* vol. 281, no. 1, pp. 219-228, Oct 2016.

[172] L. A. da Silveira, F. B. C. Silveira, and V. P. S. Fazan, "Arterial diameter of the celiac trunk and its branches. Anatomical study," *Acta Cirurgica Brasileira,* vol. 24, no. 1, pp. 43-47, Jan-Feb 2009.

[173] K.-H. Lee, E. Liapi, J. A. Vossen, M. Buijs, V. P. Ventura, C. Georgiades, K. Hong, I. Kamel, M. S. Torbenson, and J.-F. H. Geschwind, "Distribution of iron oxide–containing Embosphere particles after transcatheter arterial embolization in an animal model of liver cancer:

evaluation with MR imaging and implication for therapy," *Journal of Vascular and Interventional Radiology,* vol. 19, no. 10, pp. 1490-1496, 2008.

[174] M. Mascolo, Y. Pei, and T. Ring, "Room temperature co-precipitation synthesis of magnetite nanoparticles in a large pH window with different bases," *Materials,* vol. 6, no. 12, pp. 5549-5567, 2013.

[175] P. Pouponneau, G. Soulez, G. Beaudoin, J.-C. Leroux, and S. Martel, "MR imaging of therapeutic magnetic microcarriers guided by magnetic resonance navigation for targeted liver chemoembolization," *Cardiovascular and interventional radiology,* vol. 37, no. 3, pp. 784-790, 2014.

[176] T. Chemoembolization, "Quality improvement guidelines for transarterial chemoembolization and embolization of hepatic malignancy," *J Vasc Interv Radiol,* vol. 28, pp. 1210-1223, 2017.

[177] S. Zhang, C. Huang, Z. Li, Y. Yang, T. Bao, H. Chen, Y. Zou, and L. Song, "Comparison of pharmacokinetics and drug release in tissues after transarterial chemoembolization with doxorubicin using diverse lipiodol emulsions and CalliSpheres Beads in rabbit livers," *Drug delivery,* vol. 24, no. 1, pp. 1011-1017, 2017.

[178] V. Lalande, F. P. Gosselin, M. Vonthron, B. Conan, C. Tremblay, G. Beaudoin, G. Soulez, and S. Martel, "In vivo demonstration of magnetic guidewire steerability in a MRI system with additional gradient coils," *Medical Physics,* vol. 42, no. 2, pp. 969-976, Feb 2015.

[179] H. Dyvorne, A. Knight-Greenfield, G. Jajamovich, C. Besa, Y. Cui, A. Stalder, M. Markl, and B. Taouli, "Abdominal 4D flow MR imaging in a breath hold: combination of spiral sampling and dynamic compressed sensing for highly accelerated acquisition," *Radiology,* vol. 275, no. 1, pp. 245-254, 2014.

[180] B.-B. Chen, C.-Y. Hsu, C.-W. Yu, P.-C. Liang, C. Hsu, C.-H. Hsu, A.-L. Cheng, and T. T.-F. Shih, "Dynamic contrast-enhanced MR imaging of advanced hepatocellular carcinoma: comparison with the liver parenchyma and correlation with the survival of patients receiving systemic therapy," *Radiology,* vol. 281, no. 2, pp. 454-464, 2016.

[181] F. Michaud, N. Li, R. PlantefEve, Z. Nosrati, C. Tremblay, K. Saatchi, G. Moran, A. Bigot, U. Häfeli, S. Kadoury, A. Tang, P. Perreault, S. Martel, and G. Soulez, "Injection System and Navigation of Magnetic Microbeads Using MRI Gradients," to be published.

[182] S. F. Altekruse, K. A. McGlynn, and M. E. Reichman, "Hepatocellular carcinoma incidence, mortality, and survival trends in the United States from 1975 to 2005," *Journal of clinical oncology,* vol. 27, no. 9, p. 1485, 2009.

[183] J. Belghiti and R. Kianmanesh, "Surgical treatment of hepatocellular carcinoma," *Hpb,* vol. 7, no. 1, pp. 42-49, 2005.

[184] S. Herber, J. Schneider, B. Brecher, T. Höhler, M. Thelen, G. Otto, and M. Pitton, "TACE: therapy of the HCC before liver transplantation--experiences," *RoFo: Fortschritte auf dem Gebiete der Rontgenstrahlen und der Nuklearmedizin,* vol. 177, no. 5, pp. 681-690, 2005.

[185] R. C. Gaba, R. J. Lewandowski, R. Hickey, M. O. Baerlocher, E. I. Cohen, S. R. Dariushnia, d. O. B. Janne, S. A. Padia, R. Salem, and D. S. Wang, "Transcatheter therapy for hepatic malignancy: standardization of terminology and reporting criteria," *Journal of vascular and interventional radiology: JVIR,* vol. 27, no. 4, p. 457, 2016.

[186] R. J. Lewandowski, J.-F. Geschwind, E. Liapi, and R. Salem, "Transcatheter intraarterial therapies: rationale and overview," *Radiology,* vol. 259, no. 3, pp. 641-657, 2011.

[187] L. R. Roberts, C. B. Sirlin, F. Zaiem, J. Almasri, L. J. Prokop, J. K. Heimbach, M. H. Murad, and K. Mohammed, "Imaging for the diagnosis of hepatocellular carcinoma: A systematic review and meta-analysis," *Hepatology,* vol. 67, no. 1, pp. 401-421, 2018.

[188] O. Felfoul, A. T. Becker, G. Fagogenis, and P. E. Dupont, "Simultaneous steering and imaging of magnetic particles using MRI toward delivery of therapeutics," *Scientific Reports,* vol. 6, p. 33567, Sep 26 2016.

[189] T. De Baere and P. Mariani, "Surgical or percutaneous hepatic artery cannulation for chemotherapy," *Journal of visceral surgery,* vol. 151, pp. S17-S20, 2014.

[190] N. Li, C. Tremblay, and S. Martel, "Combining oscillating flow and clinical MRI gradients for targeted therapy," in *2017 International Conference on Manipulation, Automation and Robotics at Small Scales (MARSS)*, 2017, pp. 1-4: IEEE.

[191] N. Li, F. Michaud, Z. Nosrati, D. Loghin, C. Tremblay, R. Plantefeve, K. Saatchi, U. Hafeli, S. M. Martel, and G. Soulez, "MRI-compatible injection system for magnetic microparticle embolization," *IEEE Transactions on Biomedical Engineering,* 2018.

[192] F. Michaud, N. Li, R. Plantefève, Z. Nosrati, C. Tremblay, K. Saatchi, G. Moran, A. Bigot, U. O. Häfeli, and S. Kadoury, "Selective embolization with magnetized microbeads using magnetic resonance navigation in a controlled-flow liver model," *Medical physics,* vol. 46, no. 2, pp. 789-799, 2019.

[193] G. S. Chaubey, C. Barcena, N. Poudyal, C. Rong, J. Gao, S. Sun, and J. P. Liu, "Synthesis and stabilization of FeCo nanoparticles," *Journal of the American Chemical Society,* vol. 129, no. 23, pp. 7214-7215, 2007.

[194] D.-H. Kim, J. Chen, R. A. Omary, and A. C. Larson, "MRI visible drug eluting magnetic microspheres for transcatheter intra-arterial delivery to liver tumors," *Theranostics,* vol. 5, no. 5, p. 477, 2015.

[195] T. Yzet, R. Bouzerar, J. D. Allart, F. Demuynck, C. Legallais, B. Robert, H. Deramond, M. E. Meyer, and O. Balédent, "Hepatic vascular flow measurements by phase contrast MRI and doppler echography: a comparative and reproducibility study," *Journal of Magnetic Resonance Imaging: An Official Journal of the International Society for Magnetic Resonance in Medicine,* vol. 31, no. 3, pp. 579-588, 2010.

[196] M. E. Fawzy, L. Mimish, V. Sivanandam, J. Lingamanaicker, M. AlAmri, B. Khan, B. Dunn, and C. Duran, "Advantage of Inoue balloon catheter in mitral balloon valvotomy: Experience with 220 consecutive patients," *Catheterization and Cardiovascular Diagnosis,* vol. 38, no. 1, pp. 9-14, May 1996.

[197] M. Latulippe, O. Felfoul, P. E. Dupont, and S. Martel, "Enabling automated magnetic resonance imaging-based targeting assessment during dipole field navigation," *Applied Physics Letters,* vol. 108, no. 6, Feb 8 2016.

[198] Y. Feng, J. Goree, and B. Liu, "Accurate particle position measurement from images," *Review of scientific instruments,* vol. 78, no. 5, p. 053704, 2007.

[199] Y. Ivanov and A. Melzer, "Particle positioning techniques for dusty plasma experiments," *Review of scientific instruments,* vol. 78, no. 3, p. 033506, 2007.

APPENDIX A - DESIGN OF THE PARTICLES FOR MRN

As mentioned before, MDEBs were designed and fabricated in our laboratory. However, they were not available because these micro-particles were produced in limited quantities. Indeed, they were only produced to demonstrate that it was possible to generate magnetic loaded drug carriers to use in MRN. I searched for a reliable encapsulation method for MMC fabrication and was able to achieve our desired MMCs, as shown in figure A-1. Gas-liquid flow focusing approach, a type of coaxial air jet techniques, was used for the encapsulation of MMCs. This technique uses the pressure gradient generated by an outer gas stream to focus a steady liquid jet of the dispersed phase. Alginate solution (1.5%, 0.5 ml) (Sigma-Alrich, St. Louis, MO) was used as the base material for MMCs. The alginate solution was stirred with ferrofluid (0.5 ml) (fluidMAG-D, Chemicell GmbH, Germany) and its application was used for MRI diagnostic and covalent coupling of bioligands. The ferrofluid contains about 25 mg⁄mL superparamagnetic particles with a 200 nm hydrodynamic diameter. Magnetic moments of the fluid were measured using a vibrating sample magnetizer (EV9, microsence). The saturation magnetization was measured at 1.36 emu/g, and it was confirmed, through the hysteresis curve, that the fluid was almost completely saturated at 1.5 T. The mixed solution was injected into a calcium solution (1%) (Sigma-Alrich, St. Louis, MO) using the gas-liquid flow-focusing device, as shown in figure A-1(a). The diameter of the MMCs used in the experiment is 200 µm, as shown in figure 4-1 (ZEISS AxioImager microscope). Because the encapsulation techniques are not included in my research topic, we do not explore it further.

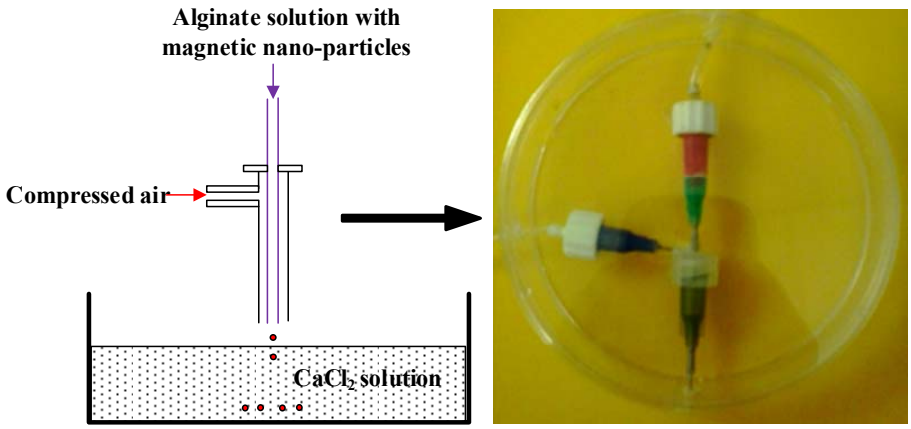

Figure A-1: Encapsulation system for fabricating MMCs.

APPENDIX B - BLOOD FLOW CONTROL WITH THE BALLON CATHETER AND ONE-BIFURCATION MRN

This chapter includes works from our experimental team. The purposes of this paper include two main ideas: 1) The possibility of precisely controlling the flow rate in hepatic arteries by using a balloon catheter; 2) The success rate of MRN in a single-bifurcation glass phantom. Parts of the results shown here have been published in the papers below.

François Michaud*, **Ning Li* (***Joint first author***)**, Rosalie Plantefève, Zeynab Nosrati, Charles Tremblay, Katayoun Saatchi, Gerald Moran, Alexandre Bigot, Urs O. Häfeli, Samuel Kadoury, An Tang, Pierre Perreault, Sylvain Martel, and Gilles Soulez, "Selective Embolization with Magnetized Microbeads using Magnetic Resonance Navigation in a Liver Controlled-flow Model ", *Medical Physics*. (Published)

The *in vivo* experiment was finished with the help of all authors listed in the article above. After the experiment, Mr. François Michaud calculated the velocity of controlled blood flow, which is listed in the last two paragraphs of the next section- *In vivo* validation of control over the flow rate in the hepatic arteries by using a balloon catheter. The candidate designed the setup for the second section-*In vitro* validation of MRN in a one bifurcation phantom-and did all the experiments listed in the table B-1. During the tests, Dr. Rosalie Plantefève was on duty of controlling the MRI steering force and recording the experiment results in the control room.

In vivo validation of control over the flow rate in the hepatic arteries by using a balloon catheter

This section mainly introduces the *in vivo* validation of controlling the flow rate in the hepatic arteries by using a balloon catheter.

The experimental steps are as follows:

1) Every pig underwent general anaesthesia;

2) The pigs were transferred into the angiography room equipped with a CT scanner. Here, the left gastric artery and the gastroduodenal artery were embolized with chitosan-sodium tetradecyl sulfate, followed by the insertion of a 5 French compliant occlusion balloon catheter (Fogarty,

Edwards Lifesciences, Irvine, CA). The catheter tip was in the proximal proper hepatic artery and was 3 to 4 cm from the right-left bifurcation.

3) The pigs were transferred into the MRI room in which liver angiography and velocity measurements with the phase-contrast cine sequence were done.

4) At the end of the experiments, the pigs were euthanized.

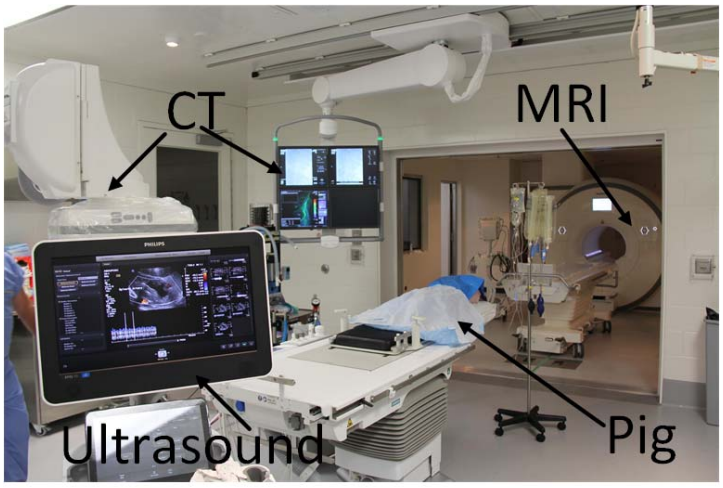

Figure B-1: Photo showing a pig being transferred from the angiography room into the MRI room.

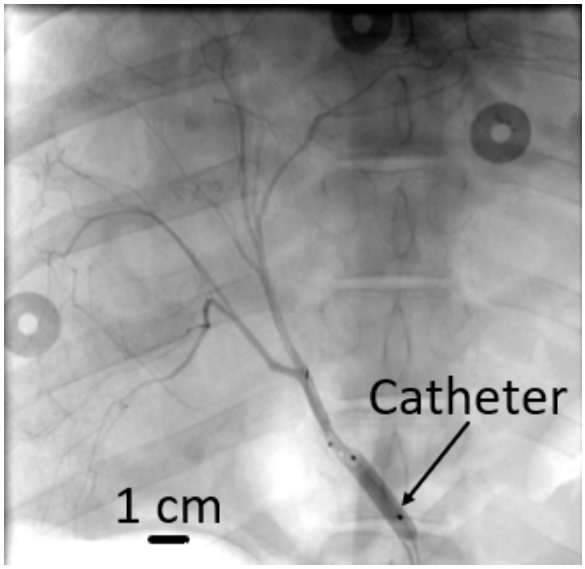

Figure B-2: CT image showing the catheter tip in the proximal hepatic artery.

When the balloon catheter was inflated, and the injection flow of a saline solution was set to 0.1, 0.2 or 0.5 ml/s, we measured the flow velocity through the 2D MRI phase-contrast cine sequence. The Venc was set at 20 cm/s and the other parameters were: TR = 24.4 ms, TE = 3.61 ms, flip angle = 20°, voxel size = 1.56 mm x 1.56 mm x 3.70 mm. The results of one pig are shown in figure B-4.

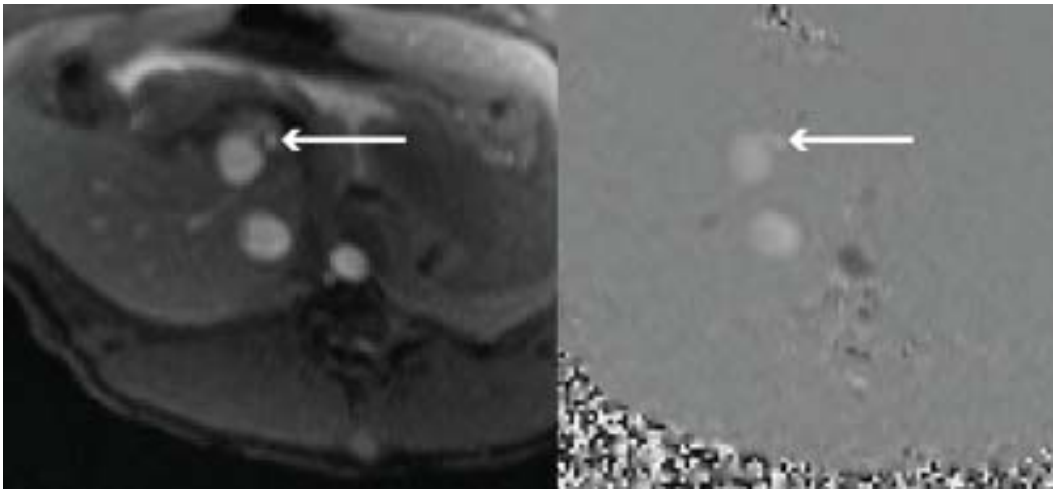

Figure B-3: Reproduced from [129]. MRI phase-contrast cine image of the proper hepatic artery in a pig. (a) Image showing the proper hepatic artery. (b) Phase image.

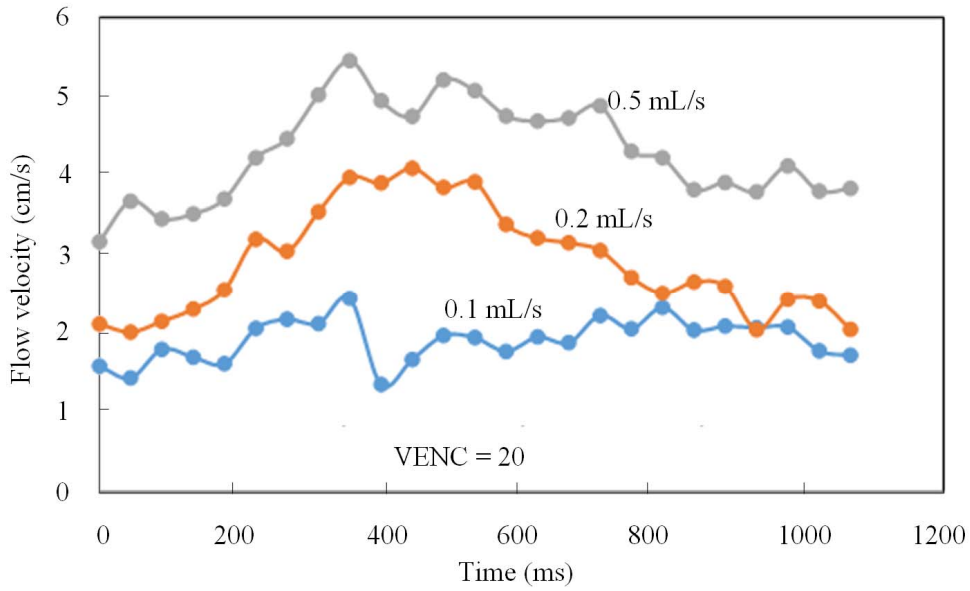

Figure B-4: Flow velocity when the injection rate is 0.1, 0.2, and 0.3 ml/s.

Considering the diameter of the main hepatic artery is about 4 mm (see figure B-2), the theoretical flow rate is 0.8, 1.6 and 4.0 cm/s, respectively. The measured results shown in figure B-4 have an average value of 1.93, 2.96 and 4.03 cm/s, respectively. Compared with the theoretical value, the error is within 10% when the flow is about 5 cm/s.

Then, with the same experimental conditions, 10 mL of a saline solution is injected distally to a pig at either 0.5 mL/s (2 pigs) or 1.0 mL/s (2 pigs) through a 5 Fr catheter. The mean flow velocity measured by the 2D MRI phase-contrast cine sequence is 20 ± 15 (n = 4, balloon non-inflation, injection rate = 0 mL/s), 12.0 ± 9.1 (n = 2, balloon inflation, injection rate = 1 mL/s) and 8.4 ± 5.0 cm/s (n = 1, balloon inflation, injection rate = 0.5 mL/s).

Four additional pigs underwent selective particle embolization of the right medial (n = 1) or left medial (n = 3) lobes using a microcatheter (FasTracker 325, Boston Scientific, Marlborough, MA) following by the injection of 50 μm radio-opaque particles (ABK, Halifax, Nova Scotia). Unfortunately, only the data from 3 out of the 4 embolized pigs have been obtained because the MRI scanner was dysfunctional during the experiment (embolization of the right medial (n = 1)). Ten mL of saline solution was injected distally to each pig at either 0.5 mL/s (3 pigs) or 1.0 mL/s (1 pig). It should be noted that: two pigs were injected at either 0.5 mL/s or 1 mL/s, and the third pig was injected with both of these two flow rates. The mean flow velocity was measured at 13.6 ± 2.0 (n = 4, balloon non-inflation), 14.1 (n = 1, balloon inflation, injection rate = 1 mL/s) and 5.4 ± 3.0 cm/s (n = 1, balloon inflation, injection rate = 0.5 mL/s).

In vitro validation of MRN in a one bifurcation phantom

After the *in vivo* validation of the control over the flow rate, the content in chapter 4 and the design of the particle injector in chapter 5, the *in vitro* validation of MRN in a single-bifurcation phantom was tested out, as shown in figure B-5.

The glass phantom has a 4 mm main branch while two 3 mm branch divisions have an angle of 60°. The flow injections included two parts: the catheter flow (0.2 mL/s constant flow) provided by Pump 2 and the bypass flow supply by Pump 3 (0.4 mL/s constant flow). Additionally, the vibration was set at a frequency of 1 Hz and an amplitude of 0.4 mL, which was used to prevent aggregates from sticking to the glass phantom's walls.

The magnetic gradient was always 20 mT/m and the pointing direction, either left or right, set to 90° relative to the main branch. The MDEBs (200 ± 20 µm) used in these experiments have a magnetization saturation value of 30 emu/g. Steering ratio differences were researched at different gradient orientations relative to B_0 (0°, 45°, 90°).

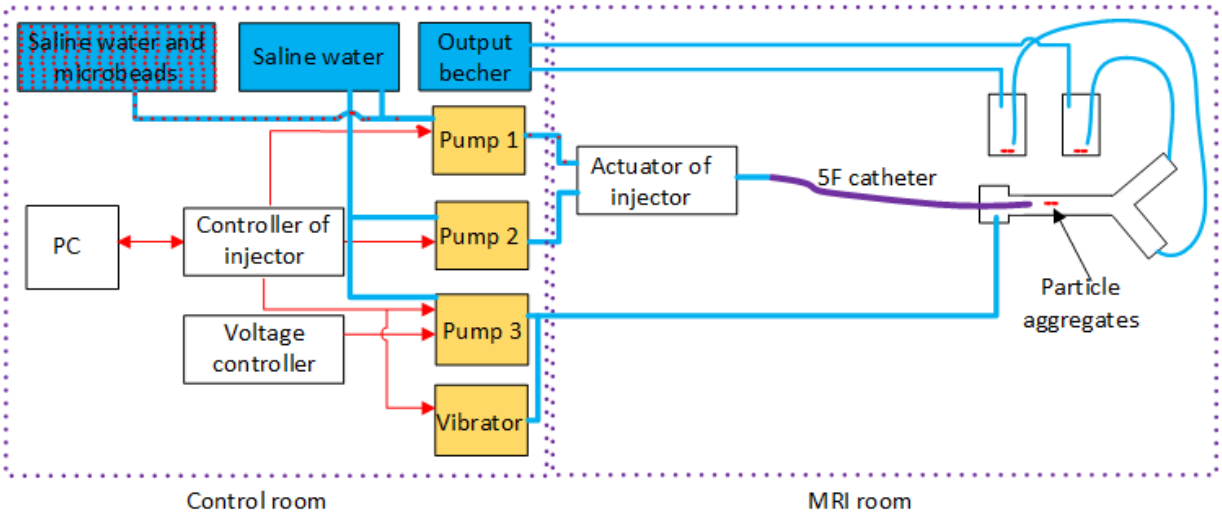

Figure B-5: Experimental setup of the *in vitro* validation of MRN in a single bifurcation phantom.

The results are presented in table B-1. For navigation without MRN, 45%, 75% and 25% of the aggregates entered the left branch for 0°, 45° and 90° phantom angulations, respectively. Using MRN, an 100% success rate was always obtained throughout the different angles.

Table B-1: Reproduced from [129]. Steering results in the phantom

Total steering number	**Gradient direction**	**Gradient magnitude (mT/m)**	**Right steering number (%)**	**Left steering number (%)**	**Steering efficiency**
0° angle with B_0					
20	No gradient	0	11 (55)	9 (45)	n/a
20	Right	20	20 (100)	0 (0)	100 %
20	Left	20	0 (0)	20 (100)	100 %
45° angle with B_0					
20	No gradient	0	5 (25)	15 (75)	n/a
20	Right	20	20 (100)	0 (0)	100 %
20	Left	20	0 (0)	20 (100)	100 %
90° angle with B_0					
20	No gradient	0	15 (75)	5 (25)	n/a
20	Right	20	20 (100)	0 (0)	100 %
20	Left	20	0 (0)	20 (100)	100%

APPENDIX C - INFLUENCE OF GRAVITY FOR MRN

Despite the magnetic force, MDEBs are also affected by gravity and buoyancy during MRN. In this section, the influence of gravity will be evaluated.

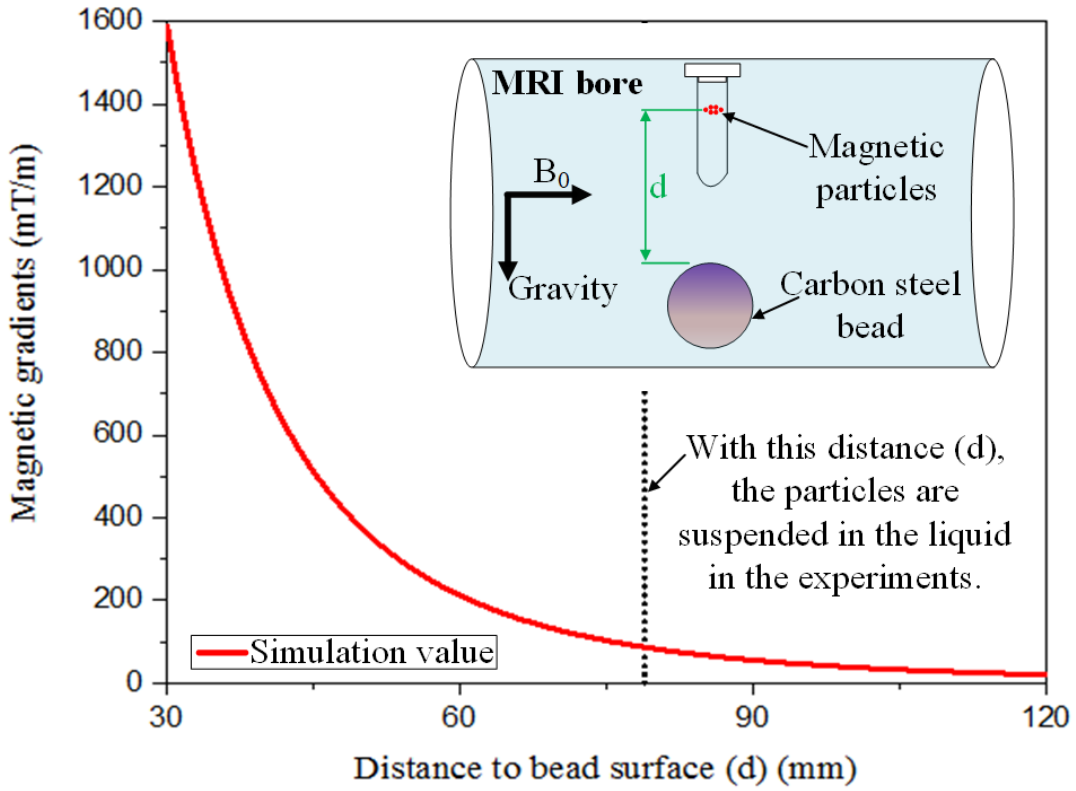

Figure C-1: Setup for calculating the appropriate gradient capable of lifting microparticle aggregates.

To obtain a strong magnetic field gradient that is high enough to lift particles in a saline solution, a carbon steel bead, with a diameter of 21.76 mm, was carefully put at the iso-center of a 3 T MRI bore, which was used to distort the uniform magnetic field of the MRI scanner. Above the bead, the distribution of magnetic gradients can be calculated by the formula below:

$$G = \frac{3\mu_0 m}{2\pi r^4} \qquad \text{(Eq. C-1)}$$

where μ_0 is the vacuum permeability ($4\pi \times 10^{-7}$ H/m), $\boldsymbol{r}$ the distance to the center of the core, and m the magnetic moment of the core.

$$m = \frac{4\pi R^3}{3} M \qquad \text{(Eq. C-2)}$$

where $\mu_0 = 4\pi \times 10^{-7}$ H/m is the vacuum permeability, m the magnetic moment of the bead, $\boldsymbol{R}$ the radius of the core and M the volume magnetization. Here, the saturation magnetization is 1.43×10^6 A/m which could be reached at B $\geq$ 1.3 T.

A vial containing a magnetic particle suspension was put above the bead. The position of the vial could be tuned manually. My experiments revealed that when d is 82 ± 3 mm (mean ± standard deviation and n =10), magnetic particles could be suspended in the saline solution. From calculations, I obtained that the magnetic gradient is about 76.5 mT/m.

When doing MRN, the magnetic force F_m applied on each magnetic particle is

$$F_m = V_p \ (M_p \bullet \nabla) \ B \qquad \text{(Eq. C-3)}$$

where V_p is the volume of magnetic particles, $M_p = 89.7 \times 10^3$ A/m the magnetization of particles, B the strength of the magnetic field, and ∇B the magnetic gradients. If the particles were to be navigated in a 3D phantom, F_m needs to be able to lift the microparticles in the liquid, which means:

$$F_m \geq V_p \ (\rho_p - \rho_S) \ g \qquad \text{(Eq. C-4)}$$

where $\rho_p = 2.95\ g/cm^3$ is the density of magnetic particles, $\rho_s = 1.0046\ g/cm^3$ the density of the saline solution and $g = 9.8\ N/kg$ the acceleration due to gravity. From the equation above, when the magnetic gradient is about 71.0 mT/m, F_m can lift the particles. Thus, this theoretical value is close to the experimental value (76.5 mT/m).

Considering the fact that the clinical 3 T MRI can only supply gradients up to 40 mT/m, the ratio r has to be bigger than 1 if we want to lift particles in liquids.

$$r = \frac{(M_p \bullet \nabla) \ B}{(\rho_p - \rho_S) \ g} \qquad \text{(Eq. C-5)}$$

According to the experimental phenomena and my calculations, Fe_3O_4 nanoparticles based microparticles can not be lifted in the -Y direction using a normal clinical MRI (≤ 40 mT/m) even if the homogeneous magnetic field is up to 3 T.

For 3D MRN, there are two possible options:

1) We can take advantage of using both the gravitational and magnetic forces.

2) We can use high magnetization materials, such as $Fe_{55}Co_{45}$ (about 270 emu/g) instead of Fe_3O_4 nanoparticles (about 75.3 emu/g). Although the cobalt has shown to be toxic for human bodies, the delayed PGLA degradation can make its release slow, thus decreasing systemic toxicity levels.

APPENDIX D - LIST OF MANUSCRIPTS ACCEPTED AND SUBMITTED FOR PUBLICATION, SELECTED CONFERENCE PROCEEDINGS

MANUSCRIPTS ACCEPTED, SUBMITTED, AND TO BE SUBMITTED

1. **Ning Li**, Francois Michaud, Zeynab Nosrati, et al. "MRI-compatible injection system for magnetic microparticle embolization", *IEEE Trans Biomed Eng.*, 2018. (Accepted and available online at: https://ieeexplore.ieee.org/abstract/document/8584114)
2. **Ning Li**, Yuting Jiang, Rosalie Plantefève, et al. "Magnetic resonance navigation for targeted embolization in a two-level bifurcation phantom", *Ann Biomed Eng.*, 2019. (Submission)
3. Francois Michaud, **Ning Li (co-first author)**, Rosalie Plantefève, et al. "Selective Embolization with Magnetized Microbeads using Magnetic Resonance Navigation in a Liver Controlled-flow Model", *Medical Physics*, 2018. (Accepted and available online at: https://aapm.onlinelibrary.wiley.com/doi/full/10.1002/mp.13298)
4. Zeynab Nosrati, **Ning Li**, François Michaud, et al. "Development of a Coflowing Device for the Size-Controlled Preparation of Magnetic-Polymeric Microspheres as Embolization Agents in Magnetic Resonance Navigation Technology", *ACS Biomaterials Science & Engineering* 4(3), 2018. (Accepted and available online at: https://pubs.acs.org/doi/abs/10.1021/acsbiomaterials.7b00839)
5. Francois Michaud, **Ning Li**, Rosalie Plantefève, et al. "In vitro feasibility study of magnetic resonance navigation in realistic physiological settings", *Journal of Vascular and Interventional Radiology*, 29(4), 2018. (Accepted and available online at: https://www.sciencedirect.com/science/article/pii/S105104431830349X)

CONFERENCES:

1. **Ning Li**, Charles Tremblay, Sylvain Martel. "Combining oscillating flow and clinical MRI gradients for targeted therapy", *International Conference on Manipulation, Automation and Robotics at Small Scales (MARSS)*, 17-21 Jul. 2017, Montreal. (Oral presentation + Article)

(Accepted and available online at: https://ieeexplore.ieee.org/abstract/document/8001937)

2. **Ning Li**, Yuting Jiang, Rosalie Plantefève, et al. "In vitro validation of magnetic resonance navigation in a two-bifurcation phantom for endovascular treatment of hepatocellular carcinoma", *INNOVE-ACTION*, 13-15, Nov. 2018, Montreal. (Oral presentation)
3. **Ning Li**, Yuting Jiang, Rosalie Plantefève, et al. "In vitro validation of magnetic resonance navigation in a two-bifurcation phantom for targeted embolization ", 7e Journée Universitaire (JU), 21, Feb. 2019, Montreal. (Poster)

BOOK CHAPTER:

1. Mahmood Mohammadi, Charles Tremblay, **Ning Li**, et al., Nanoparticles for nanorobotic agents dedicated to cancer therapy. edited by Prof. Nguyen, CRC Press, Published on February 27, 2018. (Published)